MnDOT Contract, No. 1003325, Work Order No. 56

NRRA Long-term Research Project

Performance Benefits of Fiber-reinforced Thin Concrete Pavement and Overlays

Task-2: First Year Annual Cell Performance Report (2017-2018)

Prepared by:
Manik Barman and Corey Crick, UMD
and
Tom Burnham, Minnesota Department of Transportation

UMD
UNIVERSITY OF MINNESOTA DULUTH
Driven to Discover

DEPARTMENT OF TRANSPORTATION

2018

DISCLAIMER

This report represents the results of research conducted by the authors and does not necessarily represent the views or policies of the National Road Research Alliance, Local Road Research Board, Transportation Research and Innovation Group of the Minnesota Department of Transportation, or the University of Minnesota Duluth. This report does not contain a standard or specified technique.

The authors, The National Road Research Alliance, the Local Road Research Board, the Minnesota Department of Transportation, Transportation Research and Innovation Group and the University of Minnesota Duluth do not endorse products or manufacturers. Any trade or manufacturers' names that may appear herein do so solely because they are considered essential to this report.

LIST OF CONTENTS

LIST OF TABLES

LIST OF FIGURES

1 INTRODUCTION

The Minnesota Department of Transportation (MnDOT) constructed several fiber reinforced concrete (FRC) test cells at MnROAD in 2017. These cells were constructed as a part of a National Road Research Alliance (NRRA) funded long-term research study on fiber reinforced concrete. The main research objective of these cells is to identify and quantify the contribution of structural fibers in mitigating different distresses that typically occur in thin concrete pavements and overlays. The location of the 2017 FRC research cells at the MnROAD test facility is shown in Figure 1. Table 1 presents a summary of the designs and materials used in these test cells. A total of eight cells were constructed, among which seven cells were constructed with FRC, and one control cell was constructed with plain concrete (Cell 506). Cells 139 and 239 were constructed as ultra-thin (3-inch) and thin (4-inch) concrete pavement on unstabilized gravel base (city street design). An enhanced fiber dosage (@30% RSR; see Table 1 for the dosage information) was used in these two cells. Cells 705 and 805 were constructed as thin unbonded concrete overlays on an existing concrete pavement varying the panel size; a standard fiber dosage (@20% RSR) was used in these two cells. Cells 506 through 806 were constructed as thin concrete pavement on gravel base mainly varying with fiber content (0% to 0.75% volume fraction). Table 2 presents the paving dates of the different cells. Figure 2 shows a photograph of the fibers used in all the seven FRC cells. Table 3 presents the mix design for the FRC research cells. All the eight cells were equipped with different types of sensors for measuring responses such as, (i) dynamic strain due to wheel load, (ii) strain induced by the environmental forces, (iii) pavement temperature and gradient, and (iv) joint movement. Periodical distress (cracks, spalling, and faulting) surveys were conducted to keep track of the distresses. Falling weight deflectometer (FWD) tests are being periodically performed to determine joint performance in different seasons. This report provides a summary of the distresses observed in the abovementioned eight cells during the first year of service and an analysis and discussion of the responses measured by different sensors.

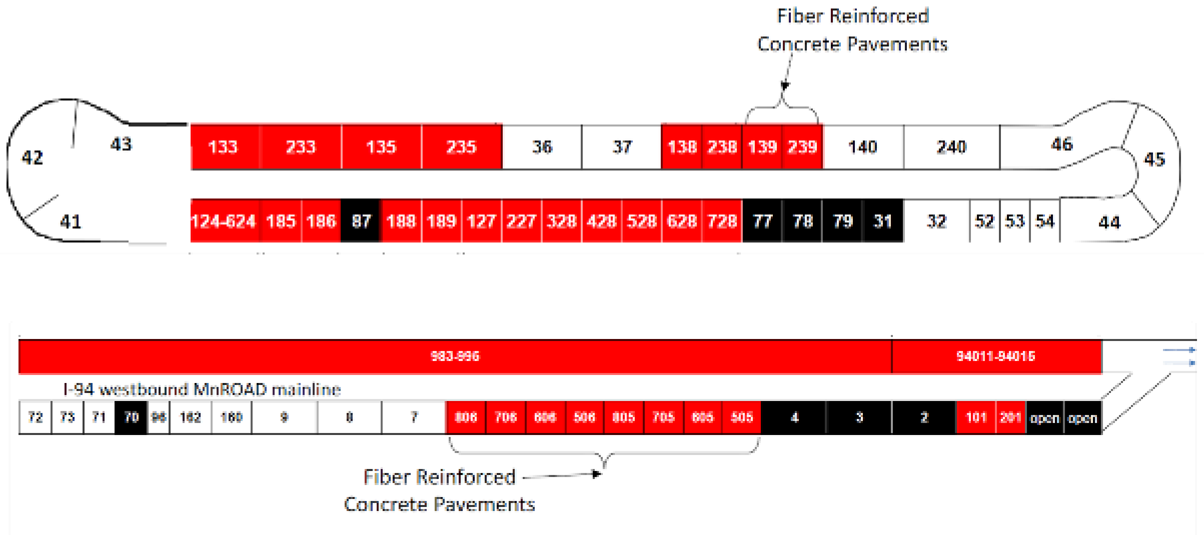

Figure 1: Location of the 2017 FRC cells at MnROAD test facility (MnDOT, 2018).

Table 1. Summary of the 2017 NRRA MnROAD test Cells constructed under FRC study.

Cell number	**Length (ft)**	**Pavement/ overlay Type**	**Underlying layer (constr. year)**	**Type of concrete/ fiber dosage***	**Panel size W ft x L ft**	**Panel thickness (inch)**
506	144	Thin pavement on gravel base	11 in. class 5Q aggregate base (2017)	*Plain concrete*	6 x 6	5
606**	138			*FRC/ standard*		
706				*FRC/ enhanced*		
806				*FRC/ high*		
139	270	Ultra-thin Pavement on gravel base	6 in. class 5 aggregate base (2017)	FRC/ enhanced	6 x 6	*3*
239	273	Thin Pavement on gravel base			6 x 6	*4*
705	144	Thin unbonded overlay on concrete pavement (w/fabric interlayer)	Concrete (1993)	FRC/ standard	*Driving:* *14 x 12* *Passing:* *12 x 12*	5
805	124				*Driving:* *6 x 12 and 8 x 12* *Passing:* *6 x 12 and 6 x 12*	5

** Fiber dosages: standard - corresponding to 20% residual strength ratio (ASTM C1609); enhanced - corresponding to 30% residual strength ratio (ASTM C1609); high – corresponding to 0.75 fibers volume fraction.*

*** Even though the design thickness was 5 inches, the actual measured thickness was found to be 6 inches*

Table 2. Paving dates and times of MnROAD 2017 FRC research cells.

CELL	Date	Approximate Time
139	7/17/2017	9:15:00 AM
239	7/17/2017	9:15:00 AM
506	6/26/2017	9:20:00 AM
606	6/27/2017	9:15:00 AM
706	6/29/2017	8:45:00 AM
806	6/30/2017	8:00:00 AM
705	9/5/2017	2:00:00 PM
805	9/5/2017	3:00:00 PM

Figure 2: Photograph of the fiber used in MnROAD 2017 FRC research cells.

Table 3. Mix designs for FRC Cells (includes control mix with no fibers) (MnDOT, 2018).

MIX/CELL	AIR (%)	WATER (lbs)	CEMENT (lbs)	FLY ASH (lbs)	FLY ASH (%)	W/C RATIO	FA #1 (lbs)	CA #1 (lbs)	FIBERS (lbs/CY)	SLUMP RANGE (in.)
MR-3A21FC 506	7.0	239	400	170	30	0.42	1222	1798	-	0.5 - 3
MR-3A21F1 705, 805, 606		248	413	177			1204	1773	5	
MR-3A21F2 139, 239, 706		252	420	180			1196	1761	8	
MR-3A21F3 806		258	430	185			1184	1743	11.66	

2 PAVEMENT DISTRESSES

2.1 Cracks and Spalling

The distresses such as cracks, spalling and faulting were documented through periodical distress surveys. Table 4 provides the dates of the crack and spalling surveys. Distress surveys were conducted by visually observing and documenting the distresses on MnDOT's distress survey sheets. Until May 2018, Cells 705 and 805 were surveyed twice, while the other cells were surveyed only once. A summary of the distresses (cracking and spalling) documented in the first year of service (until May 2018) is provided in Figure 3. This figure, however, does not include the unique distresses that developed in Cell 139. The following section elaborates the distresses observed in each cell. The distress map for all the cells, collected from MnDOT, can be found in Appendix A. *It shall be noted that all the data and pictures presented in this report for the distresses and different sensors are collected by MnDOT*.

Table 4. List of distress survey dates.

Cell	Date	
139	5/1/2018	
239	5/1/2018	
705	3/13/2018	4/25/2018
805	3/13/2018	4/25/2018
506	3/14/2018	
606	3/14/2018	
706	3/14/2018	
803	3/14/2018	

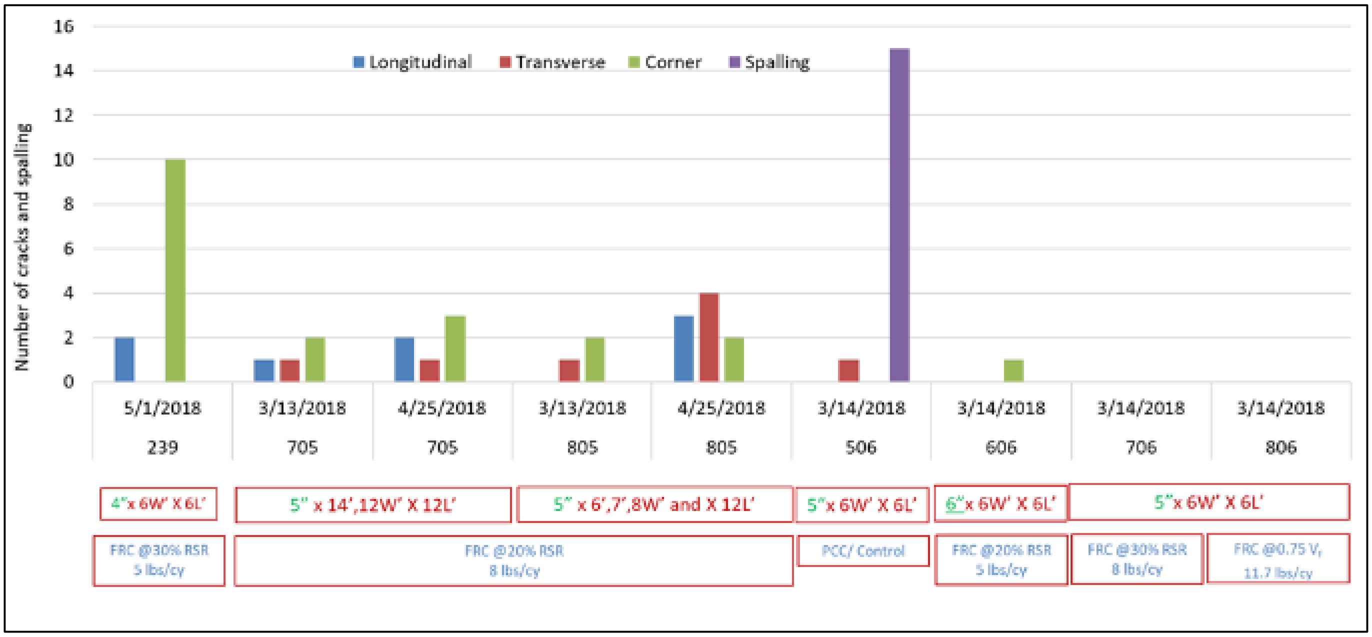

Figure 3. Summary of distress observed at the MnROAD FRC research cells during the first year of service period (Cell 139 not shown).

2.1.1 Cells 139 and 239

Cell 139 was constructed with a three-inch-thick (ultra-thin) concrete pavement on gravel base at the MnROAD low-volume test track. The slab size of this cell was 6ft x 6ft. Cell 139 was inadvertently exposed to early loads from construction trucks that were using the crossover segment to access other cells under construction, which resulted in many early-age cracks. Figure 4 shows a picture of a couple of such early-age cracks in this cell. These types of cracks continued to develop, propagate throughout the first year of service, and eventually, many slabs of this cell were shattered by the end of the summer of 2018. Besides that, there was a considerable amount of depression along the outer wheel path at some locations; this distress looked similar to rutting that occurs in asphalt pavement. Figure 5 and Figure 6 show photographs of the abovementioned distresses. While the thickness limitation (only 3-inch thick) of this cell and early-age loading were the main reasons for initiation of the failure of Cell 139, a relatively weak base layer and some drainage issues were believed to have aggravated the distresses of this cell. Based on the distresses observed in Cell 139, it can be stated that the type and quantities of the fibers used in the experiment may not be helpful when the

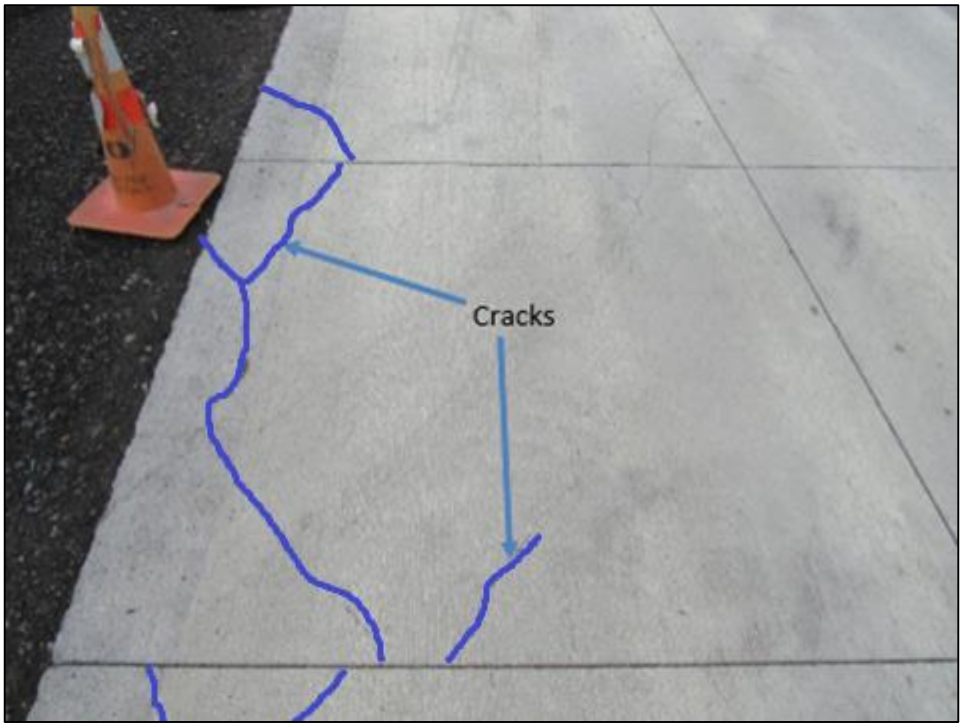

Figure 4. Cell 139 after exposure to construction truck.

Figure 5. Shattered slabs in Cell 139.

Figure 6. Depression along with the wheel path in Cell 139.

pavement is too thin (like 3 inches) and rested on a relatively weak unstabilized base layer. As many as 14 of the 44 slabs in the inside lane were eventually had to be replaced on September 27, 2018. Figure 7 shows a few photographs collected during the removal of broken slabs and construction of the replacement slabs. The replacement slabs are now 4-inch thick, with eight of them containing fiber reinforced concrete and the other six constructed with plain concrete. The fibers used in the replacement slabs are different and laterally stiffer than what was used in 2017, as shown in Figure 8a. The dosage of the fiber was 5.5 lb/cy, which corresponds to a 30% residual strength ratio. Figure 8b shows the ASTM C1609 test results for the two beam samples prepared at the site during the construction of replacement slabs in Cell 139.

(7a) Removal of shattered slabs

(7b) Close shot of the broken concrete pieces.

(7c) Fibers on the fractured face of a concrete piece.

(7d) Preparation of base layer during the construction of replacement slabs.

Figure 7. Photographs of the replacement and reconstruction on Cell 139 (outer slabs, inside lane).

(8a) Fibers used in new slabs of Cell 139.

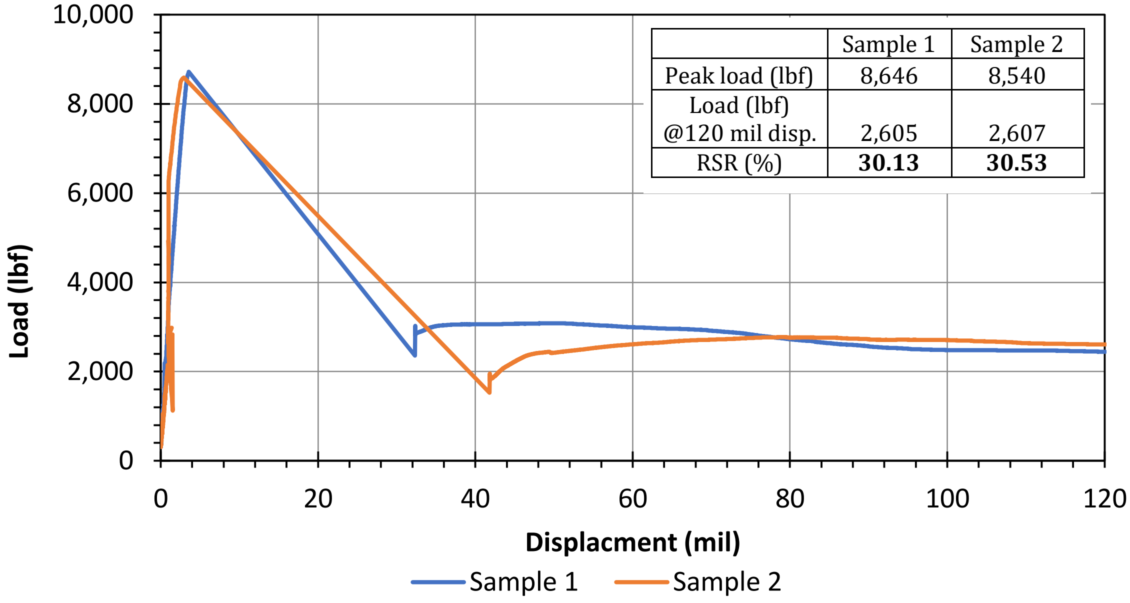

	Sample 1	Sample 2
Peak load (lbf)	8,646	8,540
Load (lbf) @120 mil disp.	2,605	2,607
RSR (%)	**30.13**	**30.53**

(8b) ASTM C1609 test results of the FRC concrete samples prepared during the construction of replacement slabs for Cell 139.

Figure 8. Photograph of fibers used in the reconstruction of Cell 139 and ASTM 1609 test results for the FRC samples.

Cell 239 on the low-volume test track, constructed as a 4-inch thick concrete pavement on gravel base with 6ft x 6ft slabs, experienced two longitudinal cracks and ten corner cracks until May 2018. Figure 9 shows a photograph of typical corner cracks that formed in Cell 239. The analysis of the distress survey map indicated that Cell 239 experienced three times more corner cracks than any other cell (excluding Cell 139). Nevertheless, this cell is performing well and significantly better than its 3-inch thick counterpart (Cell 139) for which 14 of the inside panels had to be replaced in September 2018.

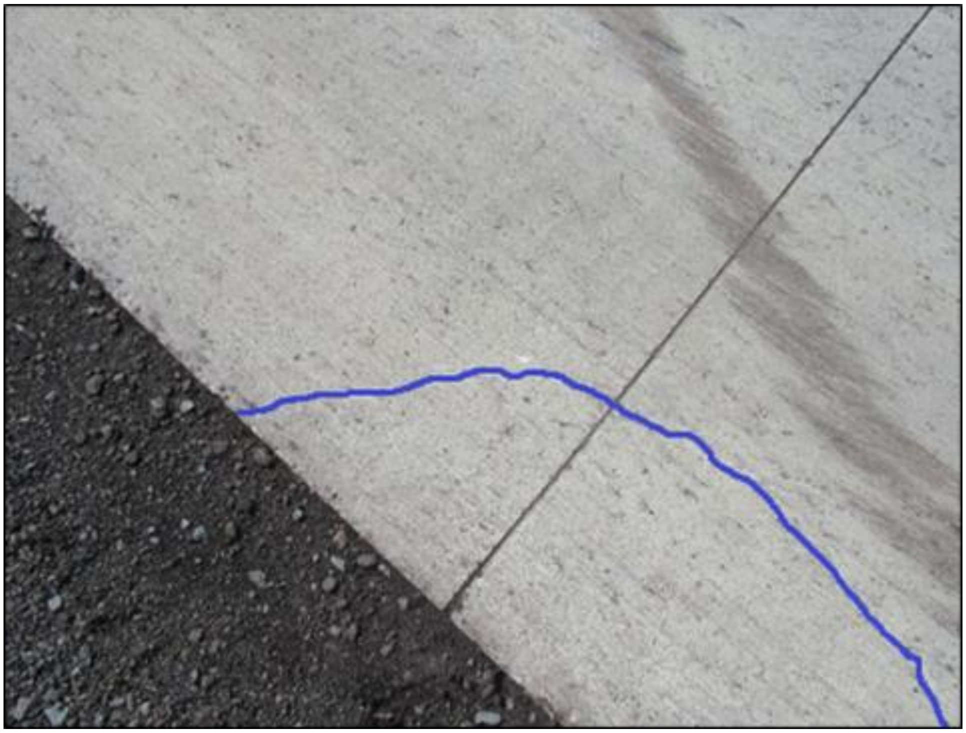

Figure 9. Corner cracks in Cell 239.

2.1.2 Cells 705 and 805

Cell 705 was constructed as a 5-inch thick unbonded concrete overlay placed over a nonwoven geotextile fabric secured to an existing 7.5-inch-thick concrete cell constructed 1993. Cell 705 was constructed with large slabs, 12 ft X 12 ft (passing lane) and 14 ft x12 ft (driving lane). This cell experienced two longitudinal cracks, one transverse crack, and three corner cracks prior to April 2018. Figure 10 to Figure 12 show photographs of typical longitudinal, transverse and corner cracks that occurred in Cell 705. Cell 805, which was also constructed with a 5-inch thick unbonded concrete overlay, has smaller slabs compared to Cell 705, as shown in Table 1. This cell experienced three longitudinal cracks, four transverse cracks, and two corner cracks prior to April 2018. Figure 13 to Figure 15 show photographs of typical cracks in Cell 805. A close investigation of the distresses observed in Cells 705 and 805 reveals that both cells had the same number of transverse and corner cracks on March 13, 2018, with the only difference being that Cell 705 had one longitudinal crack and Cell 805 had none. By April 25, 2018, the number of transverse cracks sharply increased in Cell 805. Also, by that time Cell 805 had experienced three longitudinal cracks. Based on the first-year distress data alone, even though the Cell 705 had shown slightly better performance than the Cell 805, it is too soon to draw a strong conclusion that larger FRC slabs outperform the smaller FRC slabs, in terms of cracking.

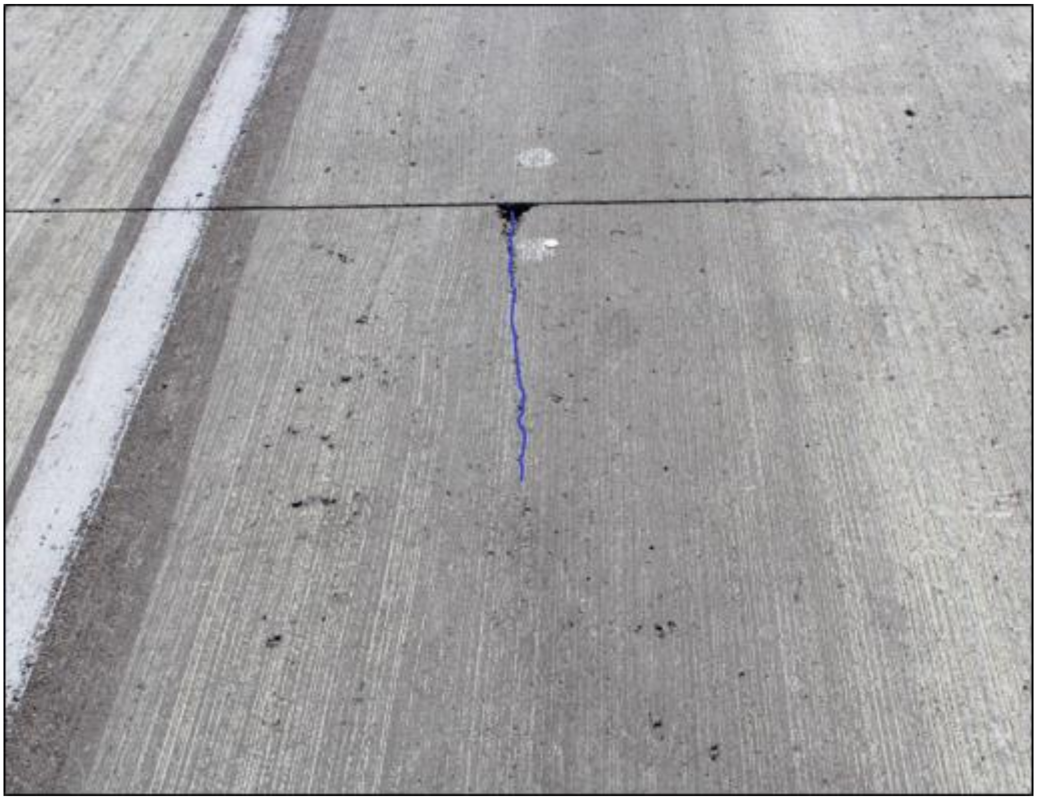

Figure 10. Longitudinal crack in Cell 705.

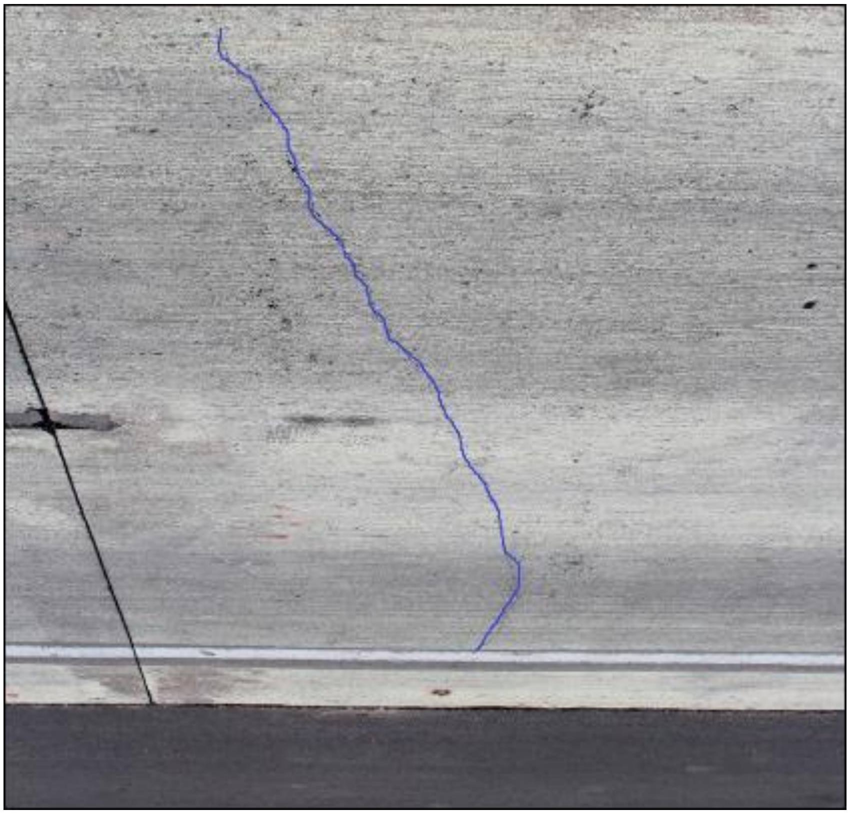

Figure 11. Transverse crack in Cell 705.

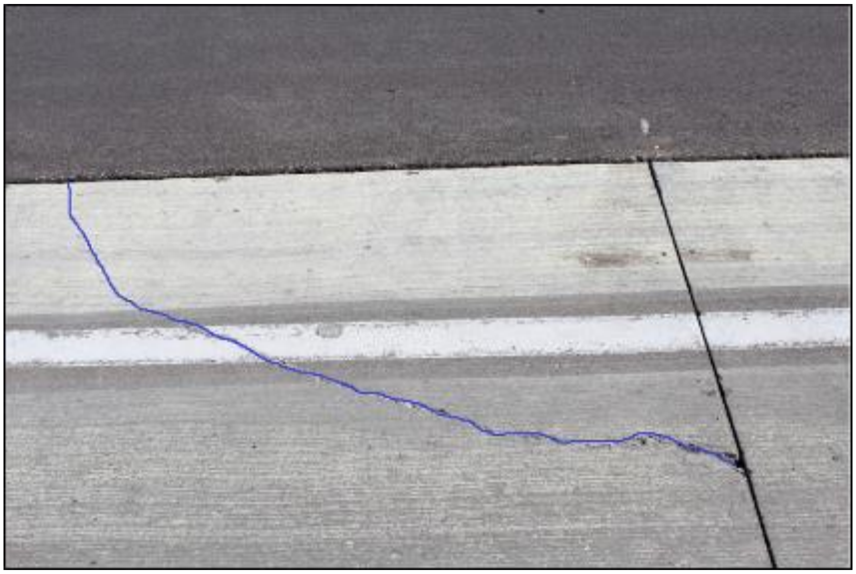

Figure 12. Corner crack in Cell 705.

Figure 13. Longitudinal crack in Cell 805.

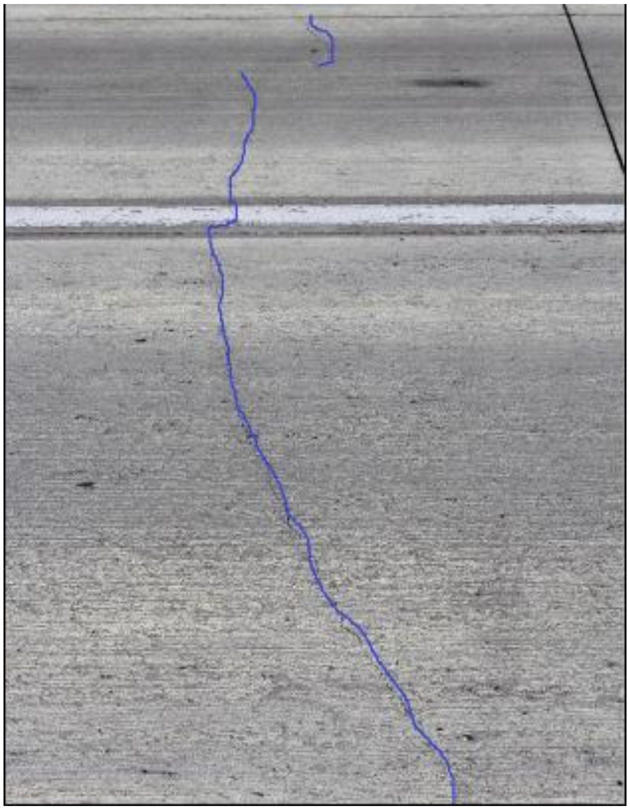

Figure 14. Transverse crack in Cell 805.

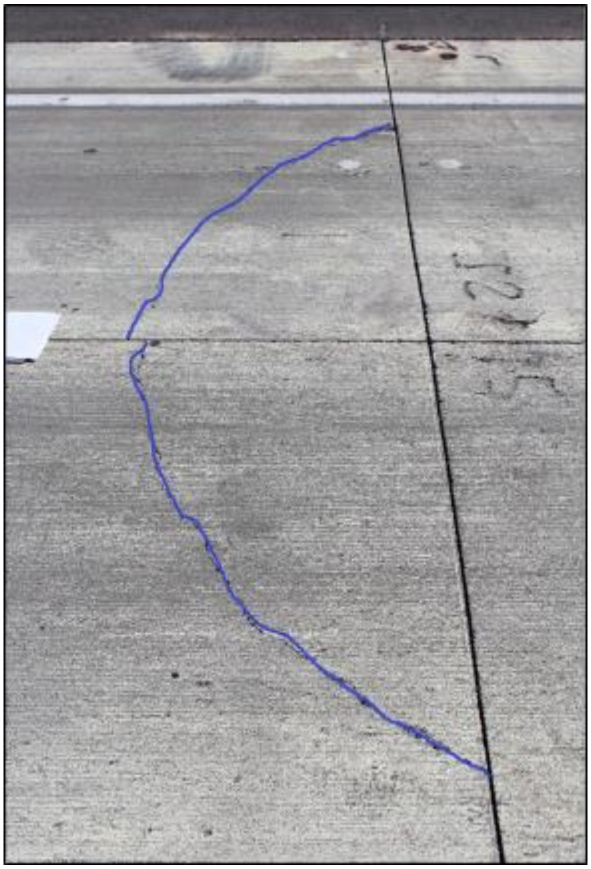

Figure 15. Corner crack in Cell 805.

2.1.3 Cells 506 through 806

Cells 506, 706 and 806 were constructed with 5-inch thick 6ft x 6ft size slabs on a gravel base. Cell 606 was constructed with 6-inch thick 6ft x 6ft size slabs. All of these cells were constructed on the Mainline test track. Cell 506, which is the control cell constructed without any fibers, experienced one transverse crack and 15 area of spalling prior to April 2018. The spalling in Cell 506 was found to be noticeably higher than other FRC cells. Figure 16 and Figure 17 show photographs of typical transverse crack and spalling that occurred in Cell 506. A comparison of the spalling in this cell with other FRC cells poses an interesting question on whether fibers help mitigate spalling. Similar findings were reported by Barman (2014). In that study, based on the laboratory test results of 4-inch-thick 5ft x 6ft size slabs, it was found that plain concrete slabs experienced significantly greater amount spalling of than the FRC slabs.

Cell 606, which was constructed with 5 lbs/cy of structural fibers, experienced one corner crack prior to April 2018. Figure 18 shows a photograph of a corner crack that occurred in the end panel of Cell 606. Cells 706 and 806, which were constructed with fiber dosages of 8 and 11.7 lbs/cy, respectively, did not experience any cracks or spalling prior to April 2018. Overall, the distress data of these four cells show that increasing the amount of fibers may decrease cracking and spalling.

Figure 16. Transverse crack in Cell 506 (control, non-FRC).

Figure 17. Spalling in Cell 506.

Figure 18. Corner crack in the last panel of Cell 606.

2.2 Joint Faulting

Joint faulting was measured on May 3, 2018, for Cells 139 and 239, and on April 28, 2018, and October 3, 2018, for the remaining cells. Joint faulting was measured on 10 randomly selected joints at four different offsets from the centerline.

2.2.1 Cells 139 and 239

Figure 19 shows the faulting measured at various transverse joints of Cells 139 and 239 prior to April 2018. It should be noted that the surface texture depth is usually around1 mm on average; therefore, any faulting readings below 1 mm may not be indicating any notable faulting. As previously mentioned, Cell 139 had experienced depression along the wheel path, so, it may not be appropriate to compare the faulting results between Cells 139 and 239. Interestingly, faulting results for Cell 239 showed negative values at almost every joint (where measured), except joint number 1. In general, a negative faulting value indicates that the leave side of the joint is at a higher elevation than the approach side. Negative faulting is usually not typical (Selezneva et. al., 2000), but since the magnitude of the faulting in Cell 239 is below -1 mm, it can be stated that there was not any notable faulting in the first of service, at least at the joints where the faulting values were recorded.

2.2.2 Cells 705 and 805

Figure 19 also shows the faulting at each joint that was measured for Cells 705 and 805 for two dates: April 26, 2018, and October 03, 2018. Both Cells 705 and 805 had shown mostly positive faulting. One noticeable observation was that the faulting at Joint number 2 of Cell 805 was higher in April 2018 than what was measured in October 2018. Even though the maximum measurements in these Cells were around 1 mm, in general, Cell 805 was closer to developing noticeable faulting.

2.2.3 Cells 506, 606, 706 and 806

Figure 19 shows the faulting magnitude at each joint that was measured for the Cells 506, 606, 706 and 806 for two dates: April 26, 2018, and October 03, 2018. Cell 506, which was constructed with plain concrete, experienced higher faulting compared to the other three cells that had fibers. Figure 20 shows a photograph of noticeable faulting in Cell 506. (note that there is a sunken corner crack in the leave slab which exaggerates the faulting in the photo.) Figure 21 shows the trend of average faulting versus fiber dosage. It can be seen that Cell 606, which was constructed with a fiber dosage of 5 lbs/cy experienced approximately 60% less faulting than the Cell 506 until October 2018. Cell 706, with a fiber dosage of 8 lb/cy, also experienced less faulting than Cell 06. Cell 806 which had the highest fiber dosage at 11.7 lbs/cy, experienced significantly lower faulting compared to any other FRC cell. Based on the designs considered in this study, early indications are that an adequate dosage of fibers is likely to reducing faulting.

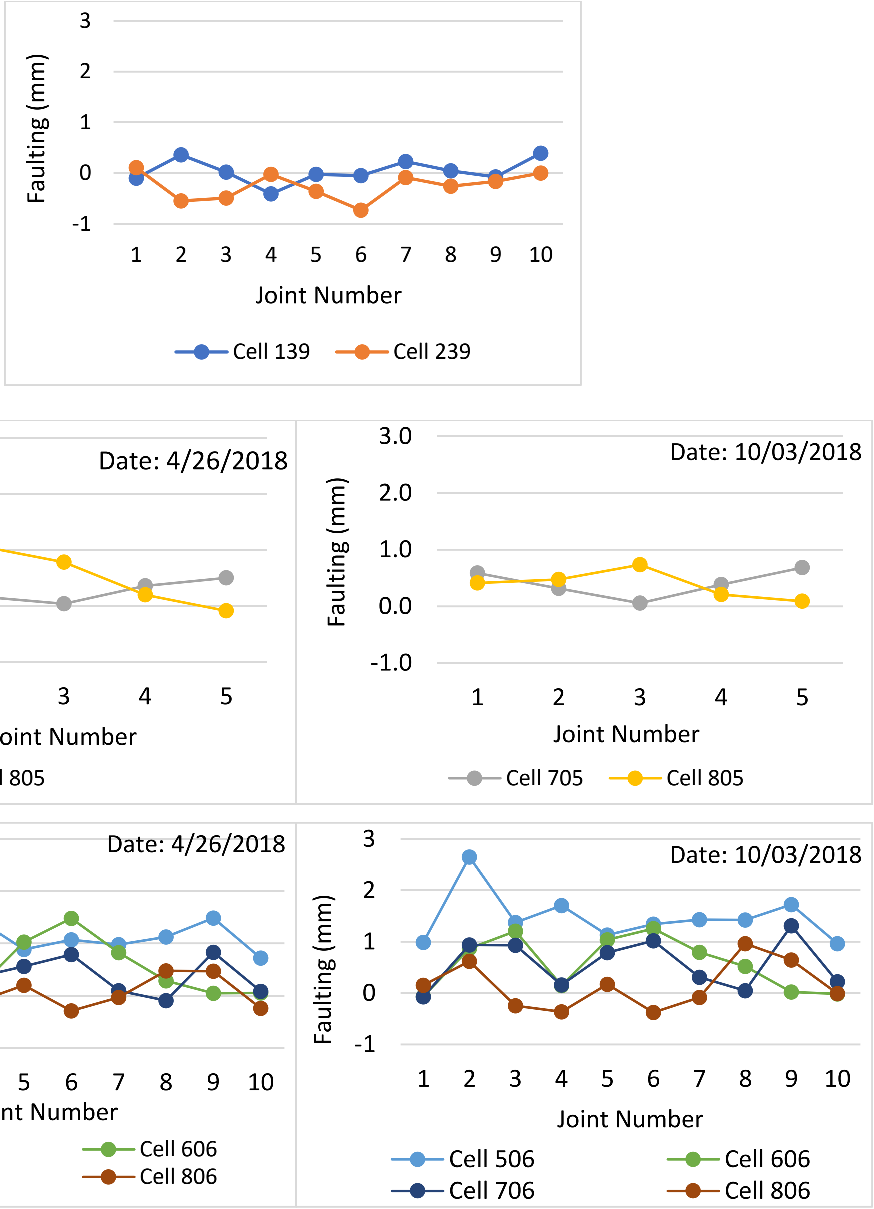

Note: The joint number in these plots are just the serial number of joints where faulting measurements were taken and different from the MnDOT's assigned joint numbers.

Figure 19. Faulting of different cells measured in April and October 2018.

Figure 20. Photograph of faulting of Cell 506 (non-FRC). Note that faulting is exaggerated due to broken corner in slab on leave slab.

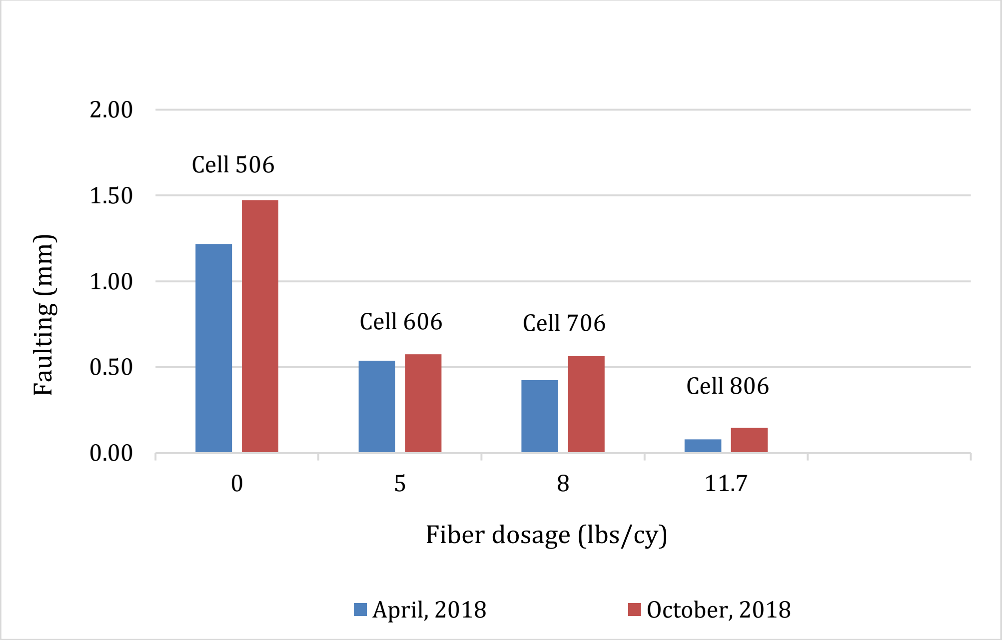

Note: Faulting for each cell is the average of all the faulting readings taken in a cell.

Figure 21. Faulting with respect to fiber dosage for Cells 506 through 806.

3 ANALYSIS OF SENSOR DATA

As previously mentioned, MnROAD 2017 FRC research cells were instrumented with four types of sensors: joint opening, dynamic strain gauge, vibrating wire strain gauge, and temperature sensors (thermocouples). Figure 22 through Figure 29 shows the sensor plans for all eight cells. This section provides an analysis of the data collected from these sensors so far.

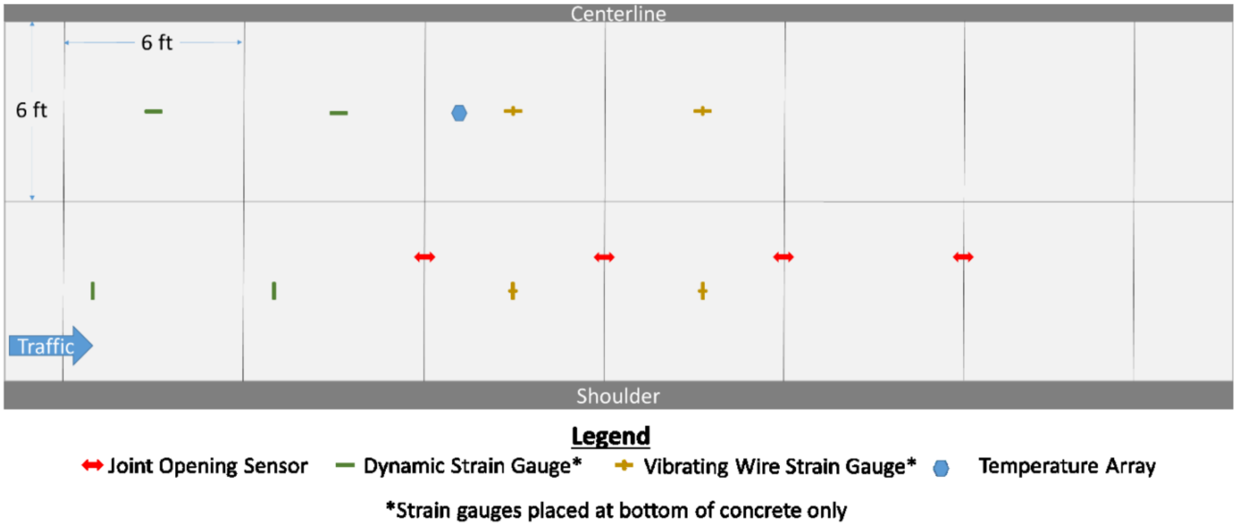

Figure 22. Sensor plan for Cell 139, inner lane (MnDOT, 2018).

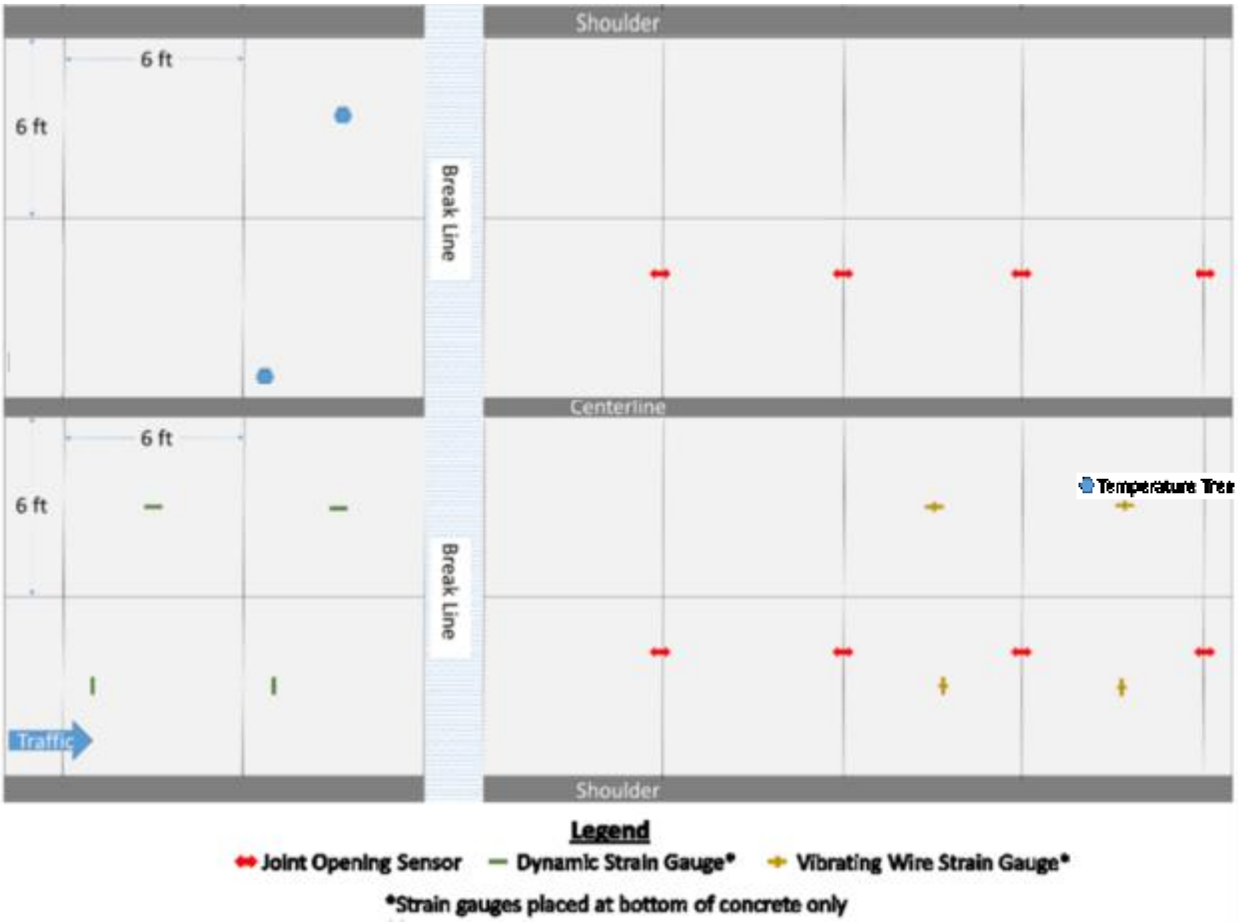

Note: Temperature trees are installed in the outer lane.

Figure 23. Sensor plan for Cell 239, inner lane (MnDOT, 2018).

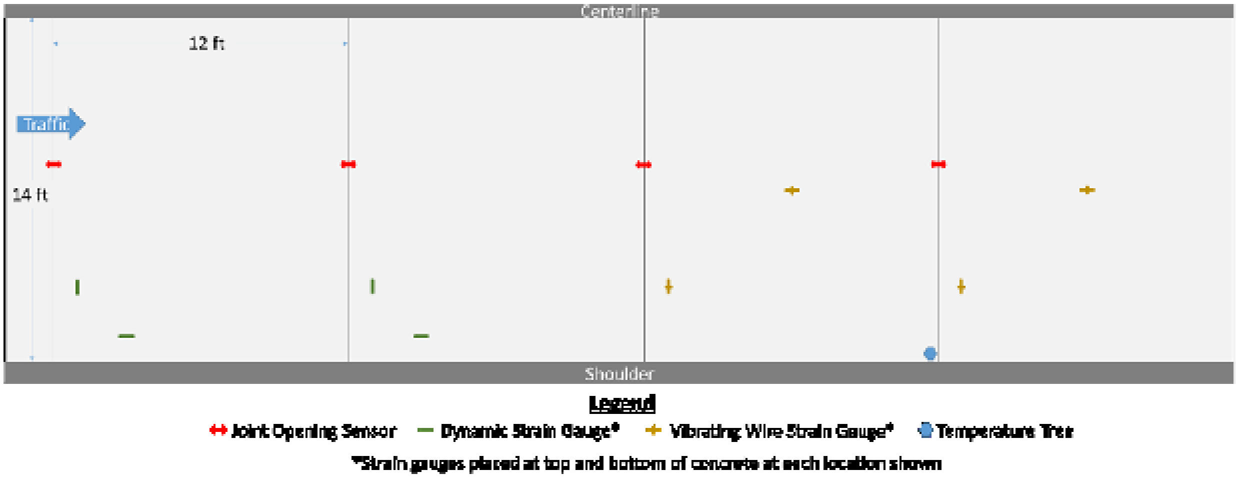

Figure 24. Sensor plan for Cell 705, driving lane (MnDOT, 2018).

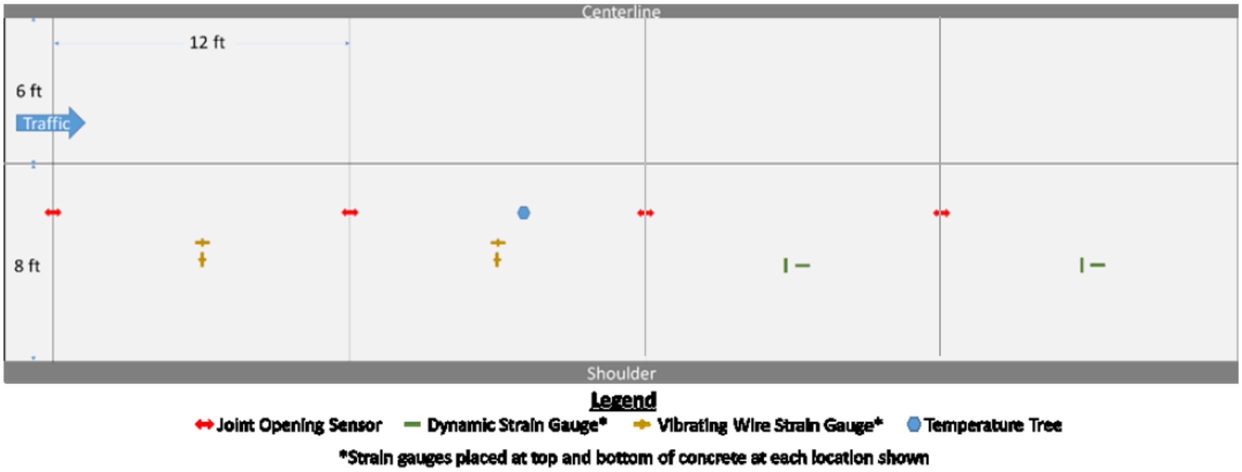

Figure 25. Sensor plan for Cell 805, driving lane (MnDOT, 2018).

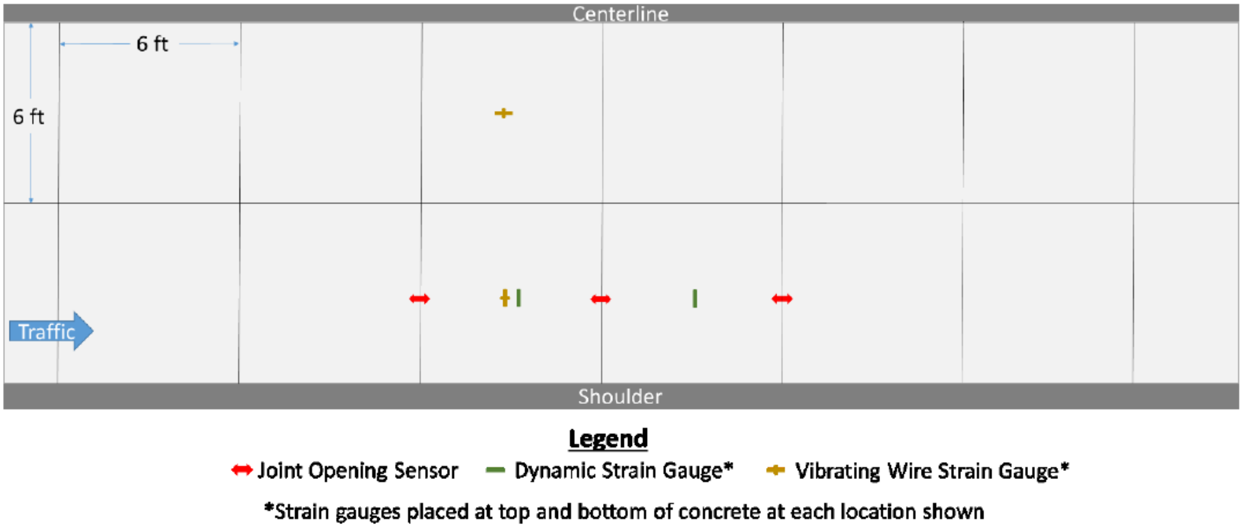

Figure 26. Sensor plan for Cell 506, driving lane (MnDOT, 2018).

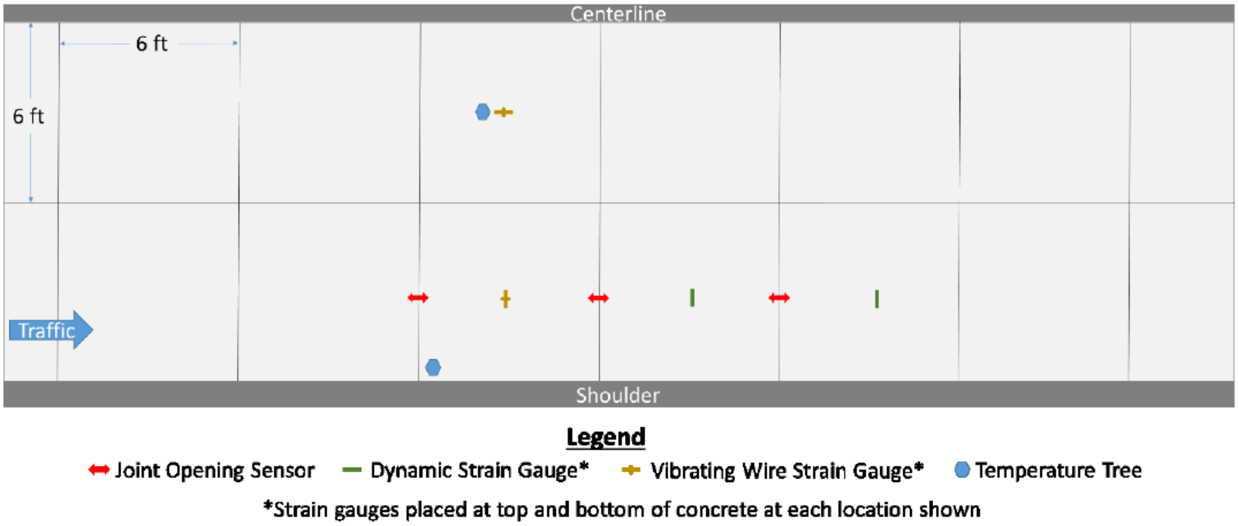

Figure 27. Sensor plan for Cell 606, driving lane.

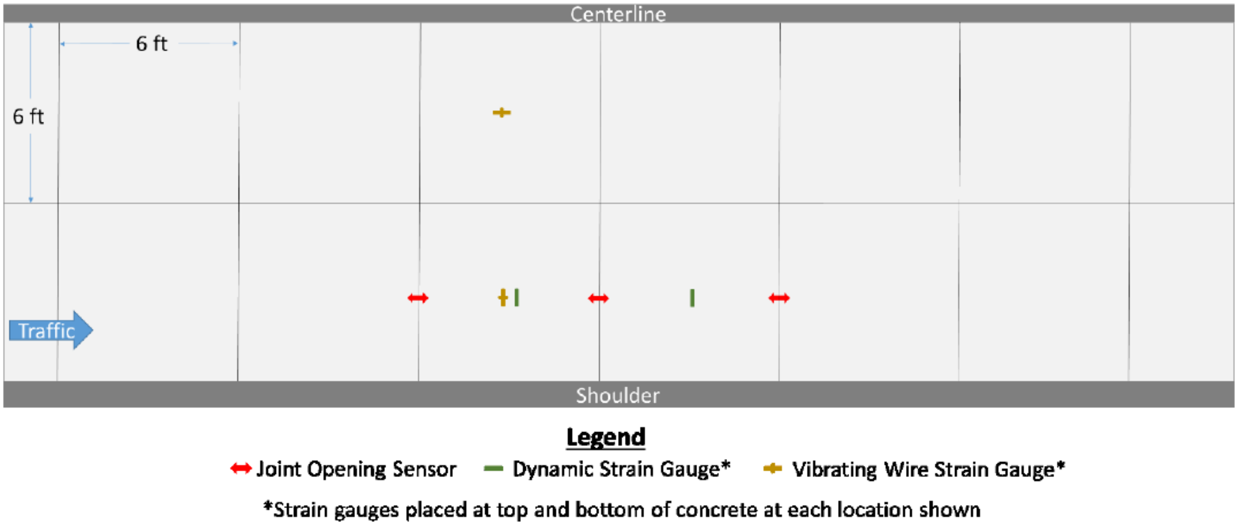

Figure 28. Sensor plan for Cell 706, driving lane.

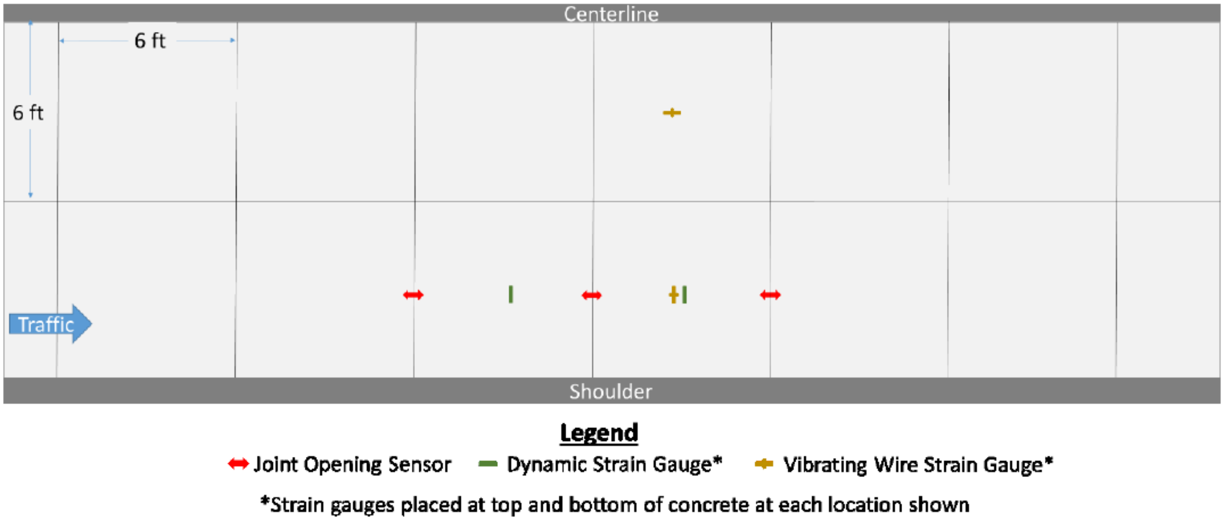

Figure 29. Sensor plan for Cell 806, driving lane.

3.1 Temperature

Daily and seasonal variations of temperature have a significant influence on the performance of the concrete pavement. A large number of thermocouple sensors were installed at MnROAD 2017 FRC research cells to capture the variations of temperature as well as temperature-gradient in the concrete slab. Thermocouples were installed at different depths within and beneath the slabs. Figure 30 shows an example of a thermocouple sensor tree installed in cells 139, 239, 705, 805, and 606. One sensor tree was installed in each of the Cells 139, 705, and 805; two trees were installed in Cells 239 and 606, located at different offsets from the centerline. For this report, to distinguish between the two sensor trees in Cells 239 and 606, the farthest sensor tree from the centerline was designated as the outer sensor and the sensor tree closest to the centerline as the inner sensor. All of the thermocouple sensors were programmed to record temperature data every 15 minutes. In addition to collecting pavement temperature data, ambient temperature data is also collected at MnROAD using an external weather station, which is capable of collecting other ambient parameters like, precipitation, relative humidity, wind speed, wind direction, etc. Figure 31 shows the variation of the ambient temperatures collected from mid-June 2017 to mid-September 2018. As shown in this figure, it can be seen that the December 31, 2017, was the coldest day with a -30°C temperature and February 4, 2017, was the second coldest day at MnROAD with -23.5°C temperature. On the other side, May 28, 2018, was the warmest day with a 37°C temperature.

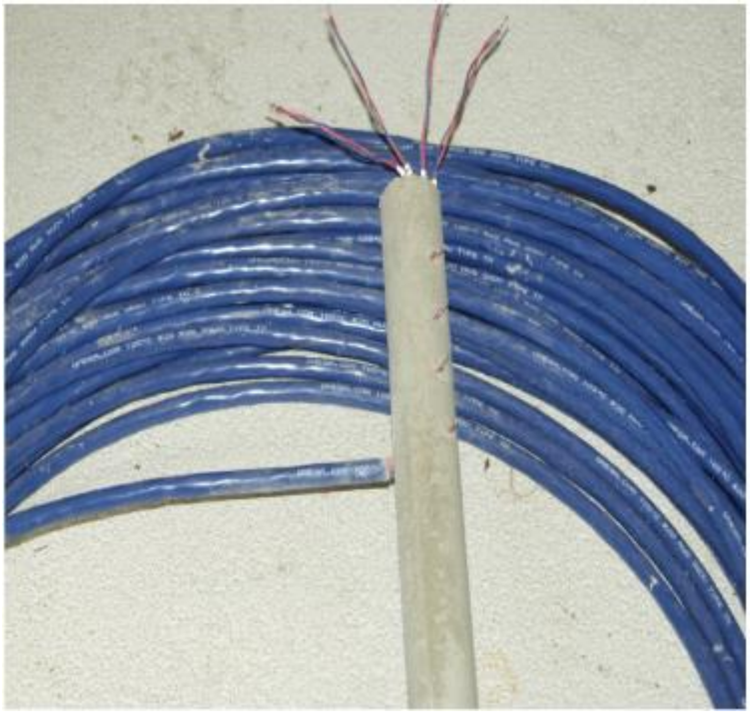

Figure 30. Example of a thermocouple sensor tree.

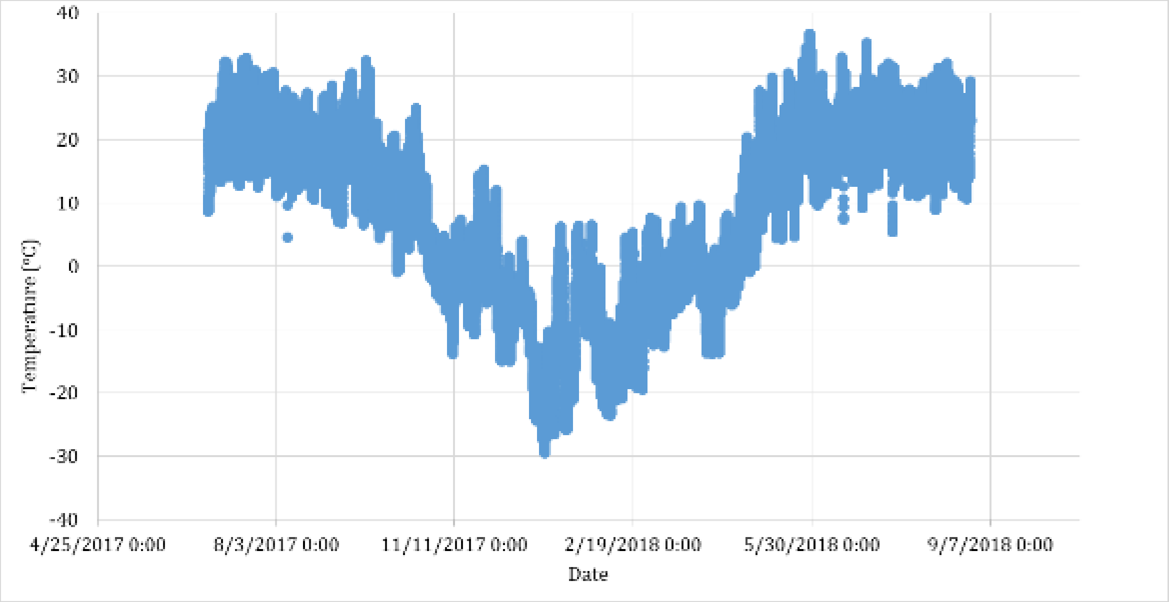

Figure 31. Ambient temperature at the MnROAD Project site.

3.1.1 Pavement Temperature

The pavement slab temperature data for the cells equipped with thermocouples are shown in Figure 32 through Figure 38. These figures contain several plots, each with temperatures recorded at different depths of the slab. As expected, the general trends of the seasonal temperature variations are similar for all the cells and align well with the ambient temperature trend, shown in Figure 31. The maximum and minimum temperatures recorded for each cell and their respective occurrence dates and times are summarized in Table 5. The dates of the coldest temperatures for all the cells were recorded on December 31, 2017, while the majority of the cells had experienced their warmest day on May 28, 2018. Cell 139 experienced the warmest day on the date of it's paving, i. e. July 17, 2017. The inner thermocouple tree of the Cell 239 also experienced the warmest temperature on July 17, 2017, on its paving date. These observations indicate that the Cells 139 and 239 were constructed on a relatively warmer day, and the recorded highest temperatures probably were influenced by the heat of hydration of the cement. Notably, the coldest and warmest temperatures for all the cells were recorded at 8:45 AM and 2:45 PM, respectively.

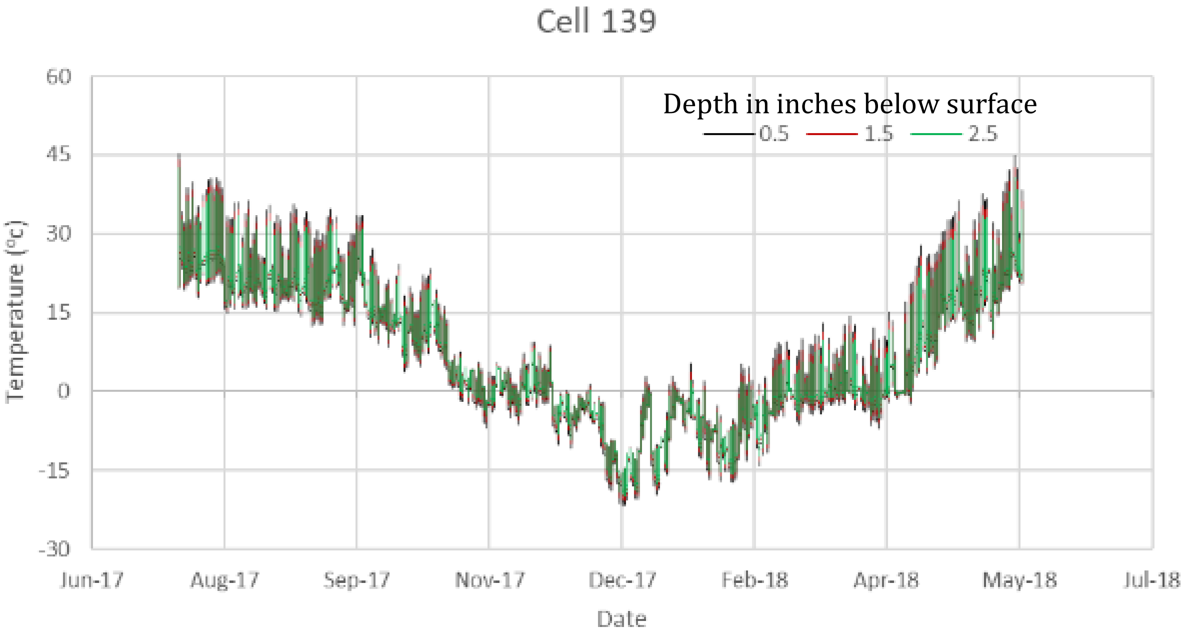

Figure 32. Temperature profile of Cell 139.

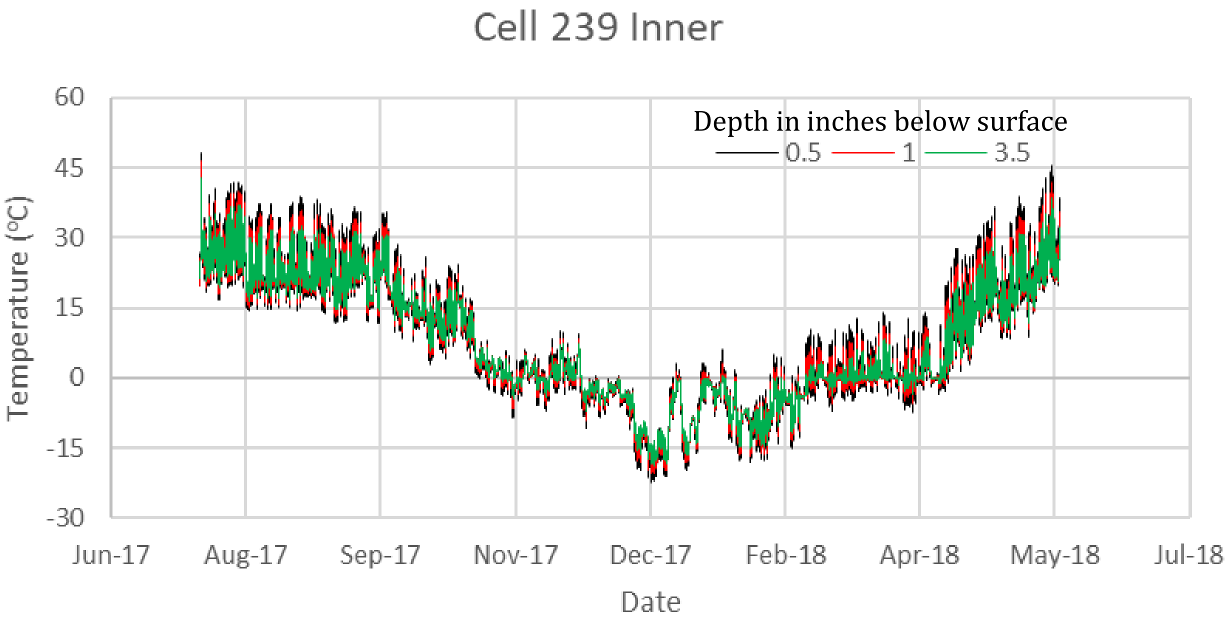

Figure 33. Temperature profile of Cell 239 inner lane.

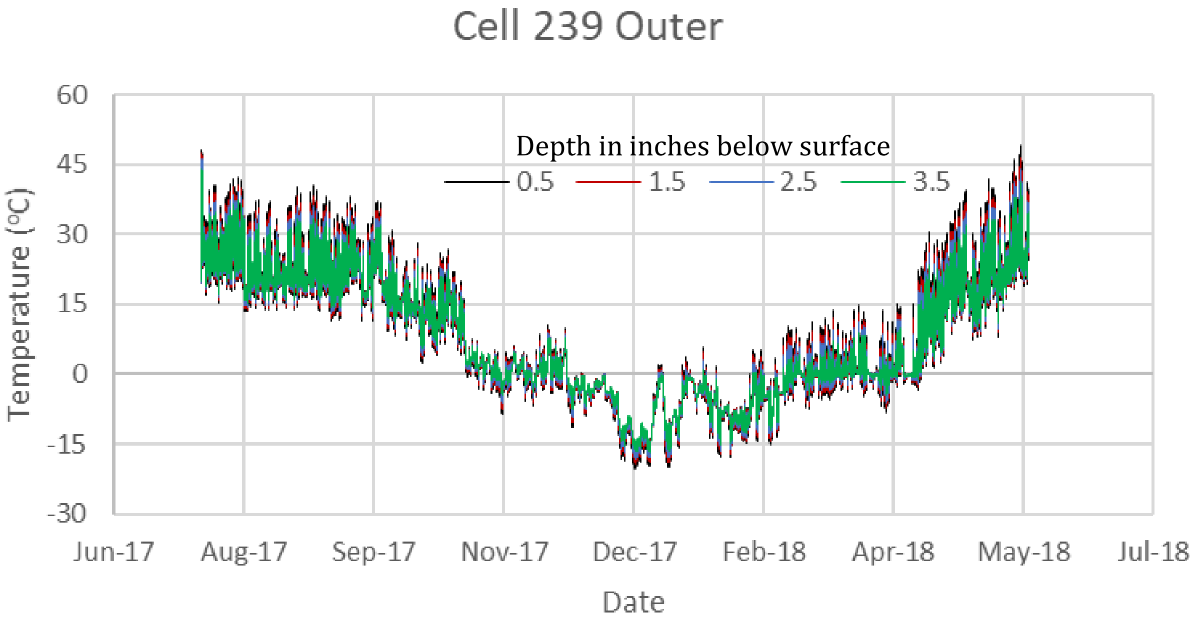

Figure 34. Temperature profile of Cell 239 outer lane.

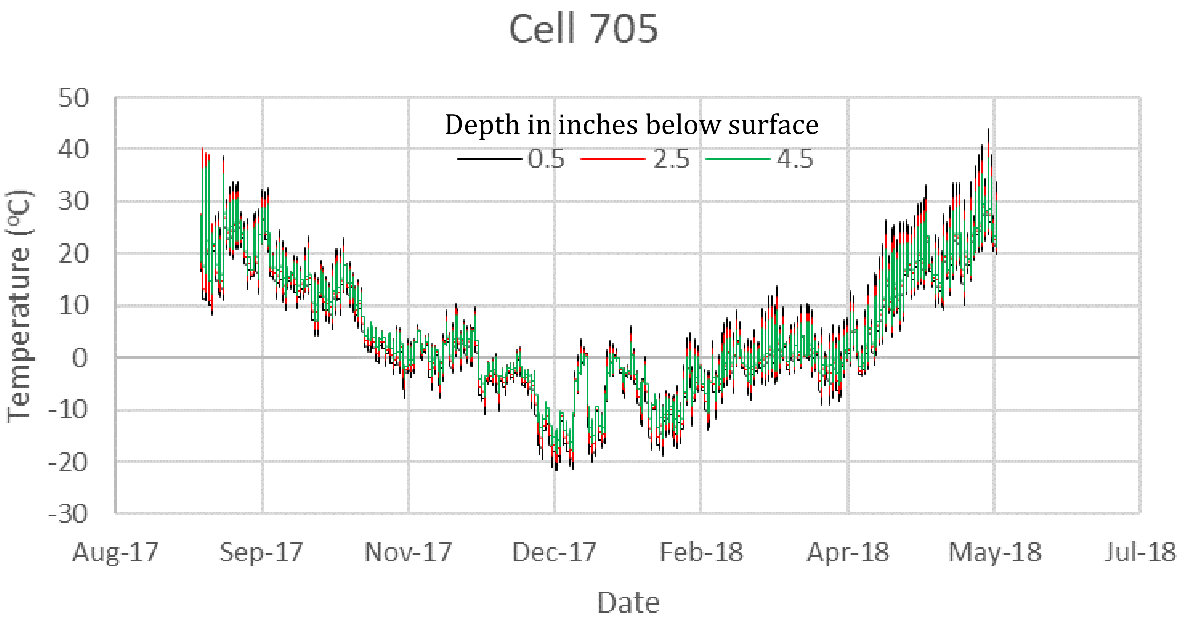

Figure 35. Temperature profile of Cell 705.

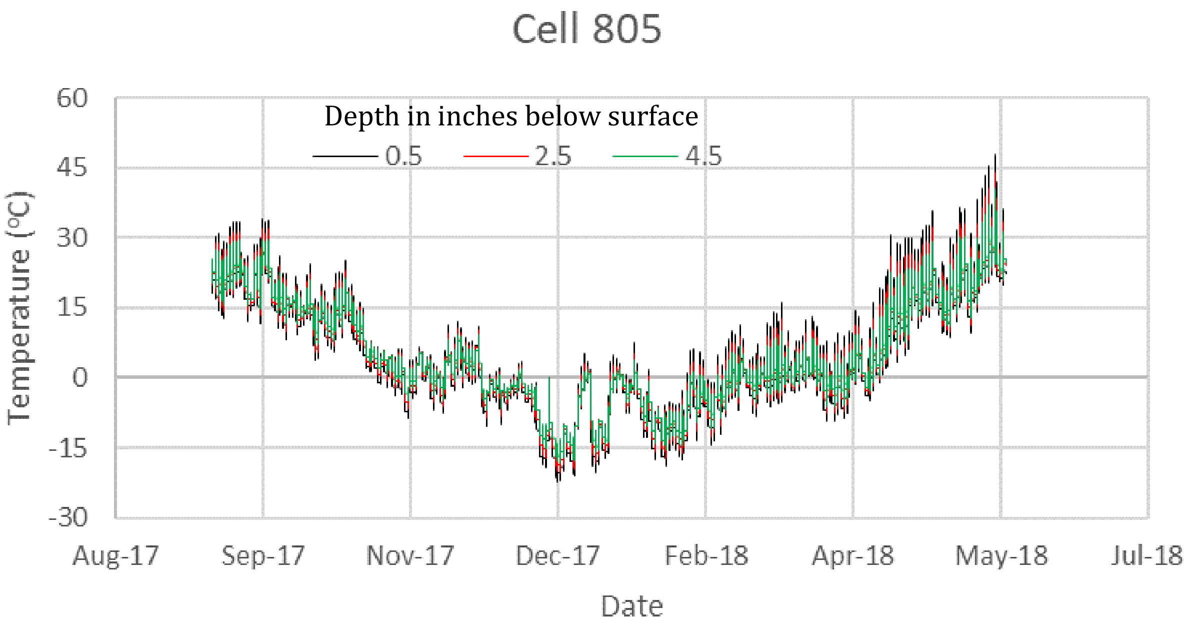

Figure 36. Temperature profile of 805.

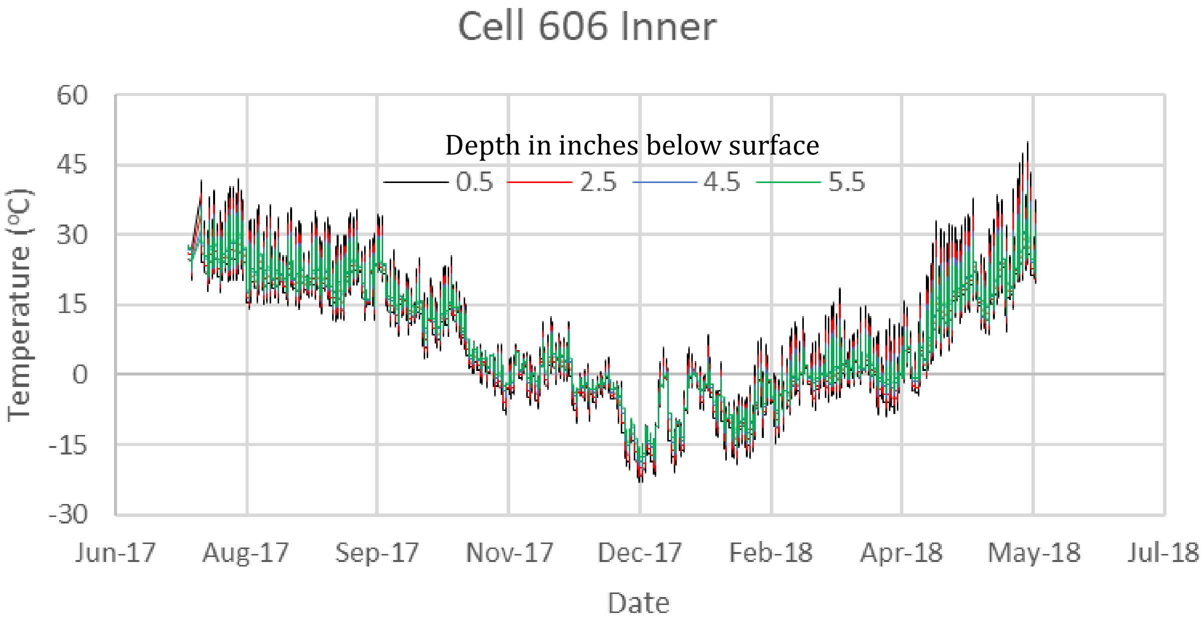

Figure 37. Temperature profile of Cell 606 inner lane.

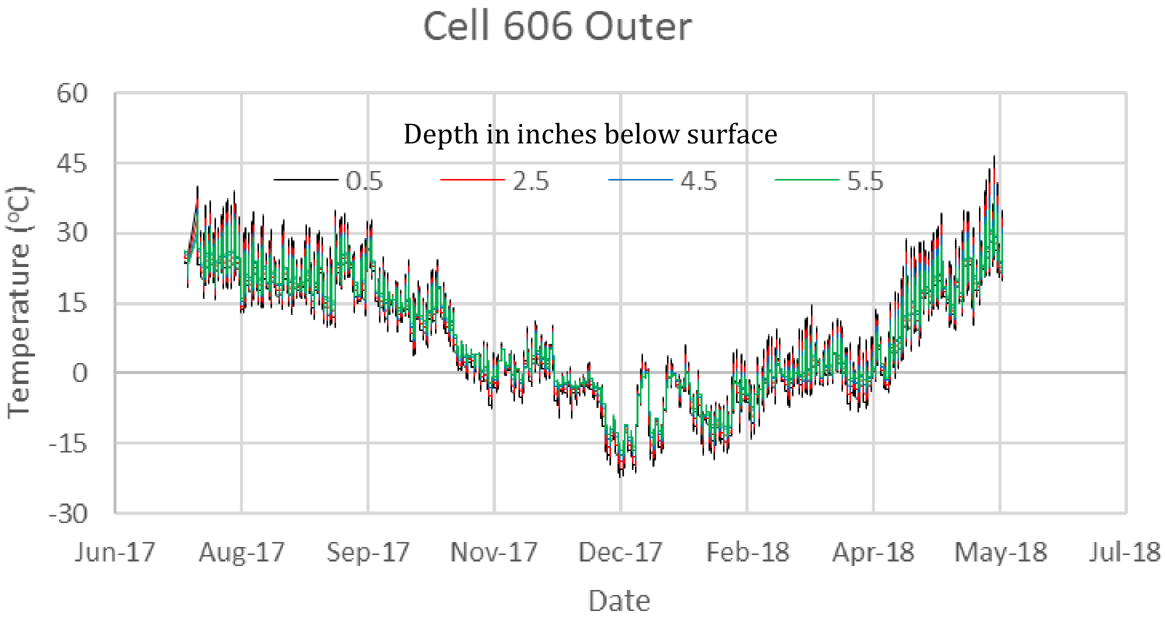

Figure 38. Temperature profile of Cell 606 outer lane.

Table 5. Cell extreme temperatures and respective dates and times.

Cell		Temperature C	Date	Time
139	Max	45.3	7/17/2017	2:45:00 PM
	Min	-21.7	12/31/2017	8:45:00 AM
239	Max Outer	49.1	5/28/2018	2:15:00 PM
	Min Outer	-20.3	12/31/2017	8:30:00 AM
	Max Inner	48.3	7/17/2017	2:45:00 PM
	Min Inner	-22.4	12/31/2017	8:15:00 AM
705	Max	44.0	5/28/2018	4:15:00 PM
	Min	-21.8	12/31/2017	8:45:00 AM
805	Max	47.9	5/28/2018	2:45:00 PM
	Min	-22.4	12/31/2017	8:45:00 AM
606	Max Inner	49.8	5/28/2018	3:00:00 PM
	Min Inner	-23.3	12/31/2017	8:15:00 AM
	Max Outer	46.7	5/28/2018	3:45:00 PM
	Min Outer	-22.2	12/31/2017	8:45:00 AM

Note: Temperature reading collected at different depths of slabs are considered.

The relationship between the temperature and depth of the slab was studied to determine the nature of the temperature variation (either linear or non-linear). Figure 39 and Figure 40 show the temperature profiles of various cells resulted in during their coldest and warmest temperature events, respectively. The general nature of the temperature variation, at least during the extreme temperature events, were found to be linear, except for the Cell 239, which showed a slightly non-linear nature. As almost all the cells experienced somewhat linear temperature gradients, the analysis has been restricted to the linear temperature gradient only. However, further analysis will be performed to verify the nature of the temperature gradients at intermediate temperature events and will be reported in the future task reports.

3.2 Linear Temperature Gradient (LTG)

The linear temperature gradient (LTG) was determined by subtracting the temperature of the bottommost sensor from the topmost sensor of a slab and then divided by the vertical distance between these sensor locations in question. A negative temperature gradient indicates that the pavement is colder at the top and warmer at the bottom and the positive temperature gradients indicate the opposite scenario. At negative and positive temperature gradients, slabs experience upward curling and downward curling, respectively. In this work, temperature gradients were calculated at every 15 minutes, then the monthly average positive and negative LTGs were determined as shown in Table 6 to Table 8.

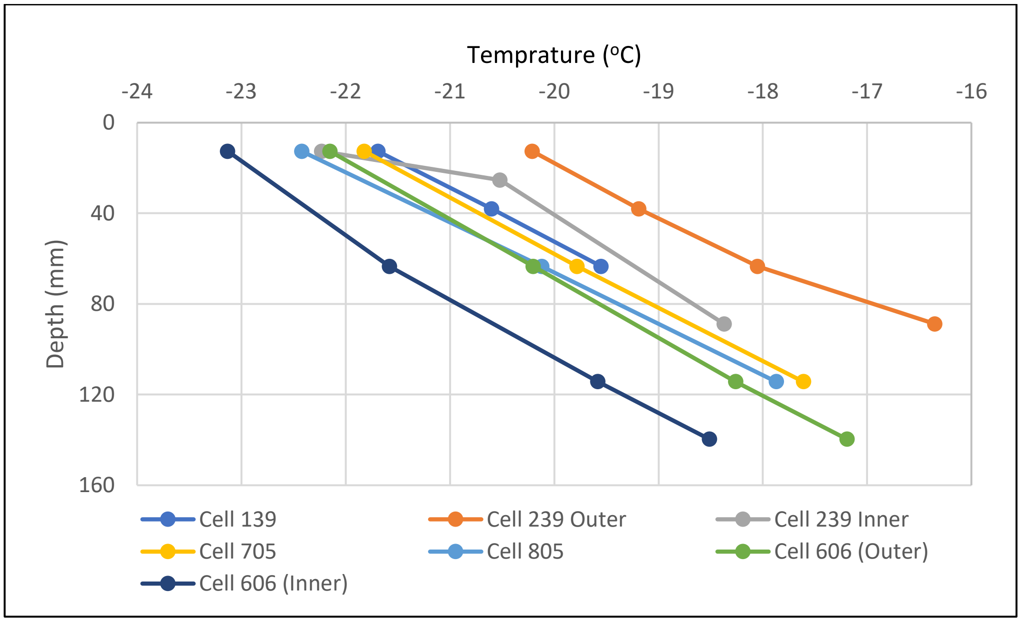

Figure 39. Temperature vs slab depth on the coldest day, December 31, 2017, 8:45 AM.

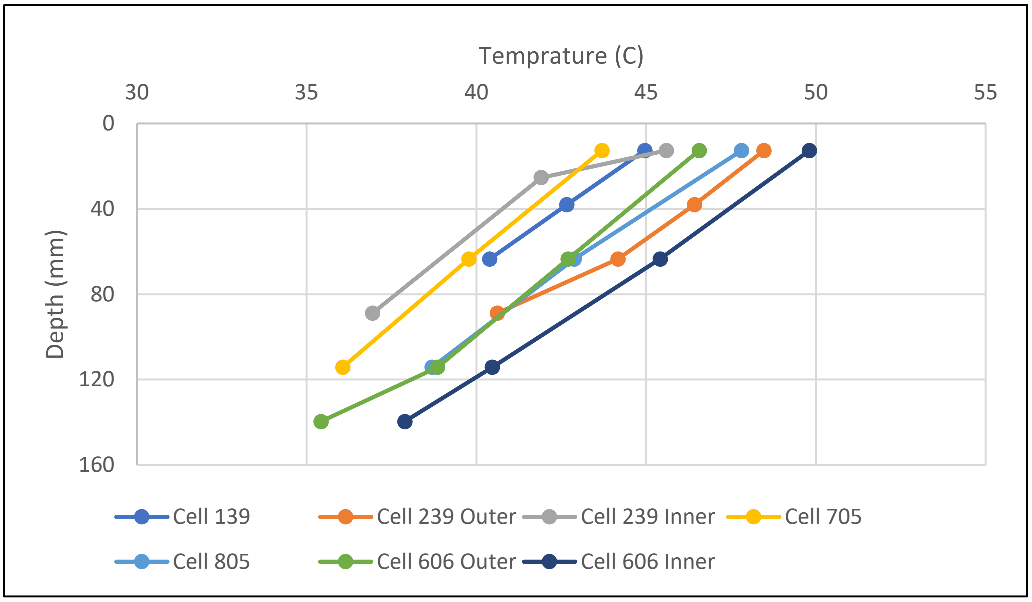

Figure 40**.** Temperature vs slab depth on the warmest day, May 28, 2018, 2:45 PM.

Table 6 shows the monthly average LTG for Cells 139 and 239. Cell 139 had the highest positive LTG of 1.09^{o}C/cm in April and May 2018, and the highest negative LTG of -0.648 ^{o}C/cm in July 2017. The outer sensor tree of Cell 239 had the highest LTG of 1.61 ^{o}C/cm in April 2018 and the highest negative LTG of -1.07^{o}C/cm in May 2018, while the outer sensor tree had the highest positive LTG of 1.16^{o}C/cm in May 2018 and the lowest LTG of -1.07 ^{o}C/cm in August 2017.

Comparing the inner sensor tree to the outer sensor tree in Cell 239, it can be seen that the outer sensor tree showed larger temperature gradients. Also, the linear temperature gradients of the inner sensor trees of Cells 139 and 239 were found to be similar.

Table 6. Linear temperature gradient results for Cells 139 and 239.

Temperature Gradient (°C/cm)						
	Cell 139 (3-inch)		**Cell 239 (4-inch)**			
	Inner		**Outer**		**Inner**	
Month	**Negative**	**Positive**	**Negative**	**Positive**	**Negative**	**Positive**
Jul-17	**-0.65**	0.81	-0.91	0.95	-0.59	0.92
Aug-17	-0.585	0.87	-0.68	1.25	**-0.61**	0.98
Sep-17	-0.52	0.79	-0.85	1.08	-0.49	0.84
Oct-17	-0.38	0.72	-0.45	0.94	-0.41	0.75
Nov-17	-0.49	0.60	-0.59	0.80	-0.51	0.64
Dec-17	-0.48	0.41	-0.58	0.40	-0.52	0.51
Jan-18	-0.51	0.68	-0.67	0.72	-0.47	0.70
Feb-18	-0.51	0.98	-0.64	1.06	-0.51	1.0
Mar-18	-0.43	1.04	-0.52	1.15	-0.47	1.12
Apr-18	-0.52	**1.09**	-0.66	**1.61**	-0.56	1.15
May-18	-0.62	**1.09**	**-1.07**	1.41	-0.53	**1.16**

* Data collection for Cells 139 and 239 started on July 17th, 2017

Cells 705 and 805 are thin unbonded fiber reinforced concrete overlays on concrete pavement. Table 7 shows the monthly average LTGs for both Cells 705 and 805. Cell 705 had a maximum positive of 0.81 °C/cm and a maximum negative of -0.74 °C/cm, while Cell 805 had a maximum positive LTG of 1.04 °C/cm and a maximum negative LTG of -0.50 °C/cm. These two cells experienced almost similar LTGs, except the September LTG of Cell 705, which was surprisingly very high compared to all the negative LTGs recorded for these two cells. For both cells, the maximum positive LTGs occurred in May 2018. The maximum negative LTG for Cell 705 occurred in September 2017, and for Cell 805, it occurred in May 2018. Overall the maximums LTGs for Cell 805, which were constructed with 6 ft wide slabs, were slightly higher than Cell 705 that had 12 ft wide slabs.

Table 7. Linear temperature gradient results for Cells 705 and 805.

Temperature Gradient (°C/cm)				
	Cell 705 (5-inch)		Cell 805 (5-inch)	
Month	**Negative**	**Positive**	**Negative**	**Positive**
Sep-17	**-0.74**	0.53	-0.39	0.57
Oct-17	-0.35	0.41	-0.38	0.57
Nov-17	-0.40	0.35	-0.41	0.48
Dec-17	-0.45	0.19	-0.47	0.30
Jan-18	**-0.49**	0.44	**-0.50**	0.56
Feb-18	-0.44	0.53	-0.46	0.66
Mar-18	-0.37	0.64	-0.43	0.83
Apr-18	-0.39	0.74	-0.43	1.01
May-18	-0.35	**0.81**	-0.48	**1.04**

* Data collection for cell 805 started on September 5th 2017

Out of the four Cells 506 through 806 in the mainline test track, only Cell 606 has thermocouple trees. Two sensor trees were included in this cell. The LTGs for both sensor trees are provided in Table 8. For the inner sensor tree, the maximum positive LTG was 1.12 °C/cm, and the maximum negative TG was -0.53 °C/cm. The outer sensor tree has maximum positive and negative LTGs of 0.92 °C/cm and -0.47 °C/cm, respectively. For both outer and inner sensor trees, the positive maximum LTG occurred in May of 2018. The maximum negative LTGs for the outer and inner sensor trees occurred in January 2018 and May 2018, respectively. Comparing the outer sensor tree, the inner sensor tree of Cell 606 shows slightly greater LTGs. Comparing all the cells, it was found that the maximum positive temperature gradients mostly occurred during the warmer temperatures (May 2018).

Table 8. Linear temperature gradient results for Cell 606.

Temperature Gradient (°C/cm)				
	Cell 606 Inner (5-inch)		**Cell 606 Outer (5-inch)**	
Month	**Negative**	**Positive**	**Negative**	**Positive**
Jul-17	-0.38	0.74	-0.28	0.62
Aug-17	**-0.50**	0.74	-0.33	0.62
Sep-17	-0.37	0.64	-0.33	0.62
Oct-17	-0.34	0.55	-0.34	0.42
Nov-17	-0.43	0.52	-0.41	0.39
Dec-17	-0.47	0.33	-0.43	0.22
Jan-18	-0.49	0.61	**-0.47**	0.49
Feb-18	-0.48	0.72	-0.43	0.56
Mar-18	-0.47	0.91	-0.39	0.73
Apr-18	-0.47	1.06	-0.44	0.84
May-18	-0.53	**1.12**	-0.34	**0.92**

*Data collection started July 7th, 2017

3.2.1 Frequency Distribution of Linear Temperature Gradients

In order to determine the common LTG ranges, the frequency distributions of the LTGs were plotted for each cell as shown in Figure 41. The LTG range and the corresponding frequencies were plotted for each cell in this figure. The frequency distributions of Cell 139 and 239 did not show a great difference. In Cell 239, the trends between the two sensor trees were similar with the exception that the outer sensor tree had a higher number of frequencies for an LTG range of -0.5 to -0.25 °C/cm than the inner one. The Cell 239 inner sensor tree and Cell 139 provided very similar LTGs. The maximum frequency for Cell 139 and the inner tree in Cell 239 occurred in the LTG range of -0.15 to 0 °C/cm. The maximum frequency for the outer sensor tree in Cell 239 occurred in the range of -0.5 and -0.25 °C/cm. Cell 705 and 805 have similar trends with the maximum for both cells occurring between -0.15 and 0 °C/cm. The trends of the LTGs measured at the inner and outer trees of Cell 606 were also the same with the maximum frequency occurring between -0.15 and 0 ^{o}C/cm.

Figure 42 shows the percent time that the LTG was positive and negative. Overall, the percent time that the LTG was positive or negative was consistent between the cells. It appeared that all the cells experienced negative temperature gradients for more than 60 percent time.

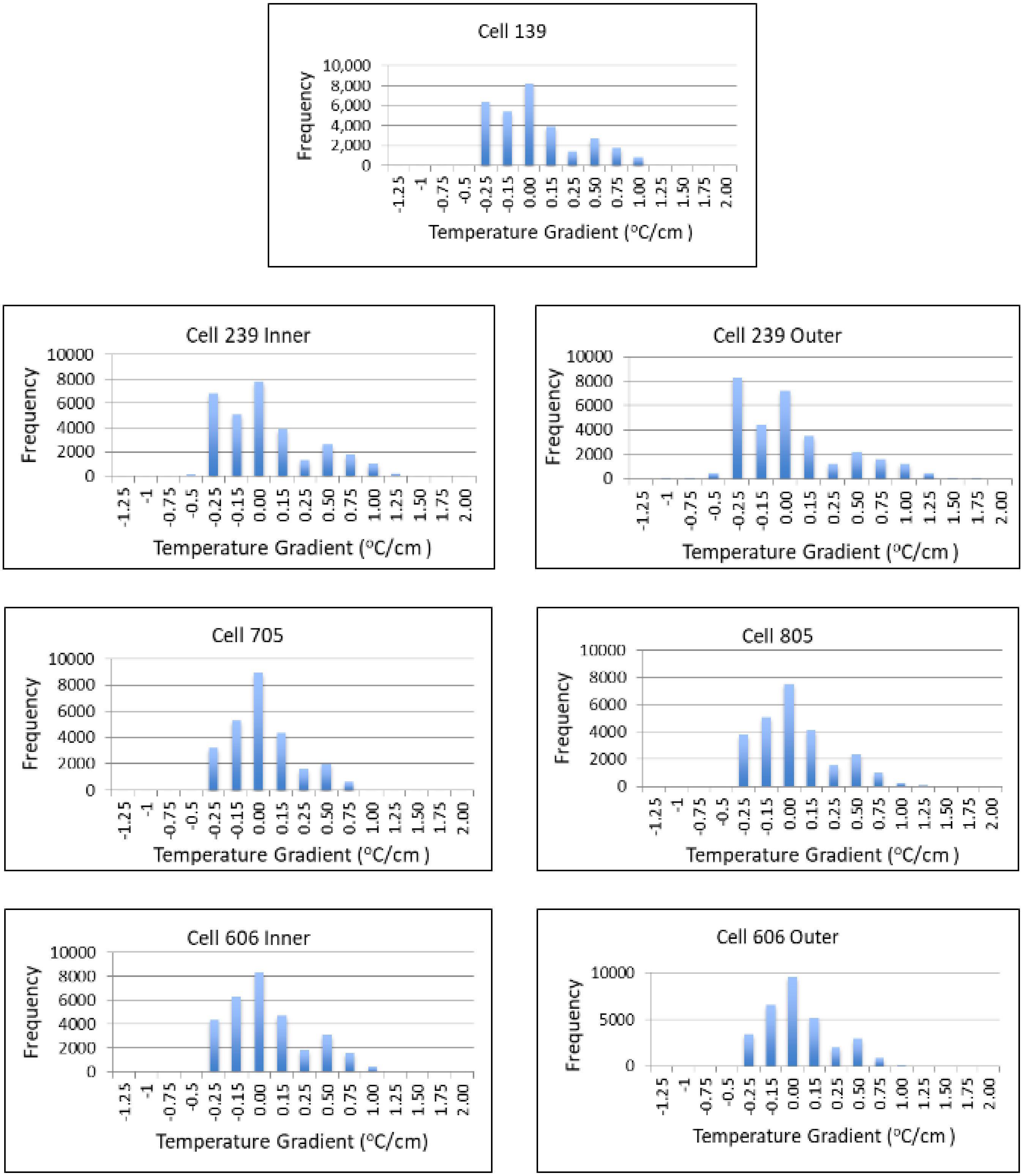

Figure 41. Frequency distributions of the linear temperature gradient for various cells.

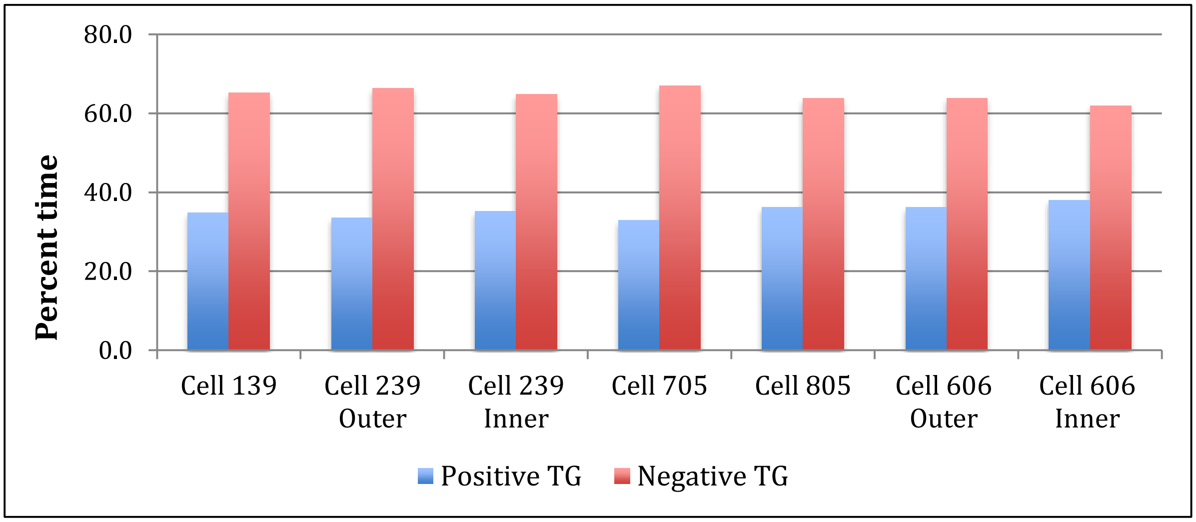

Figure 42. Percent times of positive and negative LTGs.

3.3 Environmental Strain

Vibrating wire sensors were installed in all of the MnDOT 2017 FRC research cells to measure the environmental strain that occurs in the slabs and to investigate the trends of this strain with respect to fiber dosage and pavement design features. A photograph of a vibrating sensor is shown in Figure 43. The raw data from this type of sensor are converted to estimate the environmental strain that is exerted on the concrete as a result of the change in the moisture state, temperature and temperature gradient, freezing of underlying layers, and joint locking. MnDOT has an established procedure for converting the raw vibrating wire data into a meaningful strain. One of the important steps in the vibrating wire data analysis procedure is to determine the initial strain value, which corresponds to the first reading when the concrete has hardened sufficiently to fully engage the sensor, and the temperature gradient between the nearby top and bottom temperature sensors is approximately 0. This serves as the initial or baseline value for subsequent readings. In order to determine the above-mentioned initial strain value, temperatures at the top and bottom of the slab and the raw frequency data are plotted together. An example of such plots is provided in Figure 44; these plots are related to one of the vibrating sensors of Cell 139 (Sensor 1, longitudinal direction). Using these plots, the time of the first 0 temperature gradient after the raw frequency data started proper cycling is determined; the corresponding strain at this time is considered as the initial strain value. In Figure 44, it can be seen that the initial strain value was achieved around 8:30 AM of July 18, 2017 (approximately 11 hours after the paving) when the temperature gradient was nearly 0.

In Cell 139, four vibrating wire sensors were installed, two each in the longitudinal direction and transverse directions, all at the bottom of the slab, at a depth of 2.5 inches (a half-inch from the bottom of the concrete). Figure 45 shows the environmental strains measured by the four sensors. Three out of four sensors showed a similar trend while the fourth sensor, which was in the transverse direction, shown a completely different and higher negative (tensile) strain compared to the other three. The less variation between the two sensors in the transverse direction and one longitudinal direction may be attributed to the small panel size and somewhat similar boundary conditions along three sides of each slab.

Figure 43. Photograph of a vibrating wire sensor.

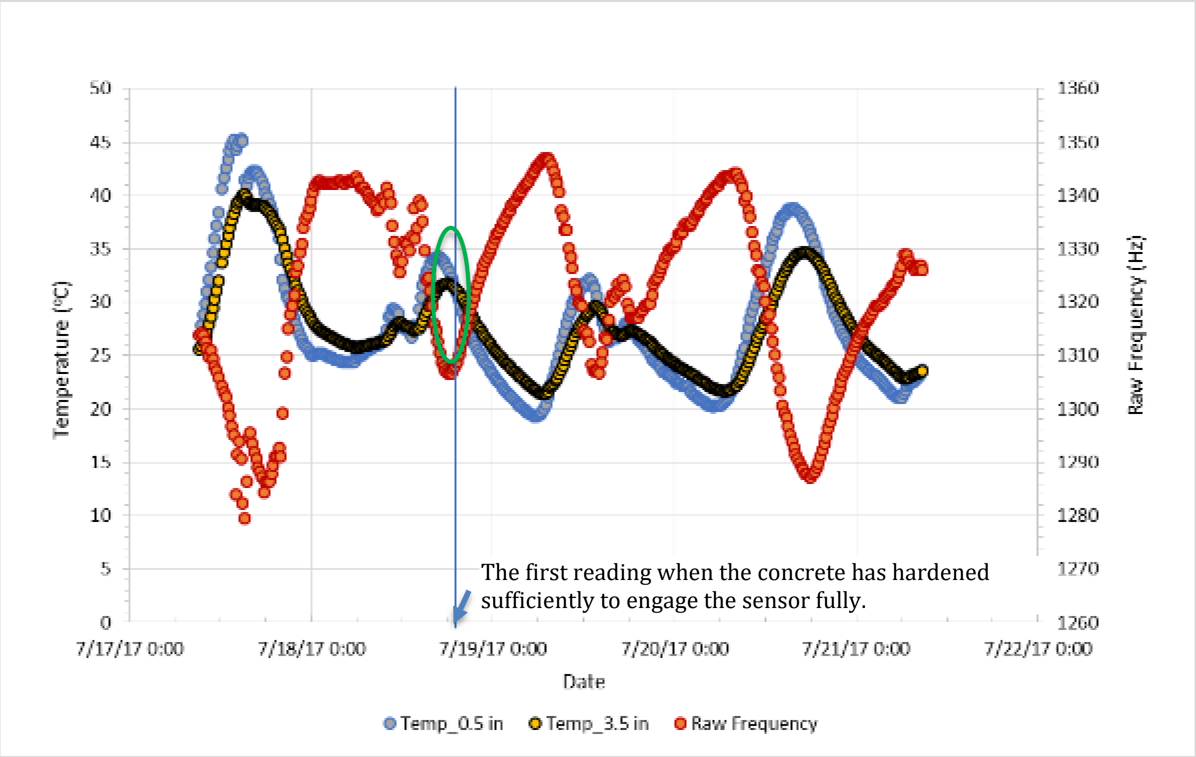

The first reading when the concrete has hardened sufficiently to engage the sensor fully.

Figure 44. Temperature vs raw frequency, Cell 139, Sensor 1.

Nevertheless, all the sensors have provided negative strains, indicating that slabs were in a state of contraction. A close look at all these plots indicates that the negative strains in all the sensors sharply increased from July 18, 2017, until the first week of August 2017. Although the temperature declined during this period, the drying shrinkage could have played an influencing role. After that, until the mid of April 2018, the strains in all the sensors followed the temperature variation with a couple of peaks during the winter when the temperature was among the lowest. Then from mid-April, 2017 when the temperature persistently raised, the strains surprisingly did not decrease but increased.

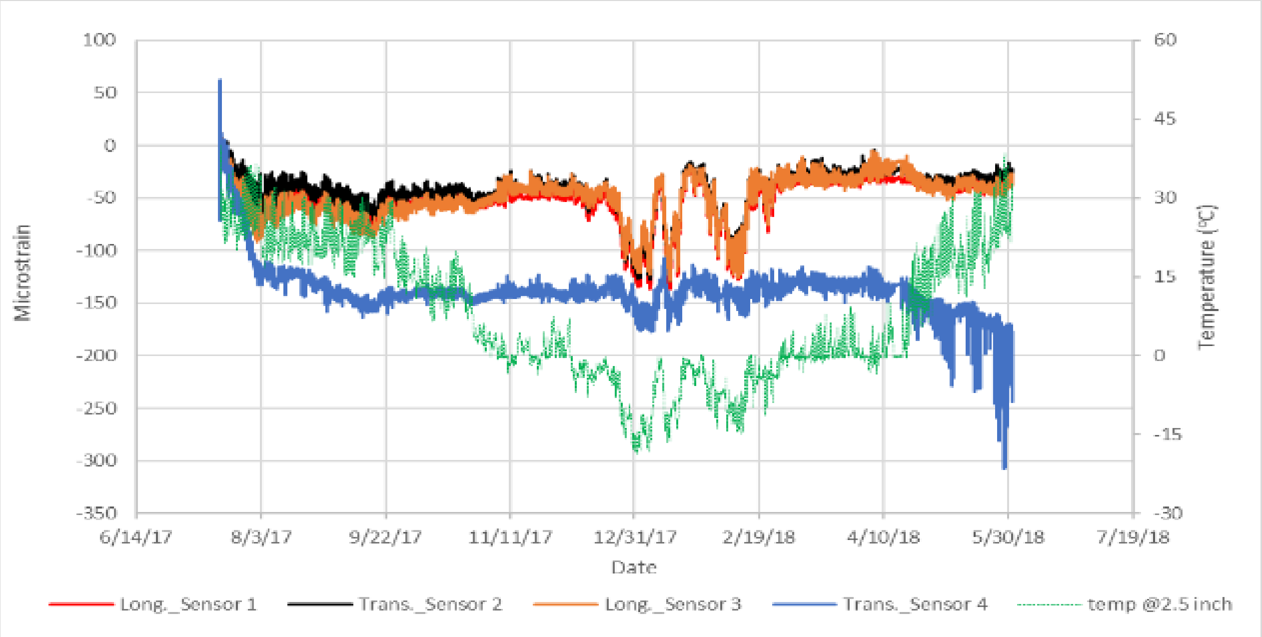

Figure 45. Environmental strains and slab temperature for Cell 139.

Figure 46 shows plots for the environmental strains and temperature at the 3.5-inch depth of the slab for Cell 239. Similar to Cell 139, vibrating wire sensors were installed only at the bottom of the slab because of the thickness limitation. As it can be seen in Figure 46, the strains varied with the seasonal temperature and also experienced a sharp increase in negative strain until the first week of August 2017 and then again between the mid-April and the end of May of 2018. This trend was similar to what was observed in the Sensor 4 of Cell 139. The overall variation of the strains recorded by the sensors in Cell 139 and 239 was similar, except the Sensor 6 in Cell 239, which was installed along the transverse direction. The strain in this sensor was relatively low compared to the other three sensors in Cell 239 until mid-April of 2018, which then sharply declines throughout May when the temperature was gradually rising. Compared to the sensors in the transverse directions, the sensors in the longitudinal direction, especially the Sensor 7, experienced greater strains and the maximum strains were recorded in the late May of 2018. The difference in magnitude of the environmental strains in both Cells 139 and 239 was not large, and a clear distinction could not be obtained because of the non-uniform behavior of a couple of sensors.

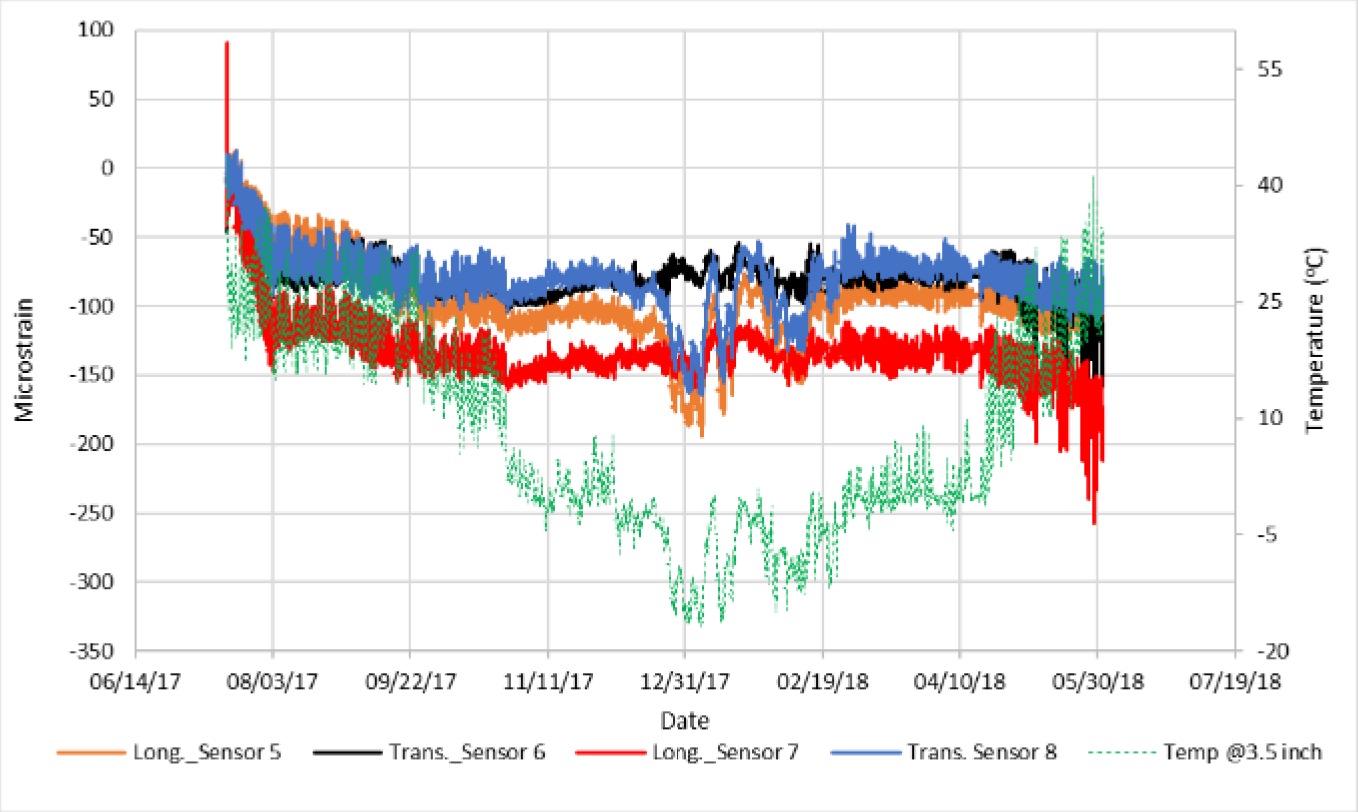

Figure 46. Environmental strains and slab temperature for Cell 239.

In Cell 705, vibrating wire sensors were installed in two slabs. In each slab, sensors were installed in the longitudinal and transverse directions. The longitudinal sensors were located at the center of the slab, and the transverse sensors were adjacent to the transverse joints as shown in Figure 24. Two sensors were installed at each location, one at the top and other at the bottom of the slab, one half-inch inside the concrete. A total of eight sensors were installed in Cell 705. Figure 47 and Figure 48 show the strains measured in the first slab and second slabs, respectively. Like the other two cells discussed above, the sensors in this cell also shown a great correlation with the seasonal temperature. In the first slab, it appeared that the sensors placed at the top of the slabs experienced more strains irrespective of their location with all the sensors recording higher negative strain values in the cold temperatures. The strains recorded by the sensors in the second slab also shown a quite similar pattern, except the Sensor 6 which was placed at the bottom of the slab along the longitudinal direction. This sensor recorded the largest strains out of all the eight sensors in Cell 705. The maximum strain, ~325 micro-strain, was recorded around the last week of December of 2017.

Similar to Cell 705, a total of eight vibrating wire sensors were also installed in Cell 805. All the sensors were installed at the center of the slabs, both near the top and bottom of the slab, a half-inch inside the concrete. This report included the results of three sensors installed in the first slab. The results of the three sensors in Cell 805 also showed a great correlation with the seasonal temperature variation; however, a clear distinction between the strains with respect to the direction of the sensors is not apparent. It could be anticipated that the smaller size of the slabs in Cell 805 would create less strain. However, the data until May 2018 did not show a clear distinction.

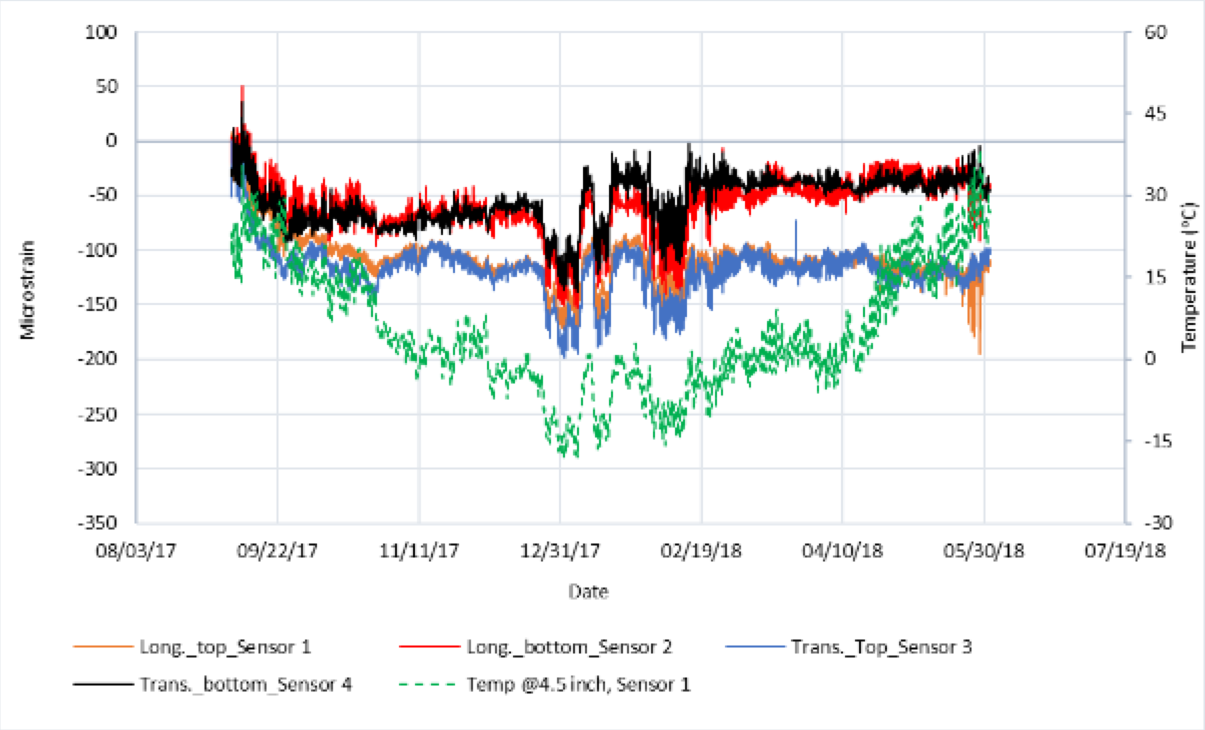

Figure 47. Environmental strains and slab temperature for Cell 705, first slab.

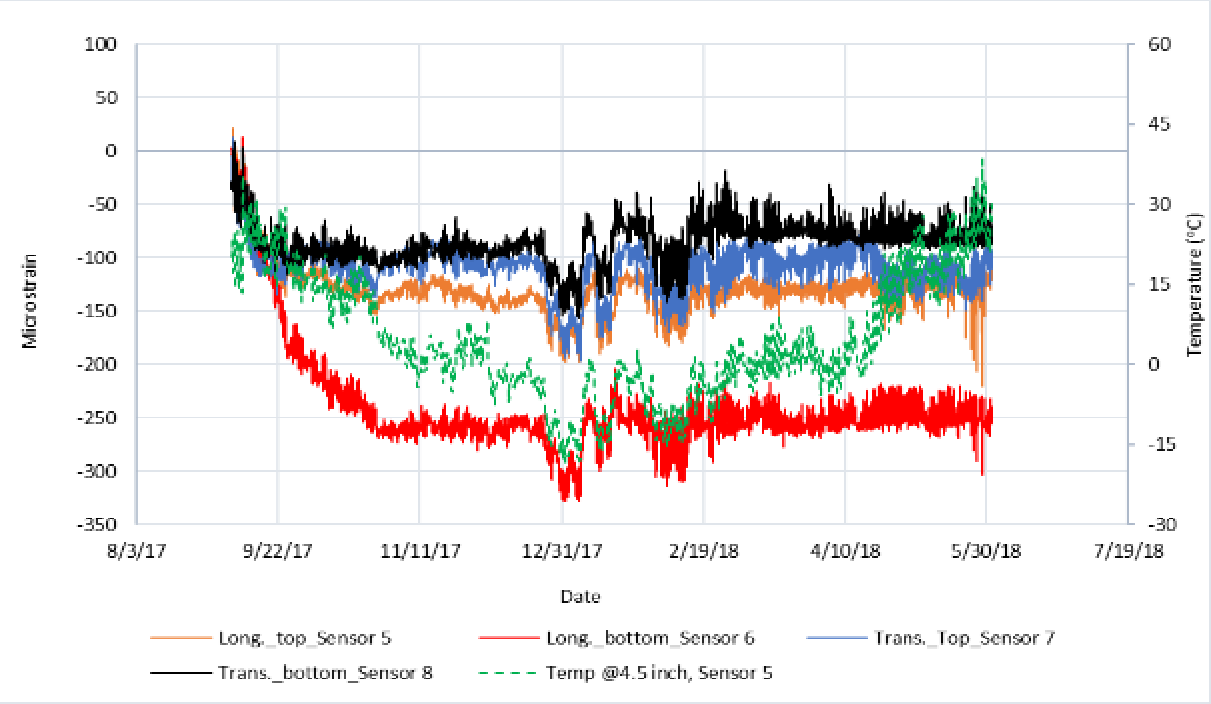

Figure 48. Environmental strains and slab temperature for Cell 705, second slab.

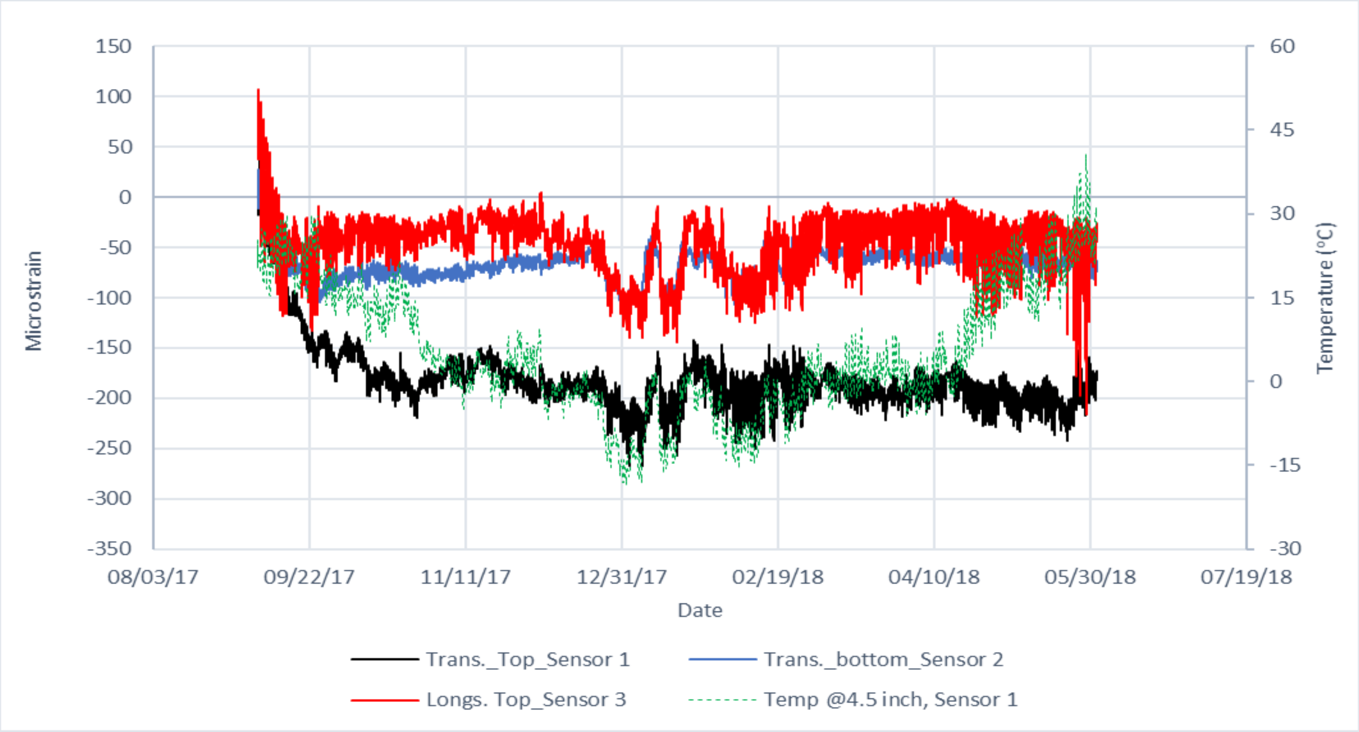

Figure 49. Environmental strains and slab temperature for Cell 805, first slab.

The analysis of the environmental sensors data for Cells 506 through 806could not be completed. Some vibrating wire data for the first couple weeks could not be found for these cells until the time of writing of this report. As previously mentioned, the vibrating wire and temperature data for the initial period are used to zero the subsequent strain values, the strains measured for these cells could not be computed. The research team and MnDOT are exploring different options to complete the analysis, such as using the initial trends of vibration data observed in other cells (e.g. Cell 239).

However, based on the findings from the presently completed analysis, it can be stated that the strain recorded by almost all of the sensors were influenced by the seasonal temperature. The difference in the strains between the sensors placed either in the transverse or longitudinal directions and the top and bottom of the slabs could not be clearly established from the data analyzed so far. It is anticipated that the inclusion of data for a larger period and from other cells will provide more insight into the environmental strains. The future analysis will also focus on establishing the relationship between strains and temperature and temperature gradients so that they could be used in future modeling.

3.4 Dynamic Strain

Dynamic strain sensors were installed in all of the MnROAD 2017 FRC research cells. These sensors record the dynamic strain in the slab when a vehicle, the MnDOT's five-axle truck, in this case, passes over them. As the tire offset (a distance of the wheel from the sensor) affect the readings, MnDOT's truck was run multiple times for each date of data collection. The raw data collected from the sensors are processed, and peaks, valleys, and baseline (Figure 50) are determined using the MnDOT's Peak-Pick Program (Burnham and Tewfik, 2007). Figure 50 is an example of the plots with the peaks and valleys noted. MnDOT has provided such plots for all the cells for different dates. These plots were used to determine the strain experienced by each sensor under each of the five axles loads. The maximum of all the strain values from of all the runs is reported as the dynamic strain in this report.

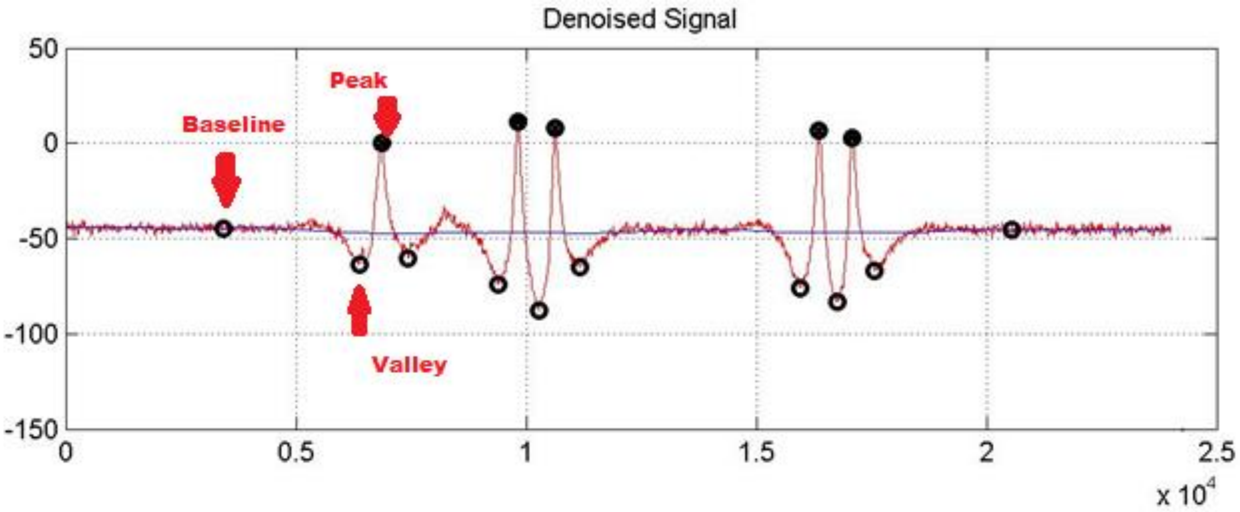

Figure 50. An example of a plot of strain due to the dynamic load exerted by the MnDOT truck.

Figure 51 shows the dynamic strains recorded by the sensors in longitudinal and transverse directions for Cells 139 and 239. The strains in both of these cells increased with time, but as anticipated, the magnitude of the strains in Cell 139 was higher than that was recorded in Cell 239. Strain in the transverse direction was slightly higher than that measured in the longitudinal direction for the Cell 139; the Cell 239 did not show a clear trend between the directions of the strains. Compared to the two other dates, it appears that the strains measured in Spring (during March 2018), when the subgrade and base layer are usually weak, were relatively high. Figure 52 shows the comparison of dynamic strains between Cells 705 and 805. Compared to Cells 139 and 239, Cells 705 and 805 experienced far lower strains. The strains in the Cell 705 were slightly higher than the Cell 805 from September 2017 through March 2018, then in April 2018, both the cells experienced similar strain values. As the magnitude of the measured strains was relatively low, the influence of the slab size on them is not apparent.

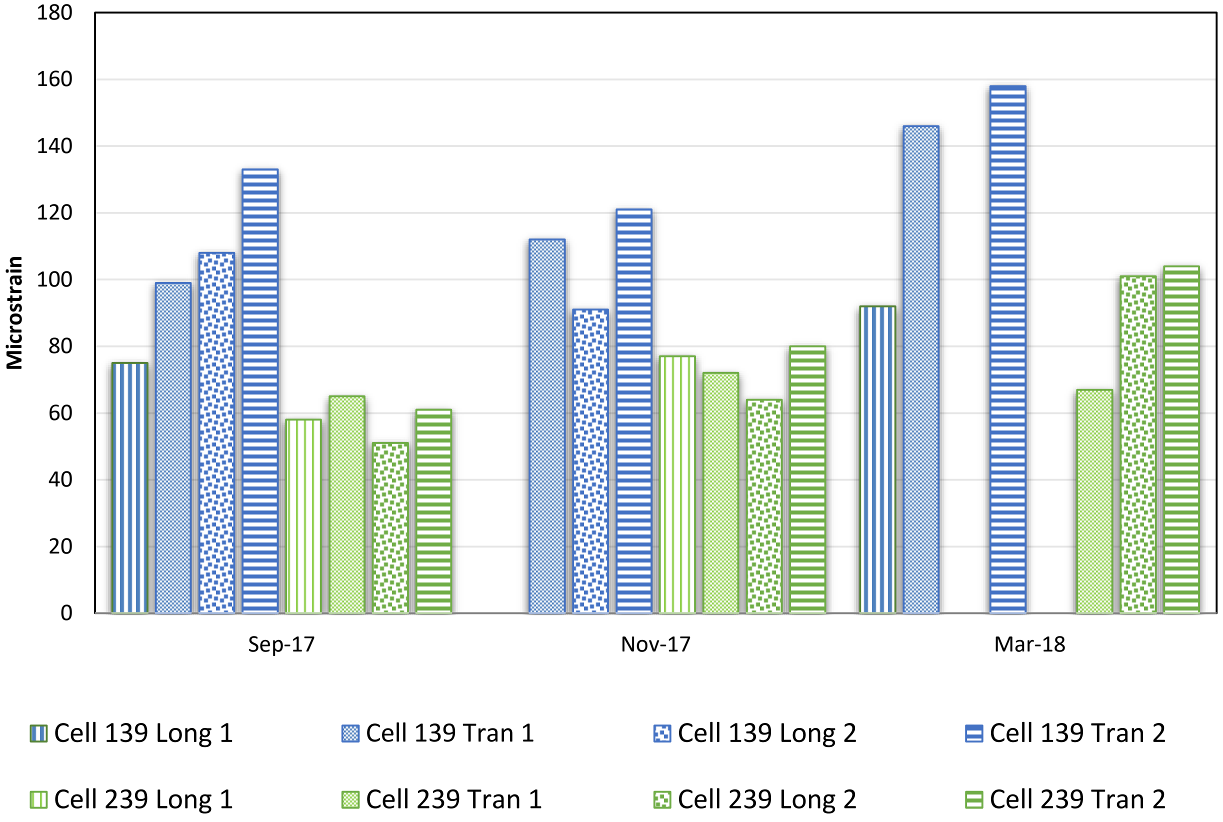

Figure 51. Dynamic strains recorded in Cells 139 and 239.

Cells 506, 606, 706, and 806 are the cells that compare the performance for different dosages of fibers. Dynamic sensors in these cells were laid along the transverse directions only. The magnitudes of the dynamic strains in these cells are comparable, except that the Cells 706 and 806 shown some higher strains in April 2018 when the base and subgrade support were possibly the weakest. Although these increased strains are somewhat surprising when compared to Cell 506, the higher thickness of the Cell 606 could be the reason for lower strains in that cell.

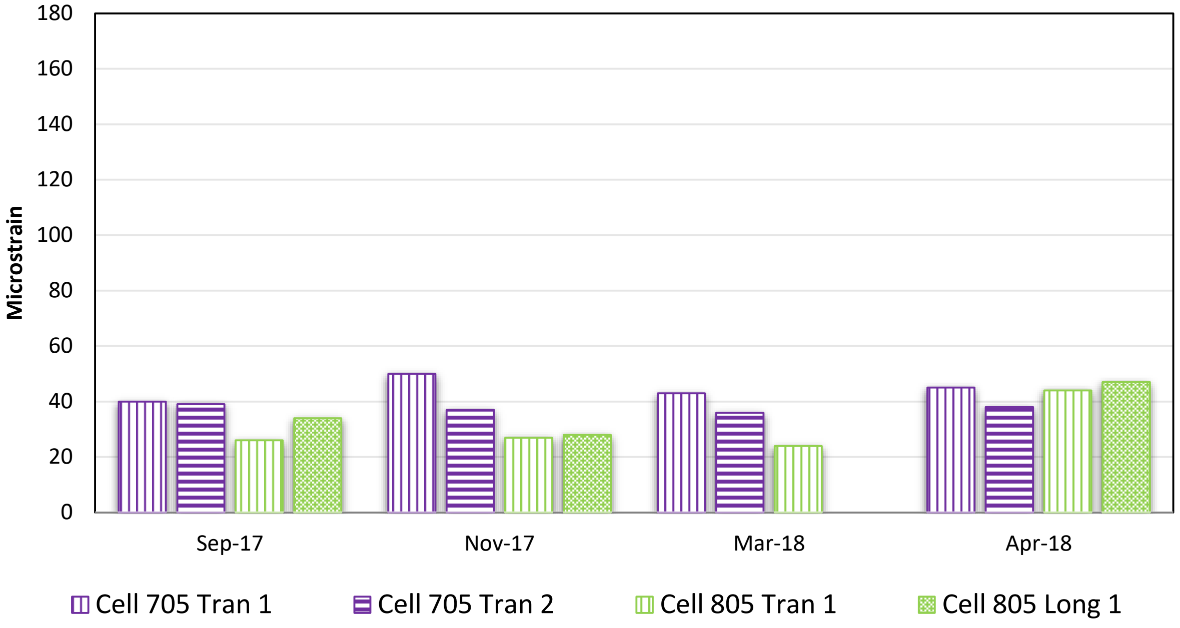

Figure 52. Dynamic strains recorded in Cells 705 and 805.

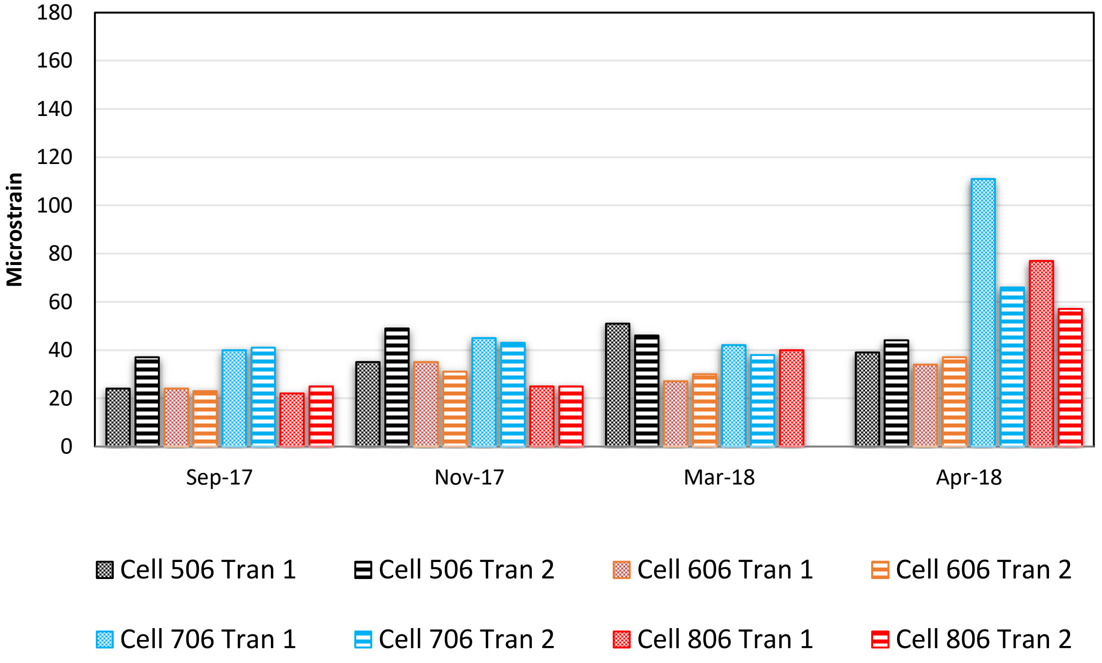

Figure 53. Dynamic strains recorded in Cells 506 through 806.

3.5 Joint Movement

3.5.1 Pin Measurements

In order to track the movements of the joints in different cells, pins (gage studs) were installed on either side of some selected transverse joints. Distances between the pins were measured shortly after installation, then periodically after that. These measurements can provide an idea of the seasonal joint movements. The dates that the pin measurement readings were recorded for each cell are provided in Table 9. Triplicate readings were taken for each pair of pins and then averaged to determine the distance between pins. Figure 54 shows the relative movement of some joints for Cell 239 with respect to the first reading collected in September 2017. At this point, a strong conclusion is not possible from a limited data set, but it appeared that the majority of the joints expanded with respect to what was observed in September 2017. Cell 139 was not included in the analysis because of the severe distresses observed in this cell. Regarding the other cells, measurements were collected only twice and because of this, the joint movements from pin measurements were not plotted at this time.

Table 9. Pin measurement dates.

Cell	139	239	506	606	706	806	705	805
Date	9/26/2017	9/26/2017	7/19/2017	7/19/2017	7/19/2017	7/19/2017	7/19/2017	7/19/2017
	2/14/2018	2/14/2018	5/22/2018	5/22/2018	5/22/2018	5/22/2018	5/22/2018	5/22/2018
	5/22/2018	5/22/2018						

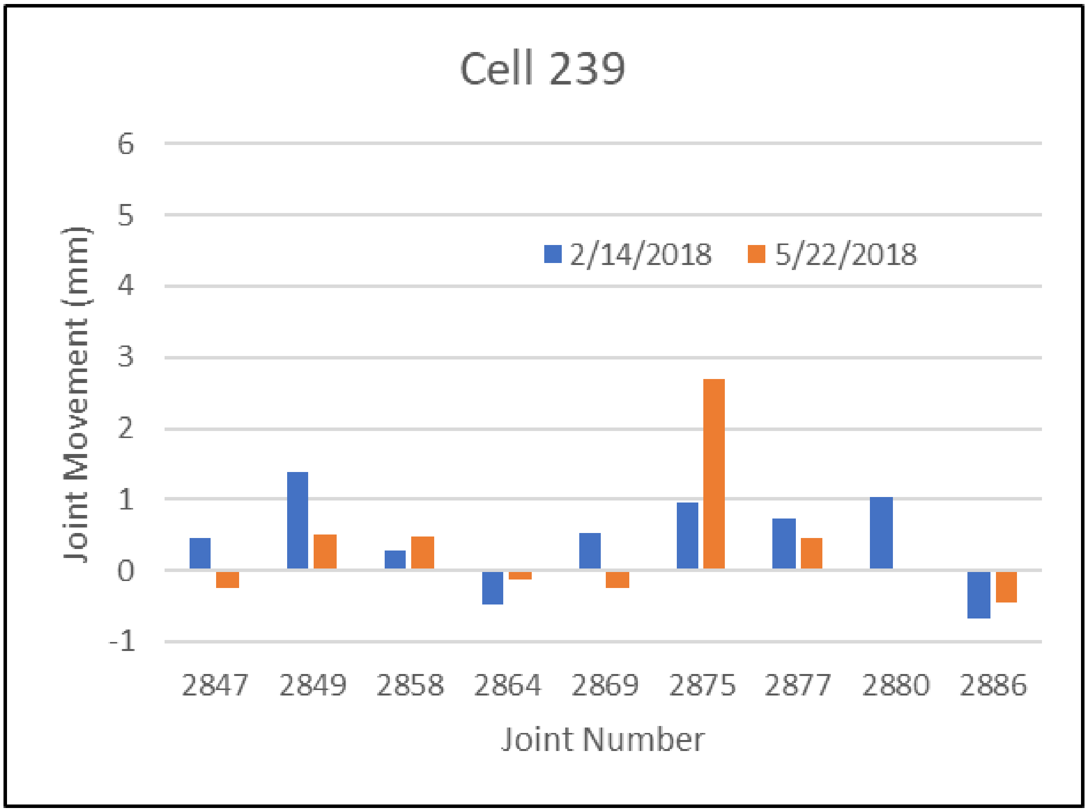

Figure 54. Joint movement of Cell 239 captured by using pin measurements.

3.6 Joint movement sensor data

A new type of joint opening sensor (spring-loaded potentiometer) was installed in MnROAD 2017 FRC research cells. A sketch and two photographs of such a joint opening sensor is provided in Figure 55. The goal of using this type of sensor is to track joint movement constantly throughout the year rather than manually measuring at certain time intervals. Figure 56 shows a plot of relative joint opening recorded by a joint opening sensor in Cell 506. The first reading was used to zero the subsequent joint opening readings. In this figure, it can be seen that there are two jumps in joint movement data, one in August of 2017 and the other one was in around October of 2017. The second jump is related to the reinstallation of the sensor.

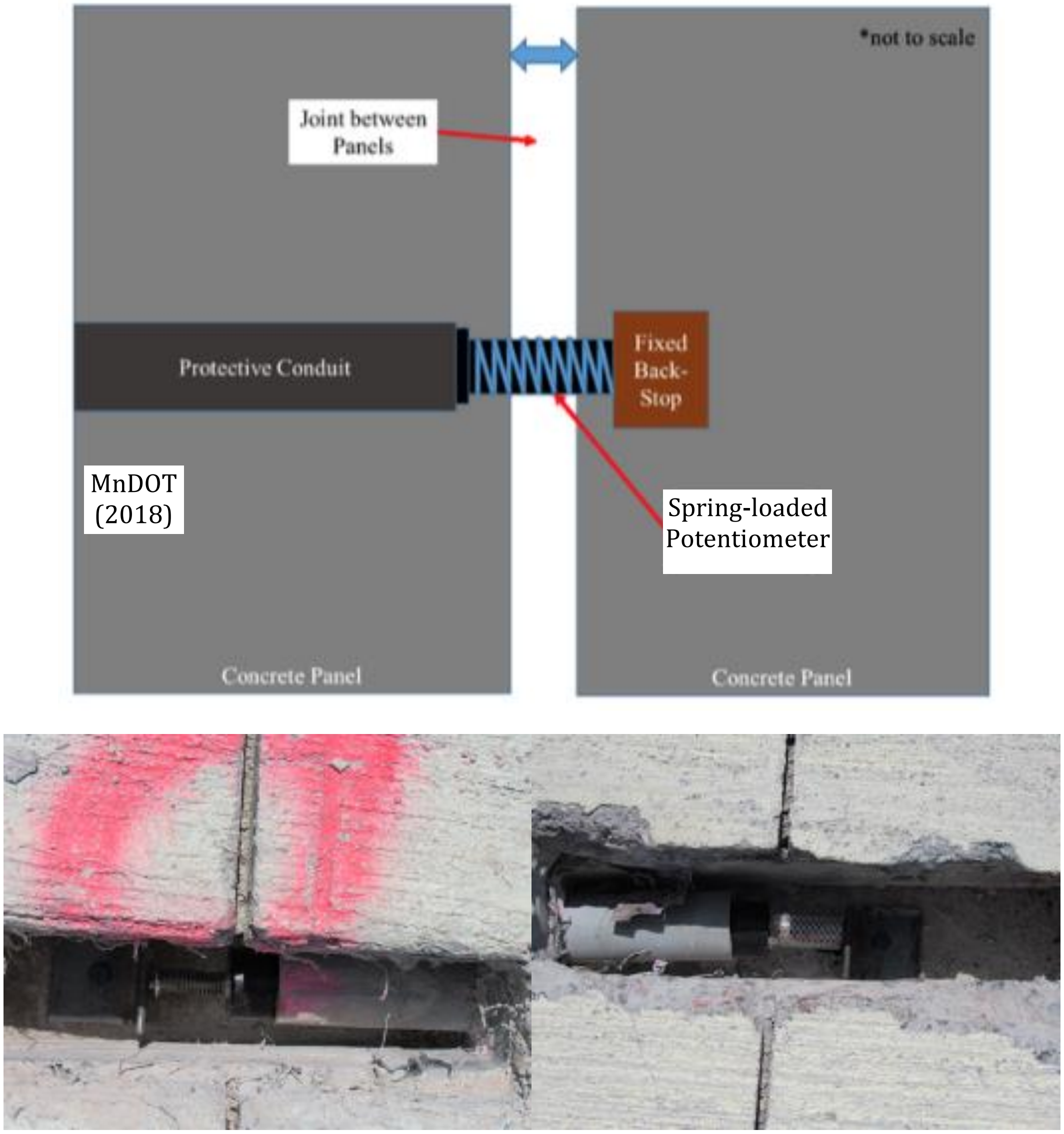

Figure 55. Sketch and photographs of joint opening sensors before installation of protective covering.

The majority of the joint opening sensors had to be re-installed after their first installation; protection for the sensor was applied during the reinstallation time. For the sensors that were reinstalled, data were adjusted to neutralize the re-installation related jump, as shown in Figure 57. Note that the y-axis scales used in this figure and the following figure are different than the one used in Figure 56. The first jump in Figure 56 is assumed to be related to the joint deployment. When the joints deploy, the sensor readings are supposed to show a jump. Some sensors didn't record any jump. The reason for this is either the deployment occurred before collecting the initial reading, the jump was not recognizable because of a minimal crack width change, or joint did not deploy at all. Figure 58 provides an example of joint movement readings collected by Sensor 3 of Cell 706; in this case, the joint in question probably did already deploy before the collection of the first reading. This plot provides a good example of relative joint opening with respect to the first reading. It can be seen that the joint opening was maximum during the winter months, after which the joint opening reduced with the temperature increase.

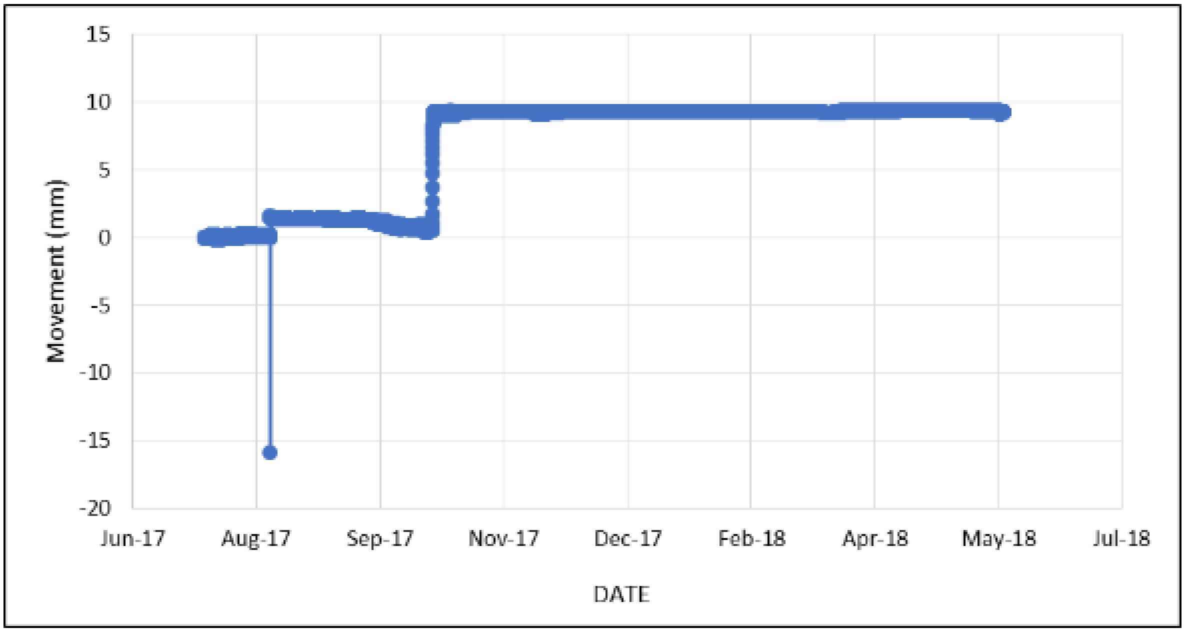

Figure 56. Joint movement recorded by Sensor 1 of Cell 506, before adjustment for re-installation was made.

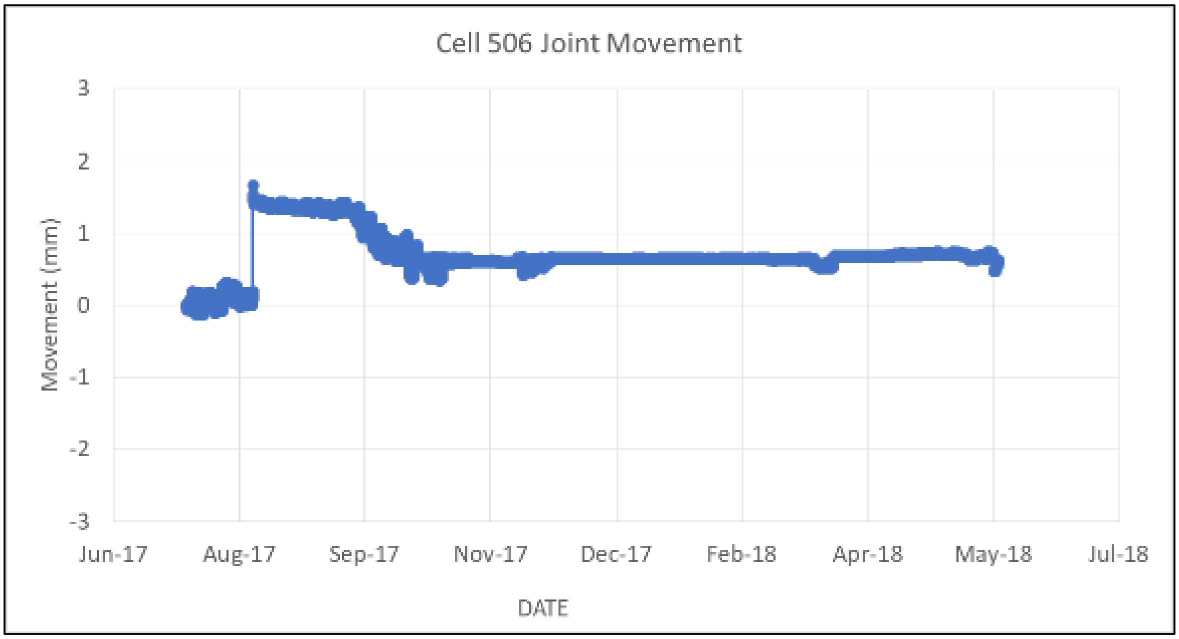

Figure 57. Joint movement recorded by Sensor 1 of Cell 506, after adjustment for re-installation was made. (***Note- diff. scale in y-axis)***

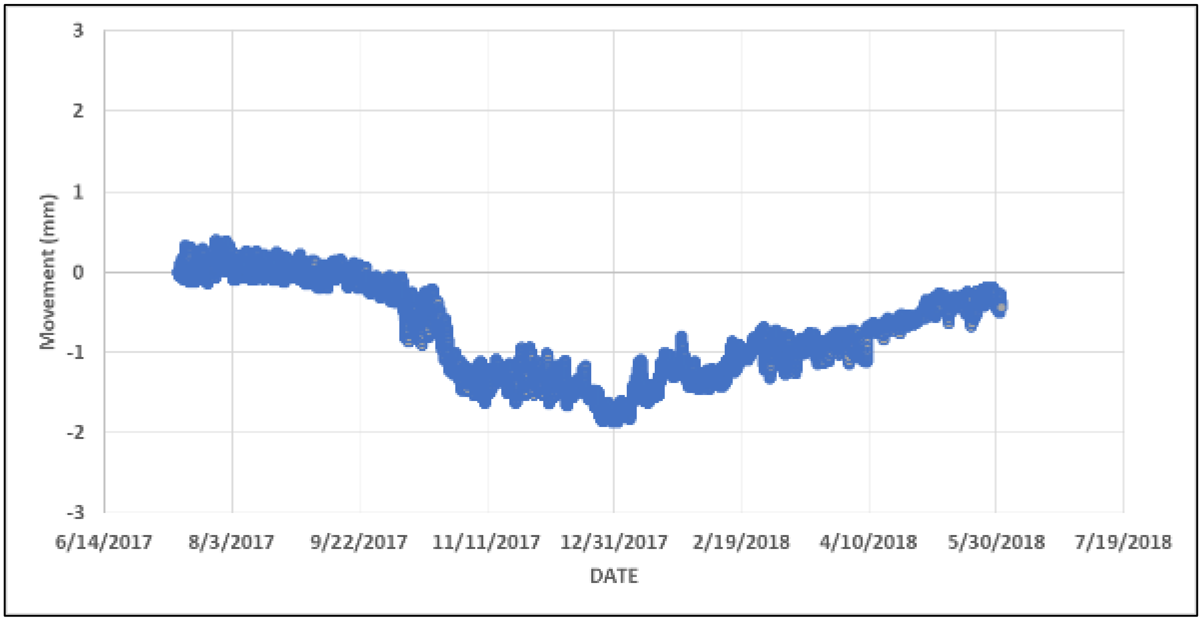

Figure 58. Movement recorded by Sensor 3 of Cell 706, no adjustment was required. (***Note diff. scale in y-axis)***

Some sensor readings were discarded because of erroneous data, such as in Figure 59, where the crack opening readings fluctuated significantly. Figure 60 shows joint movement data recorded by Sensor 1 of Cell 139; this was also excluded due to inconsistency in readings possibly due to the deterioration of the slab or sensor damage. Some sensors in other cells were excluded for similar reasons, such as in Cells 705 and 805. Appendix B includes joint movement plots for all the cells and Table 10 provides a summary of the approximate maximum joint movement observed for each of the cells. Because of the considerable variations in the data quality in some sensors, very convincing trends could not be achieved for all the cells, but the results of many sensors are reasonable. In summary, the sensors in Cell 506 has recorded the minimum joint movement and Cells 705 and 805 likely experienced the largest joint movements. However, the data available at this point does not provide a great trend on the contribution of fibers.

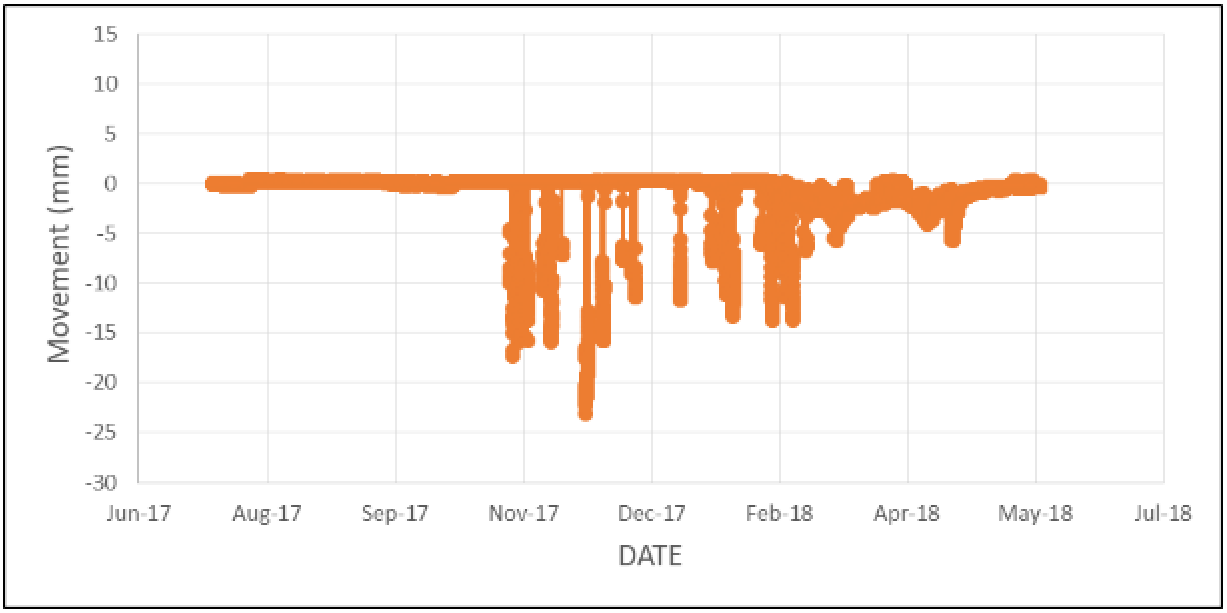

Figure 59. Movement recorded by sesnor 2 of Cell 506 ***(Note diff. scale in y-axis).***

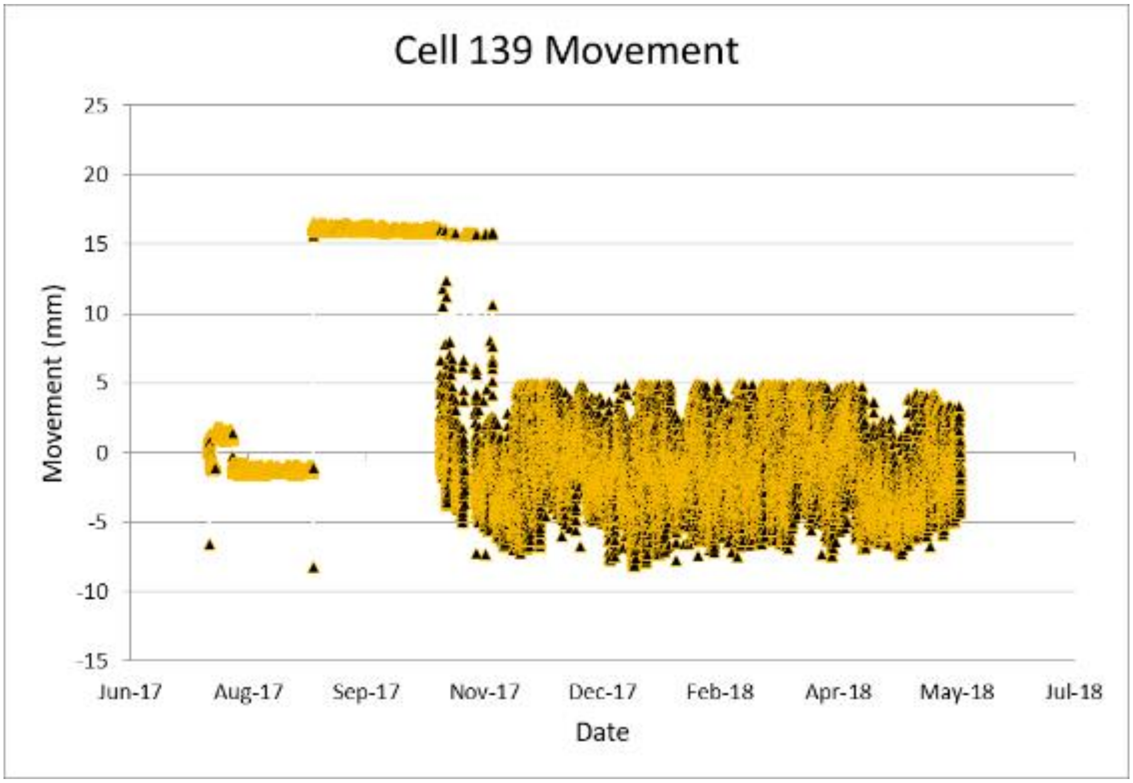

Figure 60. Movement recorded by Sensor 3 of Cell 139. (***Note diff. scale in y-axis).***

Table 10. Approximate maximum joint movement for different cells.

	Max opening (approx.), mm
Cell 139	6
Cell 239	Not clear
Cell 705	10
Cell 805	10
Cell 506	1.5
Cell 606	9
Cell 706	2
Cell 806	2

In order to investigate the seasonal variation of joint opening, the monthly average relative joint opening was calculated for each cell and plotted in Figure 61 and Figure 62. The averages for Cells 705 and 805 were zeroed with respect to September 2017, and all the other cells were zeroed with respect to July 2017. Cells 705 and 805 were zeroed using the later month because they were constructed later than the other cells. Note that the Y-axis scale of the plots for Cells 705 and 805 are different than the scale used for Cells 139 and

239 in Figure 61. In Cell 139, two sensors did not show a great variation in the joint opening, but the Sensor 1 rightly showed that the joint opening increased by a magnitude of 6 mm during the winter months compared to the first reading taken in July 2017. Based on the data, the joints of the Cell 239 (at least where the sensors were installed) remained relatively dormant for most of the year with slight expansion recorded by Sensors 3 and 4 in the winter months. Cells 705 and 805 had experienced the largest joint opening movement among all the eight cells. While a few sensors installed in these two cells remained dormant, others showed great movements. The long slabs (12 feet long) of these cells experienced around 10 mm relative joint movement with respect to the September joint opening. However, it shall also be noted that such large joint movements have not been visually observed in the site; therefore, a follow-up investigation is in progress to study the sensors closely to determine the cause of such high values of the joint movement. At this point, it can be stated that it is possible that some sensor data are erroneous.

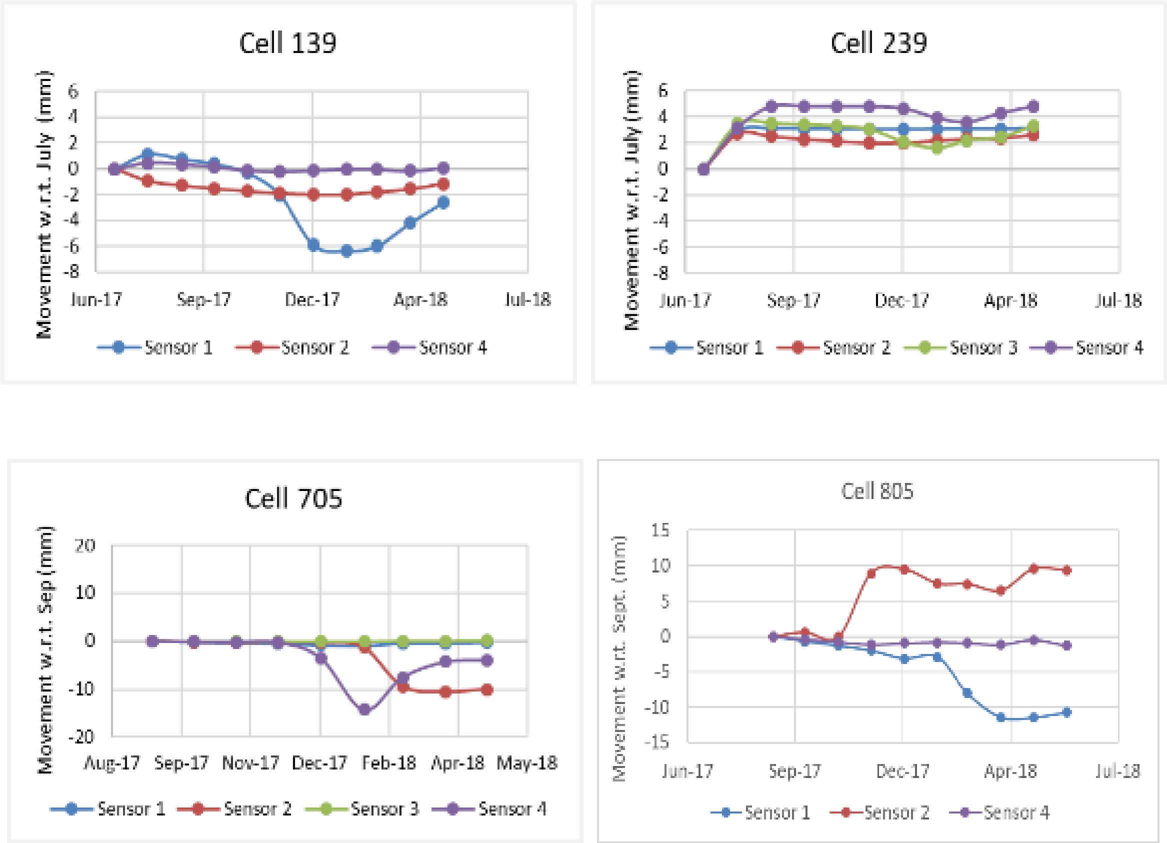

Figure 61. Monthly average relative joint movement for Cells 139, 239, 705 and 805.

For Cells 506 through 806, there is a concern in the accuracy of the sensors in Cell 506. This cell does not contain fibers, and it was anticipated that larger joint openings would be observed in this cell compared to its counterparts (Cells 606 to 806). Cell 606 which contained 5lb/ cy fibers, did experience as much as 5 to 10 mm joint opening during the winter months. Comparing with Cells 606 and 706, Cell 806 showed less joint openings. The higher fiber dosages in Cell 806 may hold the joints together tighter, potentially indicating a contribution of the fibers towards decreasing the crack width.

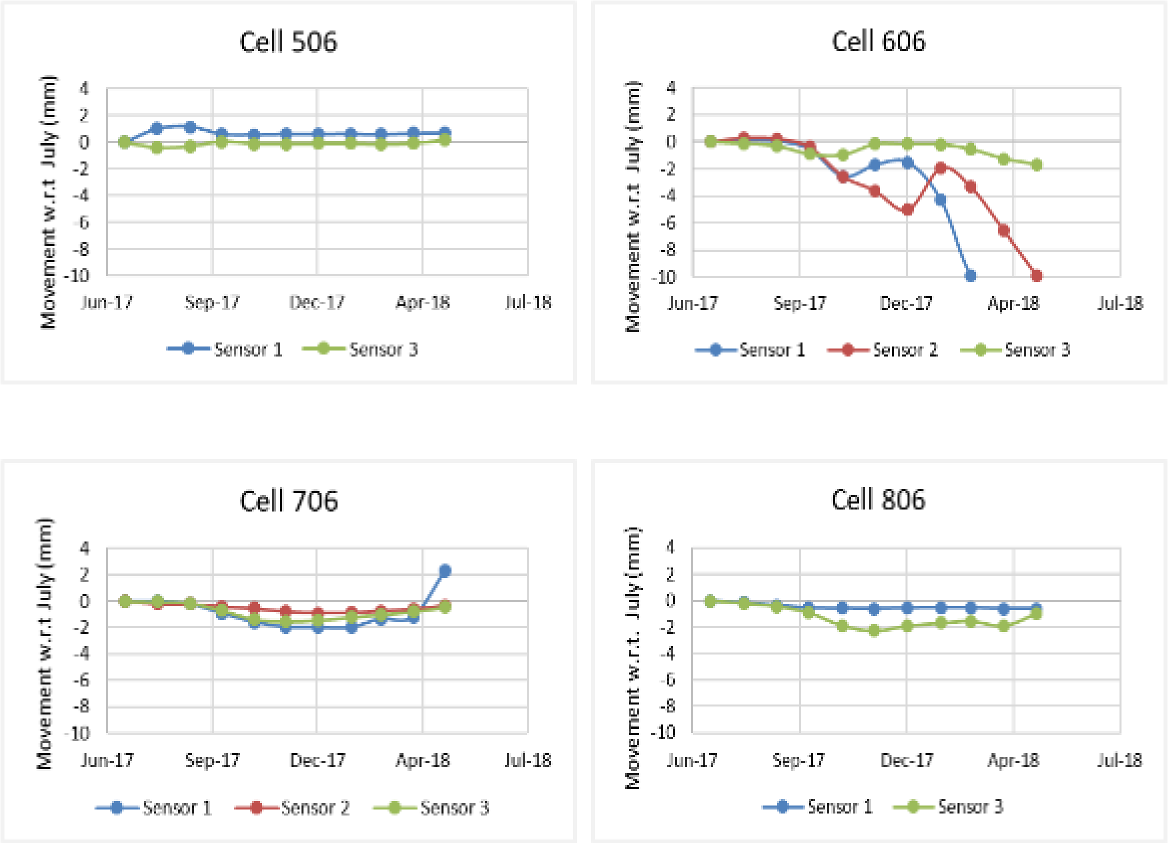

Figure 62. Monthly average relative joint movement for Cells 506 through 806.

4 JOINT PERFORMANCE

This section discusses the joint performance data. The results of the falling weight deflectometer (FWD) test conducted at selected transverse joints were used to determine the load transfer efficiency (LTE), differential displacement, and loaded-side displacement. The LTE is the ratio of the deflections at the unloaded side to the loaded side and expressed as a percentage. The differential displacement is the arithmetic difference between the loaded-side deflection and unloaded-side deflection.

4.1 LTE

Figure 63 shows the LTE of Cells 139, 239, 705 and 805. The LTE data of the Cells 139 and 239 were comparable when the first test was conducted on September 6, 2017and it ranged between 85 and 94%. The LTE of these two cells then continued to drop until the third testing was conducted on March 27, 2018. The LTE results of May 3, 2018, showed that the LTE started picking up as the temperature was increasing and the joints were closing in. Among all the lanes in these two cells, the inside lane (loaded by MnROAD truck) of Cell 239 showed the lowest LTE when measured in the winter and spring of 2018. Although the faulting results for this cell was not concerning, it will be interesting to see how this cell performs in the near future in terms of faulting.

The wide joint opening of Cells 705 and 805, as discussed in Section 3.6, appeared to have influenced the LTE significantly. Contrary to the low faulting results, these two cells exhibited surprisingly very low LTE, at least in the joints considered in FWD testing. The wide joint openings of these cells explain the reason for significantly low LTE. Based on the joint opening sensor data, some of the cracks could be as wide as 10mm. The LTE of concrete pavement at such wide joint opening is usually very low.

The LTE results of Cells 506 through 806, shown in Figure 64, clearly reveals the contribution of structural fibers in keeping the LTE high. For Cell 506, even though the FWD test conducted on the driving lane in September 2017 showed a range of LTEs between 75 and 85%, with time the LTE had significantly decreased. Even though the LTE had slightly picked in the summer of 2018, it remained around 40%. The LTE in the passing lane of Cell 506 was always low, with a maximum of around 50%.

The LTE results of Cell 606, which is 6-inch thick, were at or above 90% when measured in September 2017, except one joint in the passing lane which always did show a low LTE (around 25 to 50%). Out of six joints tested in Cell 606, three joints were still performing well with around 90% LTE, when measured last time in June 2018. LTE in the other three joints lies between 30 and 50%.

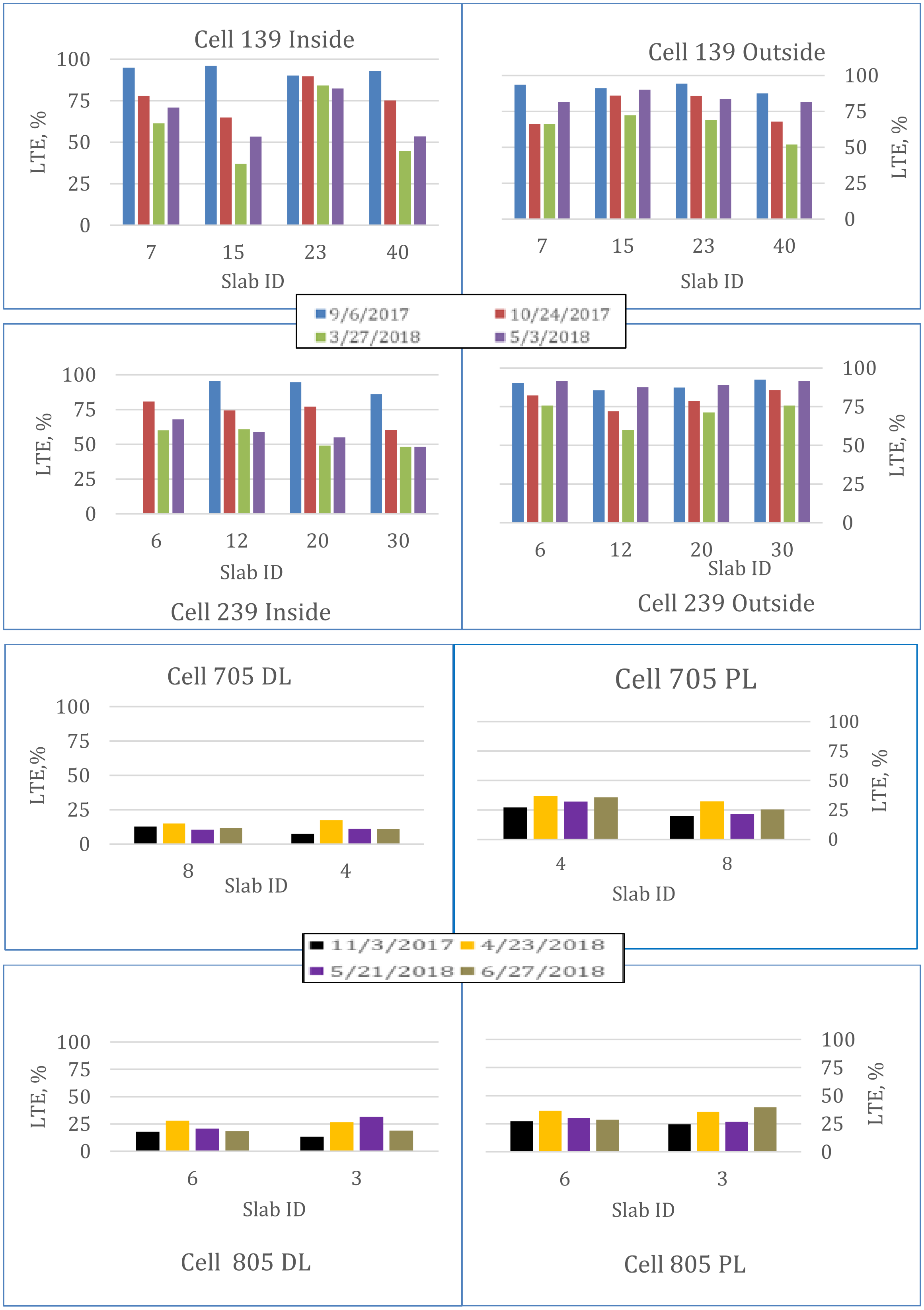

Figure 63. LTE of Cells 139, 239, 705 and 805.

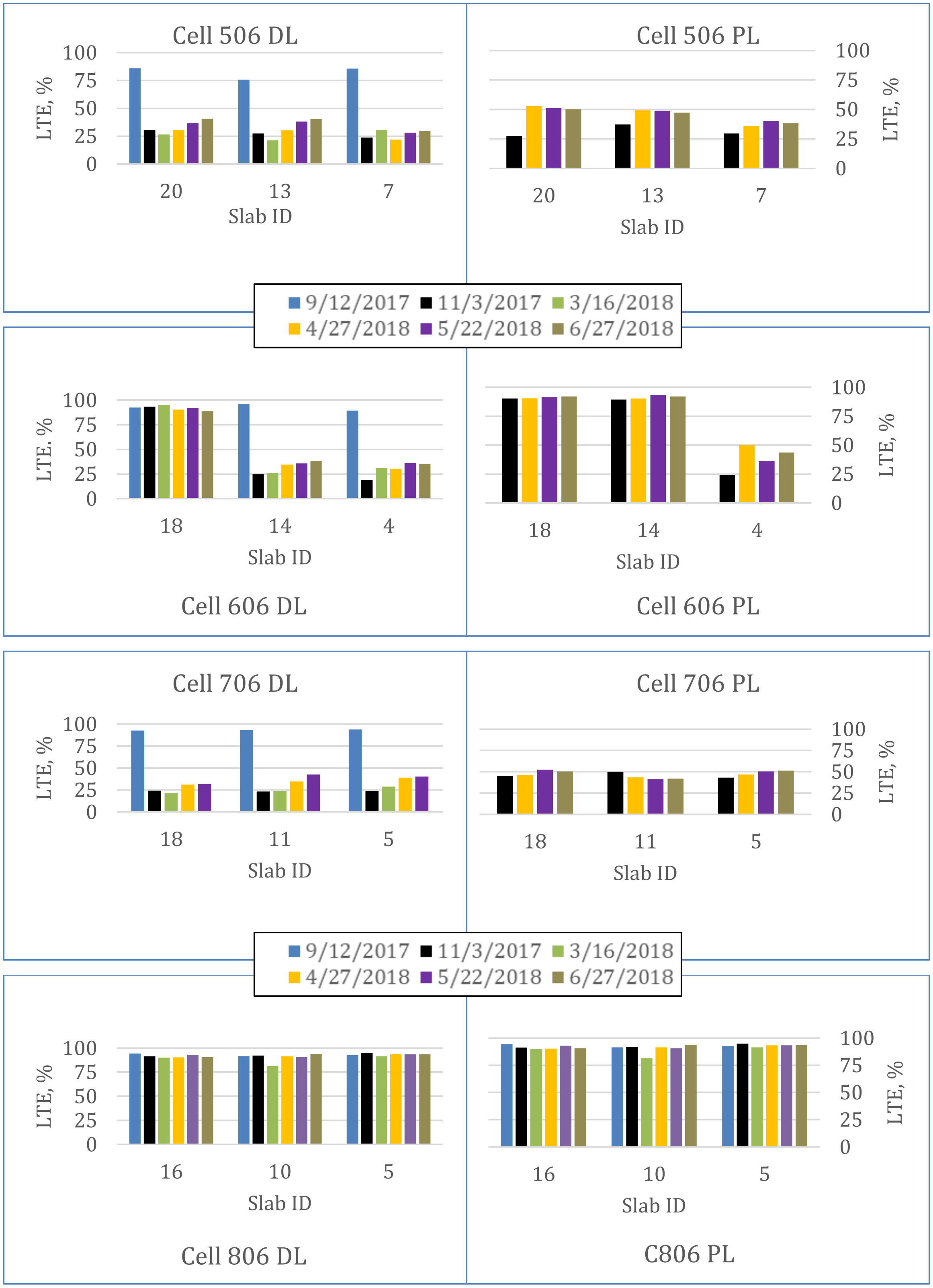

Figure 64. LTE of Cells 506, 606, 706 and 806.

The LTE of Cell 706, which is 5-inch thick, was initially high at three joints (at the driving lane) out of total of six joints measured. However, when measured in June 2018, these joints exhibited 40 to 50% LTE. This cell still did not show large faulting; however, the low LTE may create potential faulting in the near future.

Cell 806, which is 5-inch thick and contains 11.7 lb/cy of fibers, consistently exhibited the highest LTE among all the cells. Notably, all the joints were able to maintain a very good LTE as high as 94% throughout the first year service life. The higher LTE of this cell definitely helped in keeping the faulting to the lowest among all the eight cells. The performance of this cell assures that structural fiber could increase the LTE and decrease the faulting when a proper dosage is adopted.

4.2 Differential Displacement

Figure 65 and Figure 66 shows the plots for differential displacements for all the cells. The general trend of the differential displacement is similar to the trends observed for the LTE. Similar to the LTE results, this result also indicates that the inner lane of Cell 239 may be a concern in the near future, the higher differential displacement may abrade the crack faces more which can then result in joint deterioration.

Cells 705 and 805 both have experienced high differential displacements at the transverse joints; the differential displacements of Cell 705 (~1000 micron) was almost twice of the Cell 805 (~460 microns). Even though the differential displacements was relatively high, the fabric interlayer provided in these cells is expected to limit the faulting. However, FWD data and faulting measurements in some additional joints may provide a better understanding about the real cause of these high differential displacements, and whether any other joints also have the similar high differential displacements or not. The contribution of fibers in joint performance can also be seen in the differential displacement plots for Cell 506 through 806. Cells 506 and 606 exhibited more differential displacements than the Cells 706 and 806, with negligible values for the Cell 806. The joint faces in the slabs of Cell 806 will abrade minimally, which will yield a better aggregate interlocking and may provide service for a longer period.

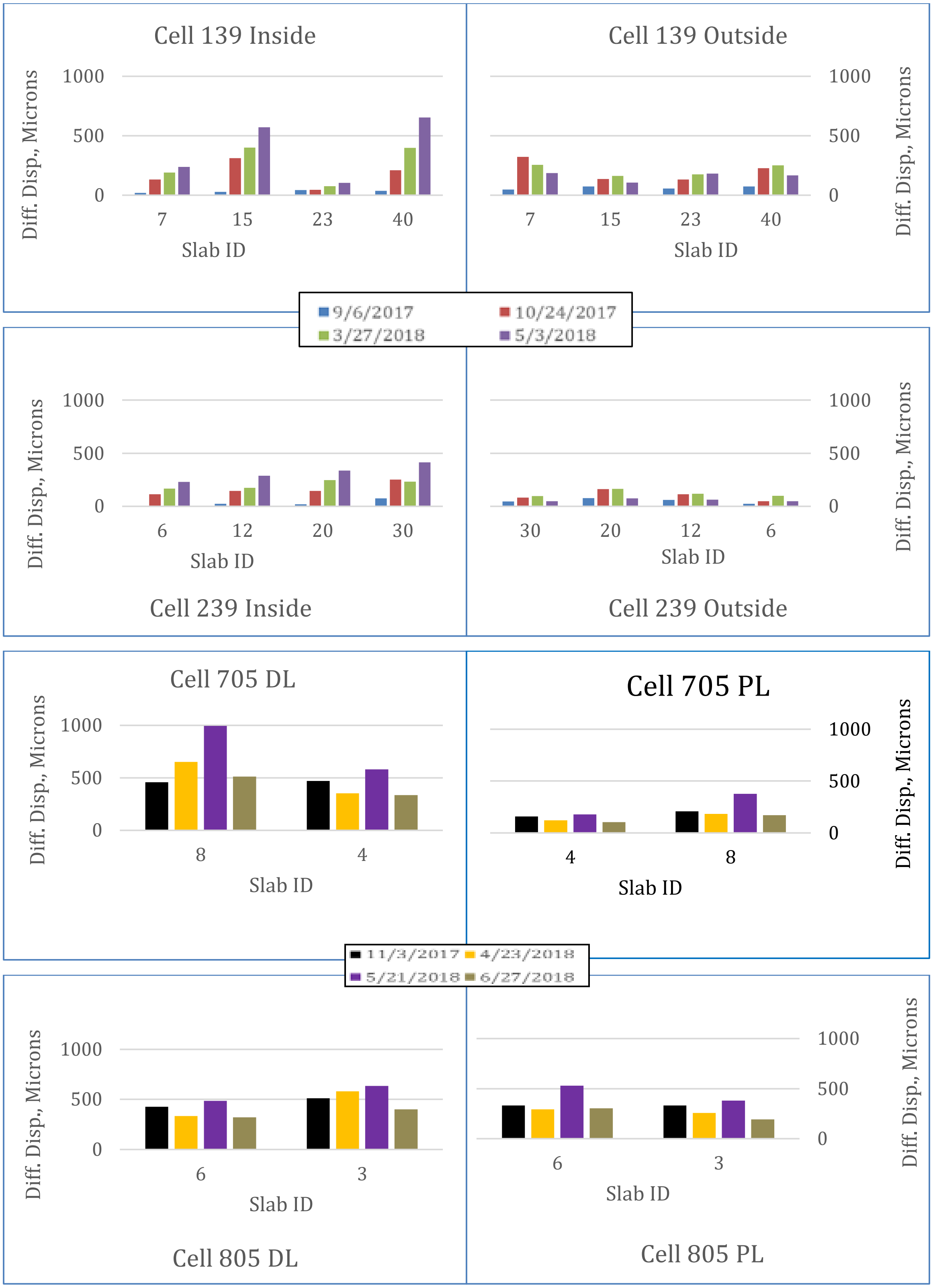

Figure 65**.** Differential displacement of Cells 139, 239, 705 and 805.

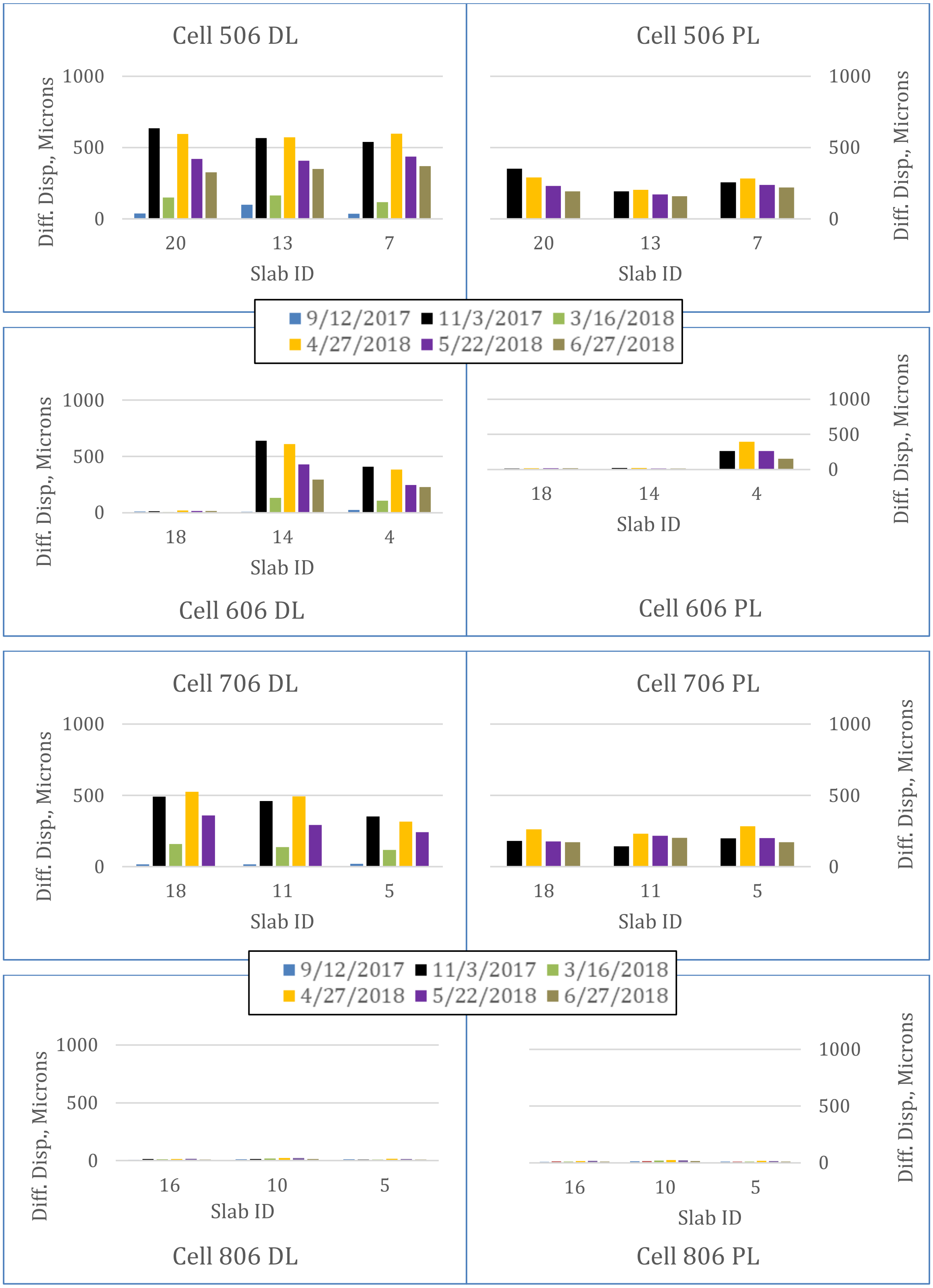

Figure 66**.** Differential displacement of Cells 506, 606, 706 and 806.

4.3 Loaded-side displacement

Loaded-side displacement is a good indicator of joint performance. Even though the LTEs and differential displacements for the Cells 139 and 239 were somewhat comparable, especially the outside lanes, the Cell 139 had significantly higher loaded-side displacement, as shown in Figure 67. This clearly indicates that cell 139 had poorer joint stiffness or weaker support compared to Cell 239.

Similar to LTEs and differential displacements, the loaded-side displacements for the Cells 705 and 805 are a concern. Between these two cells, the Cell 705 had experienced higher, and as much as twice, the loaded-side displacements compared to Cell 805.

The loaded-side displacement of Cells 506 through 806 also showed that the 806 is performing better than the other three cells.

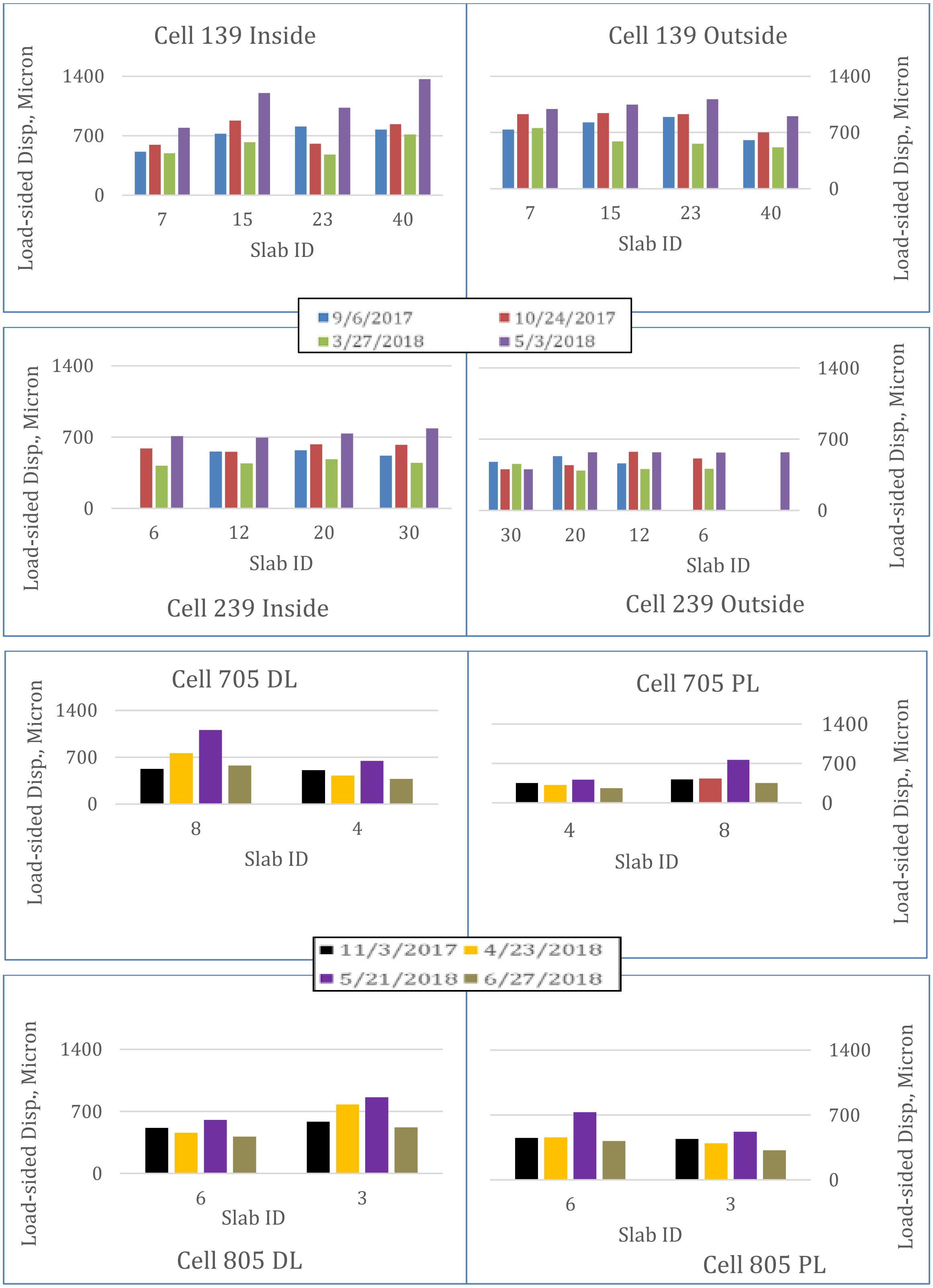

Figure 67**.** Load-sided Displacement of Cells 139, 239, 705 and 805.

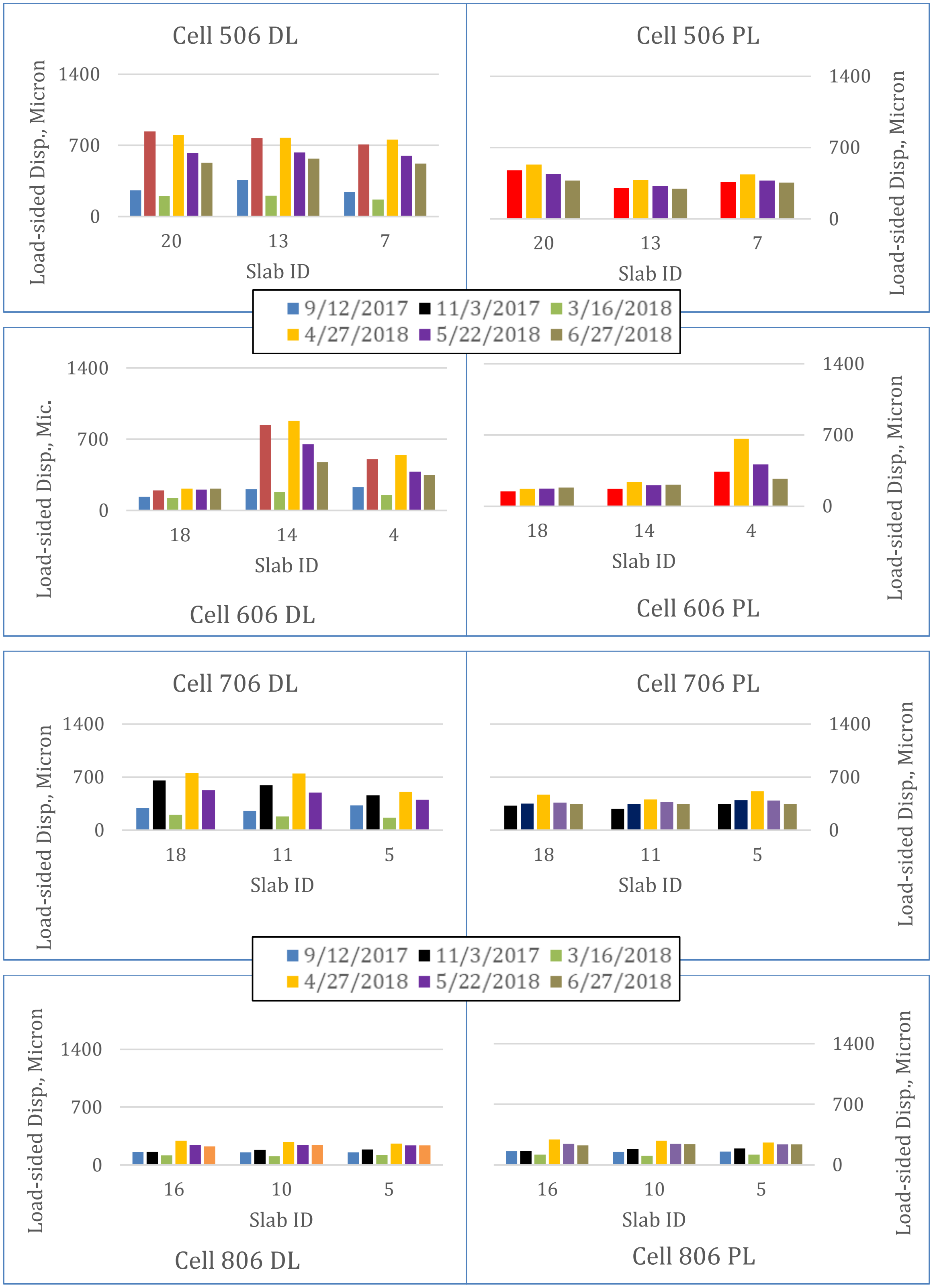

Figure 68. Load-sided Displacement of Cells 506, 606, 706 and 806.

5 CONCLUSIONS

While several fiber reinforced concrete pavements or overlays had been constructed in the United States and many other countries, a comparison between the performance of fiber reinforced concrete pavements or overlays and their plain concrete counterparts could not be found because of lack of companion sections. The National Road Research Alliance funded and MnDOT constructed 2017 FRC research cells definitely provide a great opportunity for drawing such a comparison and quantifying the contribution of structural fibers in mitigating cracks, faulting and other distresses.

This report first presented a summary of the distresses observed in different cells during the first year of service, from July 2017 to May 2018. The report then provided a discussion on the different sensor data collected during this period. The results of the joint performance tests conducted by using the falling weight deflectometer were discussed at the end of this report. The following major conclusions can be drawn from this report.

The performance of Cell 139, which is a 3-inch thick ultra-thin concrete pavement on an unstabilized gravel base, indicated that fibers (at the dosages used in this experiment)

1) might not be helpful in such thin concrete pavements, especially when the base is relatively weak.
2) The difference in the performance of Cell 506 with others indicates that fibers could reduce joint spalling.
3) Corners cracks were the most common cracks found in the various test cells, followed by the transverse and longitudinal cracks.
4) Comparison between Cells 506 through 806 revealed that fibers could decrease the total number of cracks when a sufficient amount of fibers are used.
5) The significantly low faulting of Cell 806 compared to Cell 506 also revealed that fibers could potentially decrease the faulting when appropriate dosage or type of fibers are used.
6) The temperature gradient of all the cells was found to be linear to a great extent.

7) As much as 60% of the time, slabs experienced a negative temperature gradient.

8) The environmental strains measured showed that they possess a good relation with the temperature; however, a clear trend of the contribution of the fibers could not be established from the first year data.

9) No clear conclusions could be drawn at this time on the influence of the fibers on the slab size.

10) The dynamic strains were higher in general during the springtime when the base and subgrade support was weak.

11) Joint opening sensor data provided mixed results. Some cells showed greater joint openings than the other cells irrespective of the fiber dosages and cell designs.

12) FWD data collected during the first year of service could identify the contribution of fibers. The cells with more fibers showed higher load transfer compared to their counterparts.

6 REFERENCES

1. Barman, M., (2014). Joint Performance Characterization of Bonded Whitetopping Overlays. Ph. D Dissertation, Pittsburgh: University of Pittsburgh.Advisor: Vandenbossche, J.

2. Burnham and Tewfik (2007). Development of a Computer Program for Selecting Peak Dynamic Sensor Responses from Pavement Testing. Minnesota Department of Transportation. St. Paul, MN.

3. MnDOT (2018). Report on 2017 MnROAD Construction Activities, Report Number: MN/RC 2018-16, Minnesota Department of Transportation, St. Paul, Minnesota.

4. Selezneva, O., Jiang, J., Tayabji, S. D. (1998). Preliminary Evaluation and Analysis of LTPP Faulting Data – Final Report., Federal Highway Administration, Virgina.

APPENDIX A

First Year Distress Maps

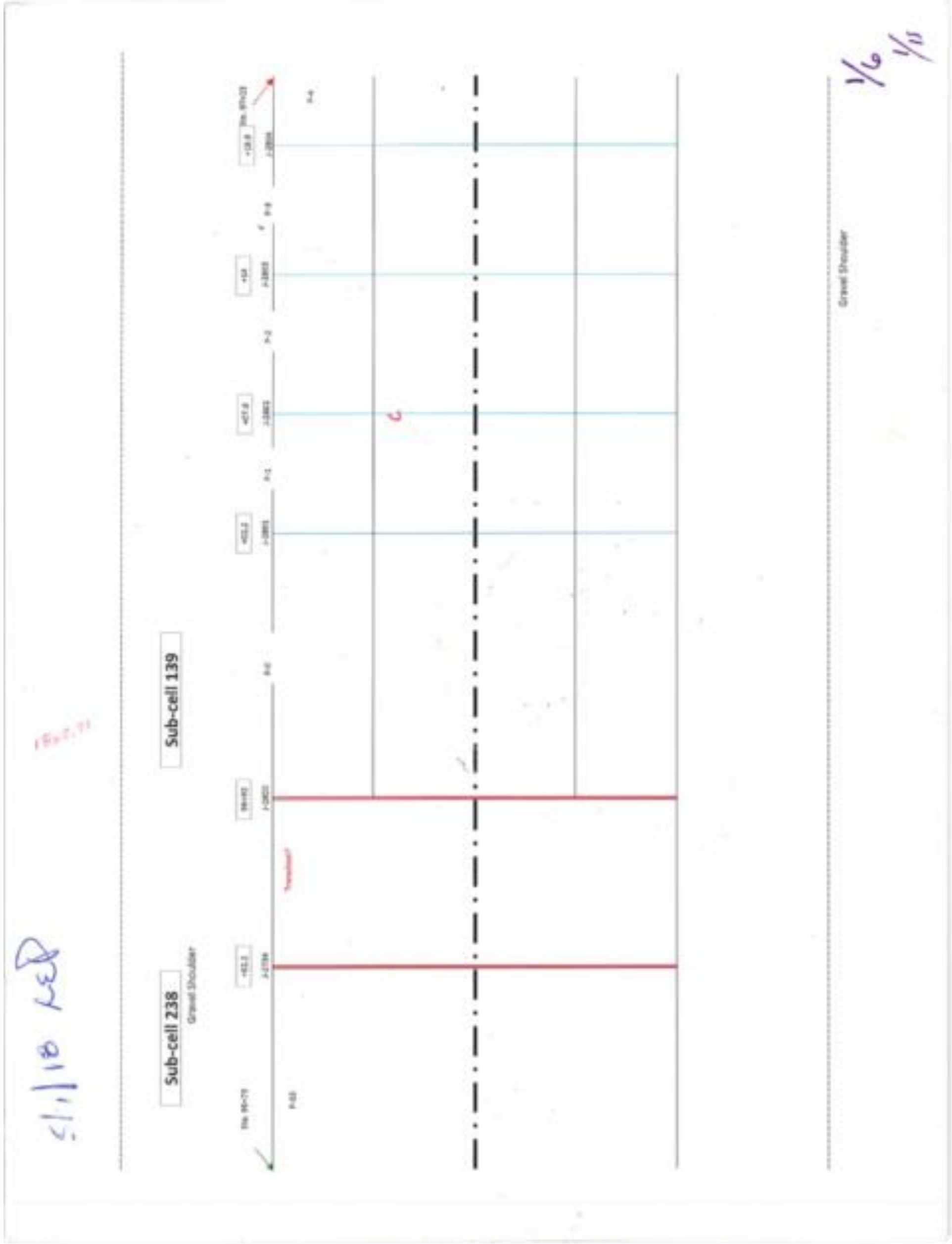

Figure A1: Distress map for Cell 139

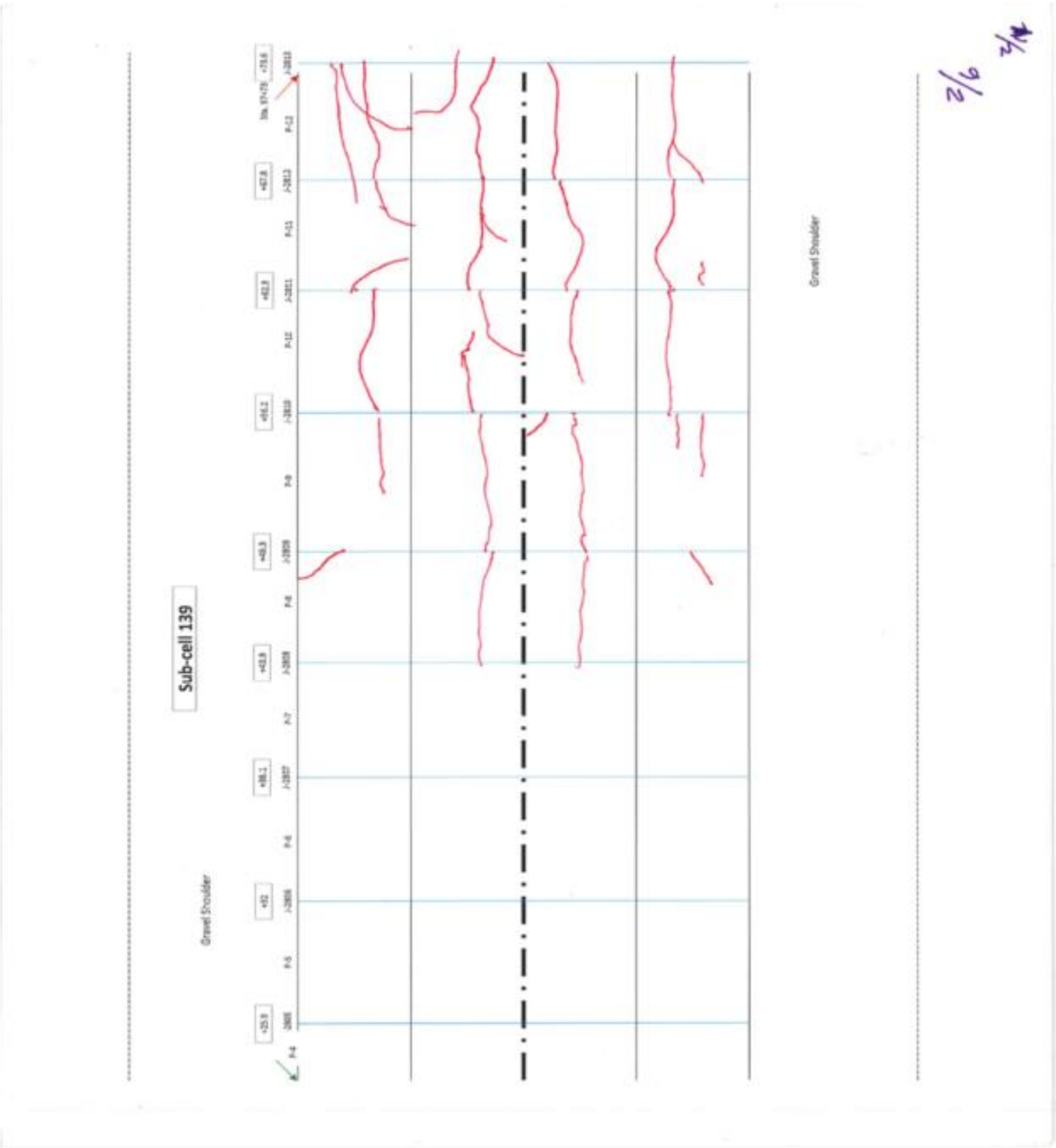

Figure A2: Distress map for Cell 139.. contd.

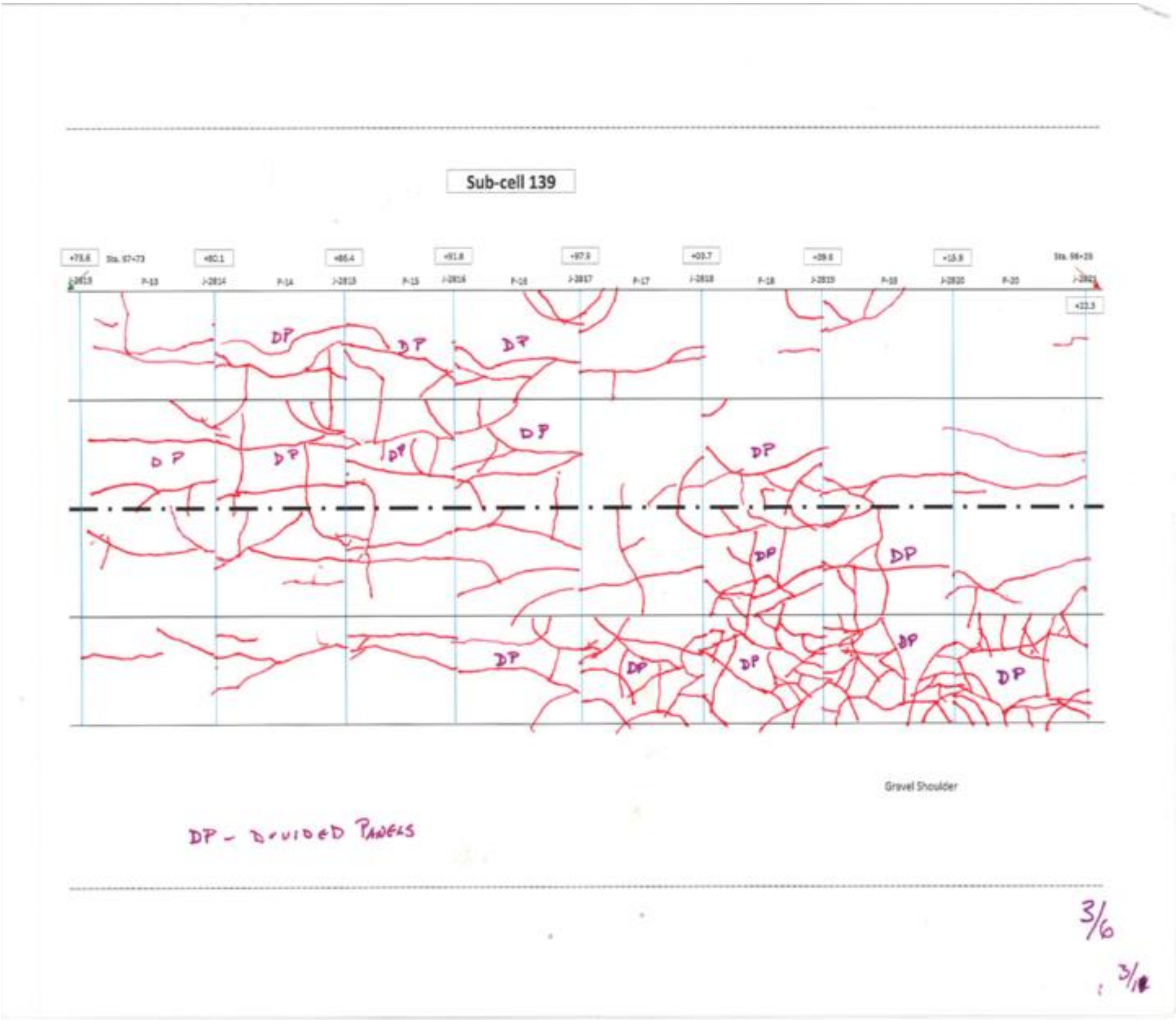

Figure A3: Distress map for Cell 139.. contd.

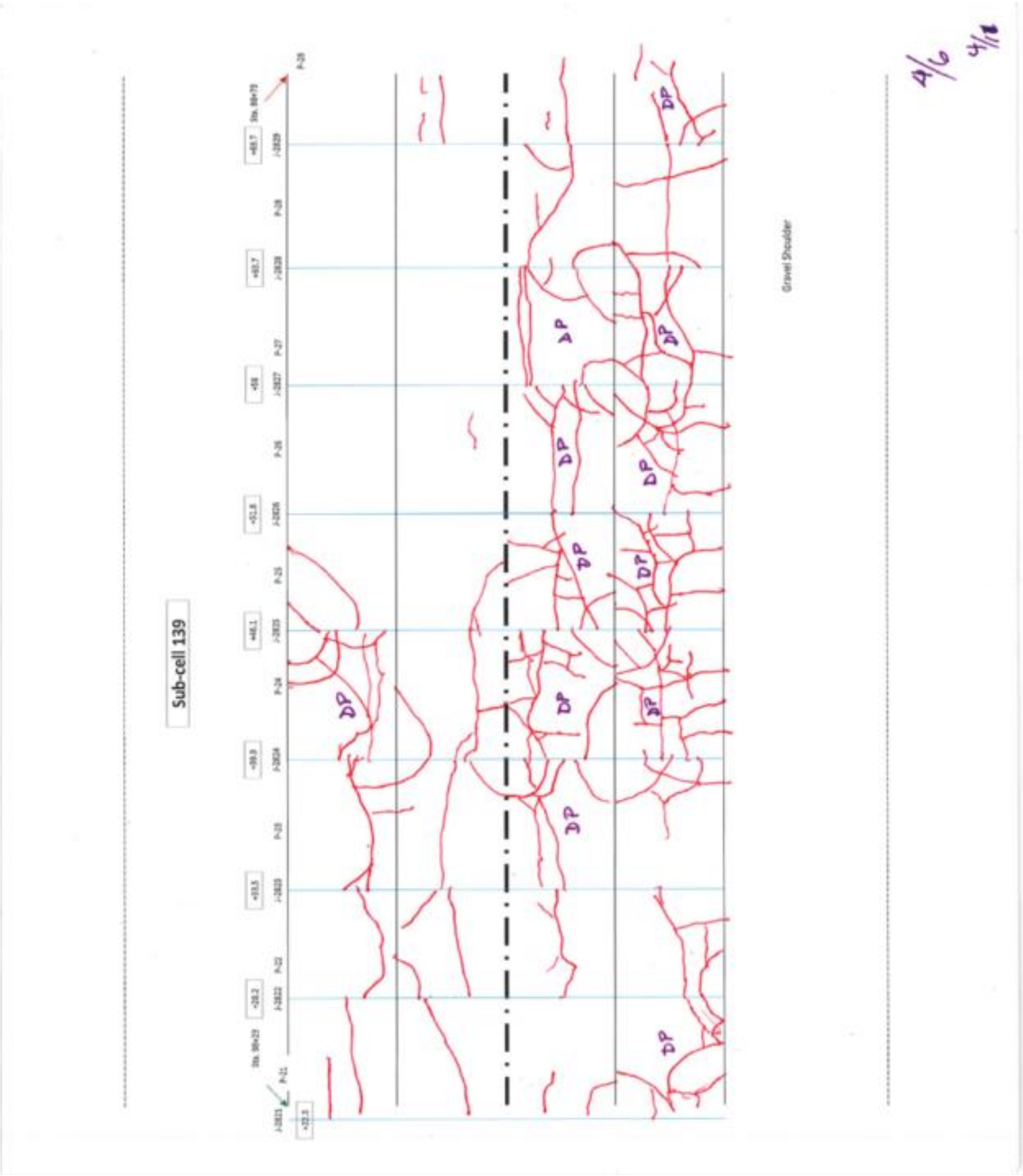

Figure A4: Distress map for Cell 139.. contd.

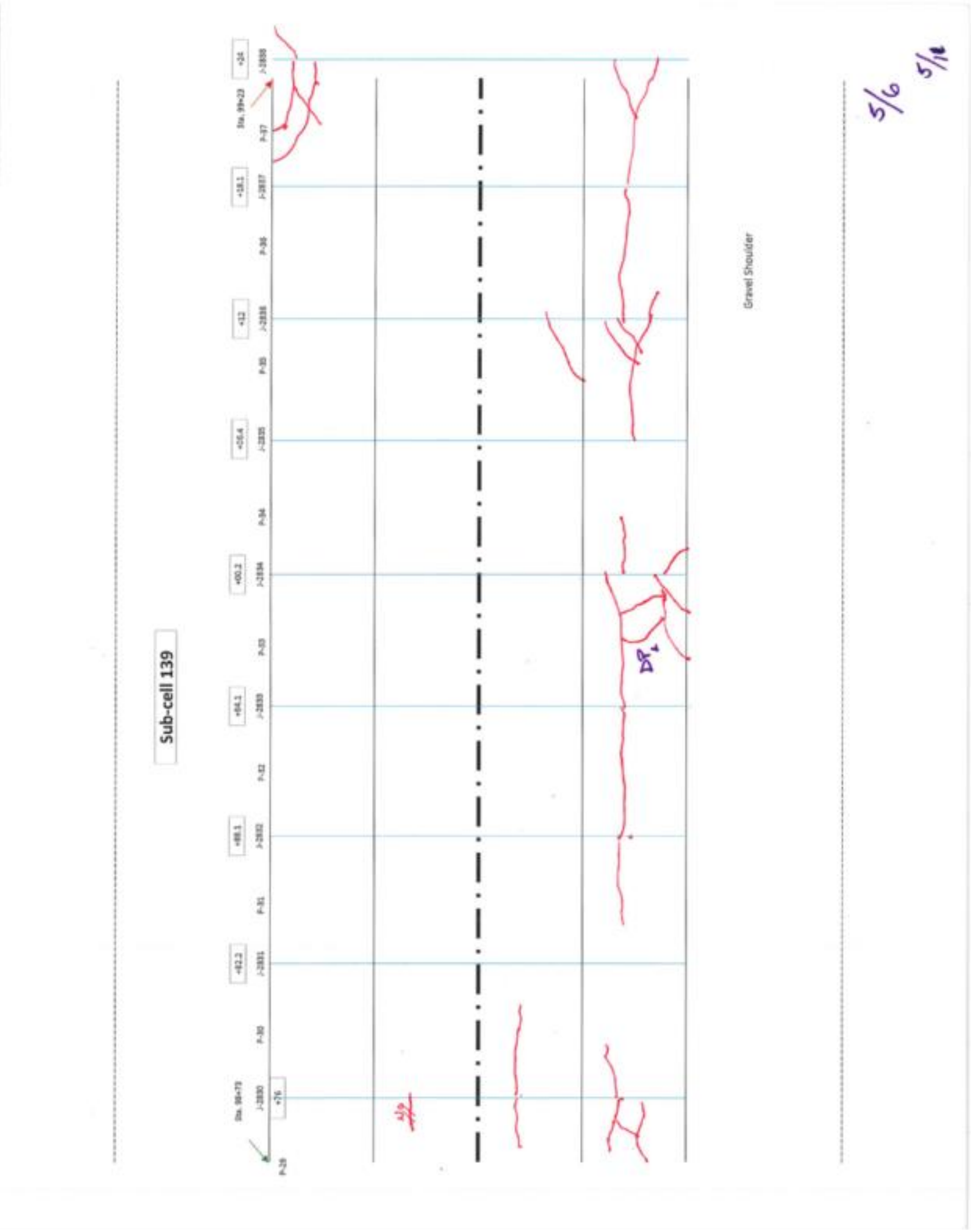

Figure A5: Distress map for Cell 139.. contd.

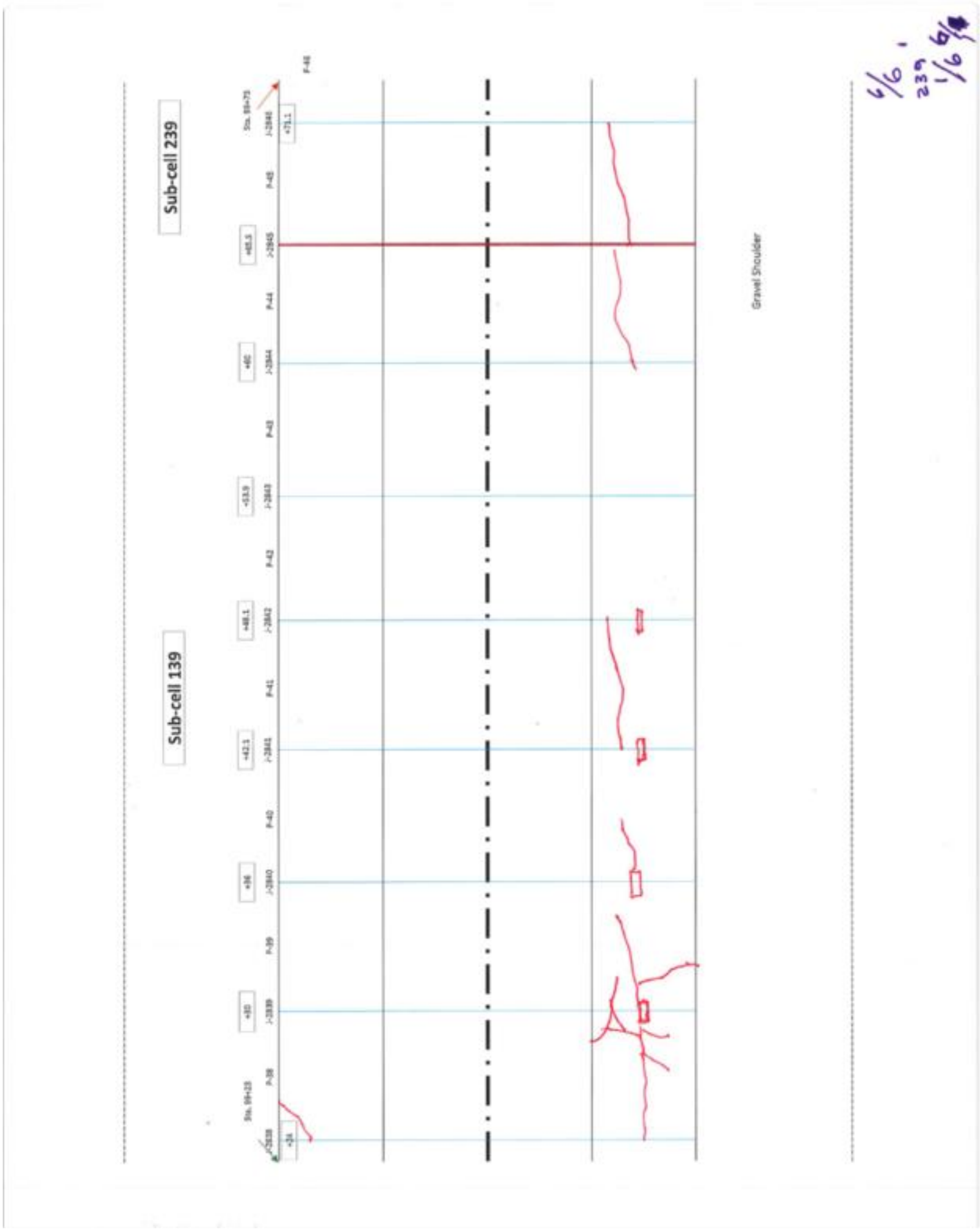

Figure A6: Distress map for Cell 139.. contd.

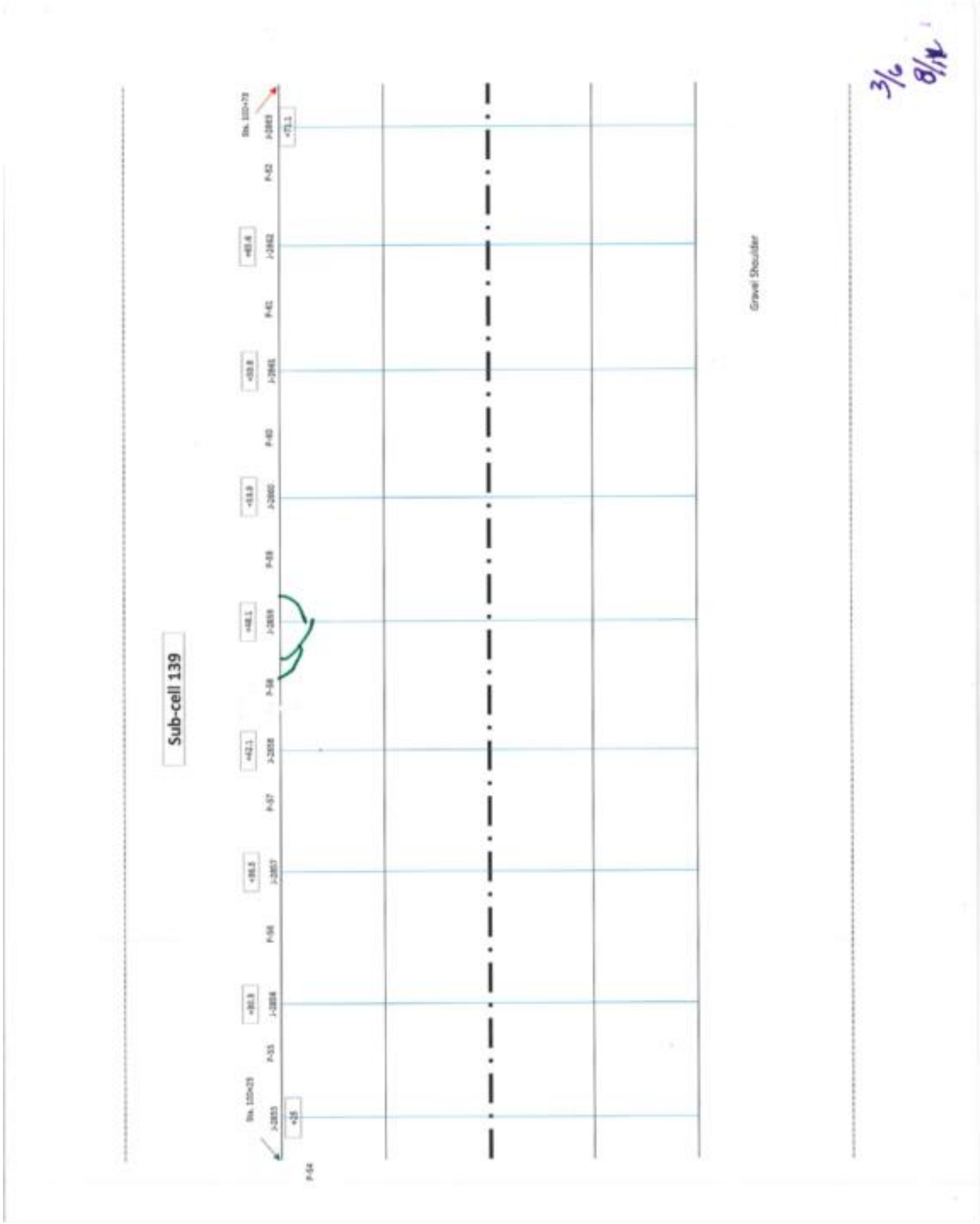

Figure A7: Distress map for Cell 139.. contd.

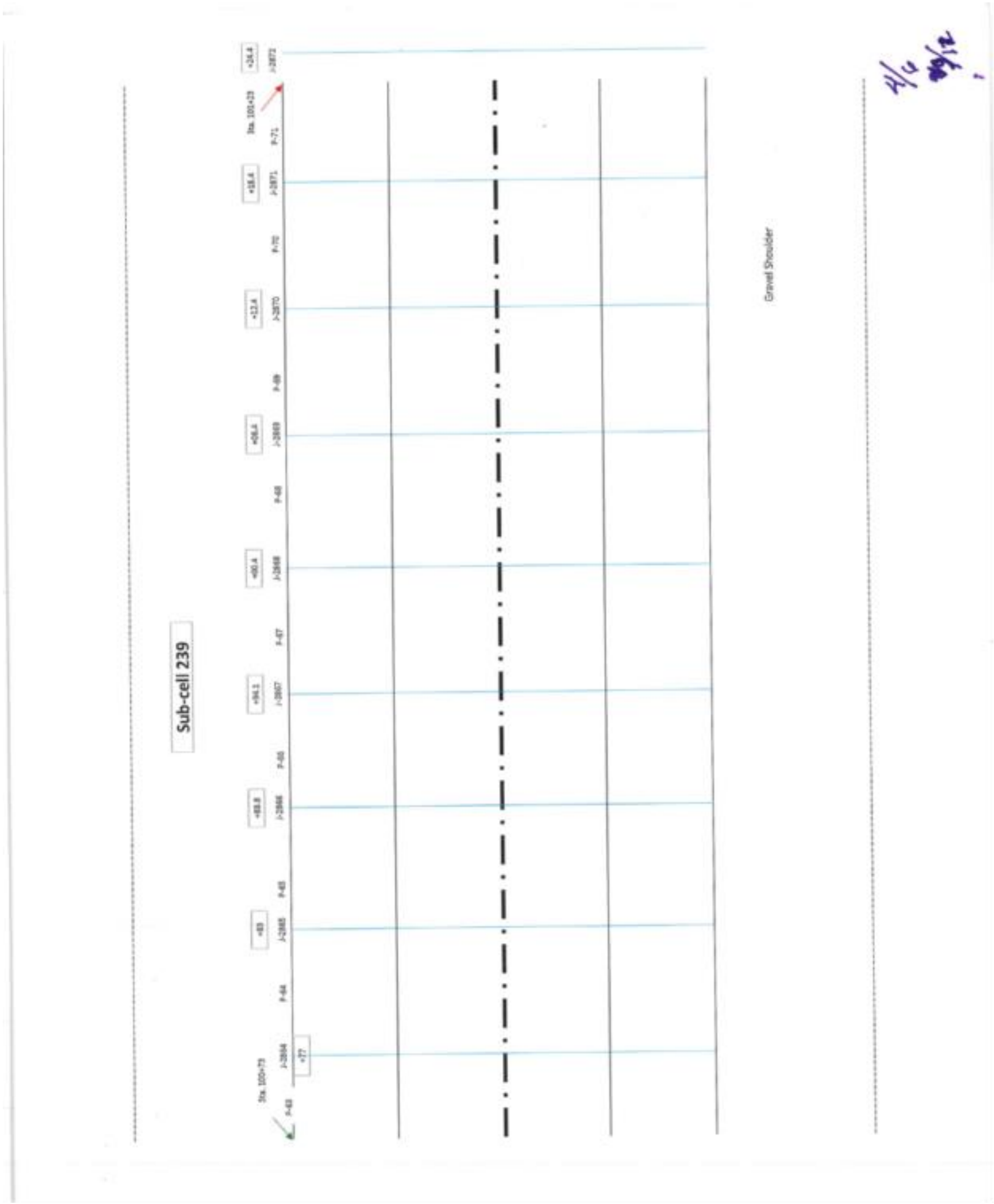

Figure A8: Distress map for Cell 239.

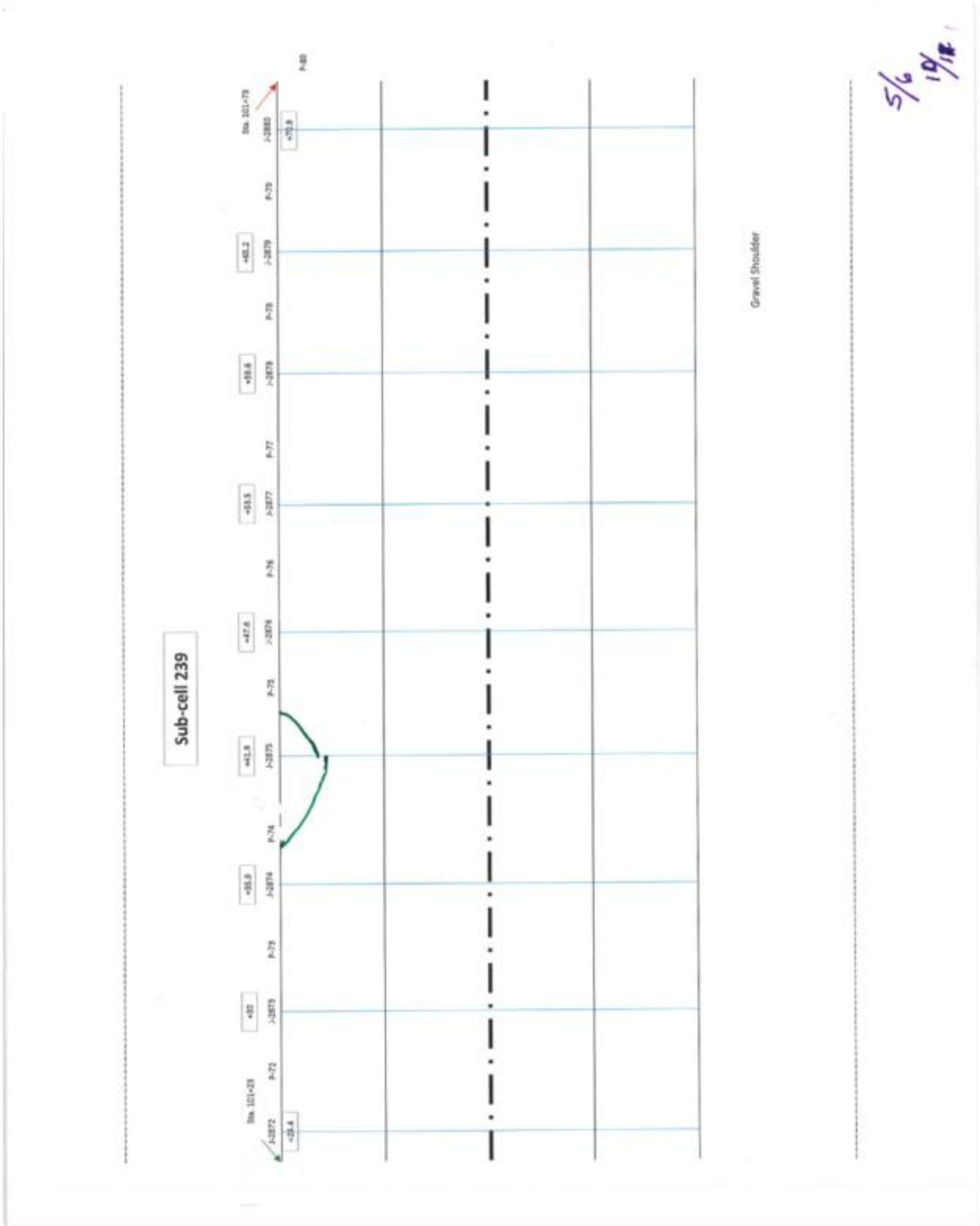

Figure A9: Distress map for Cell 239.. contd.

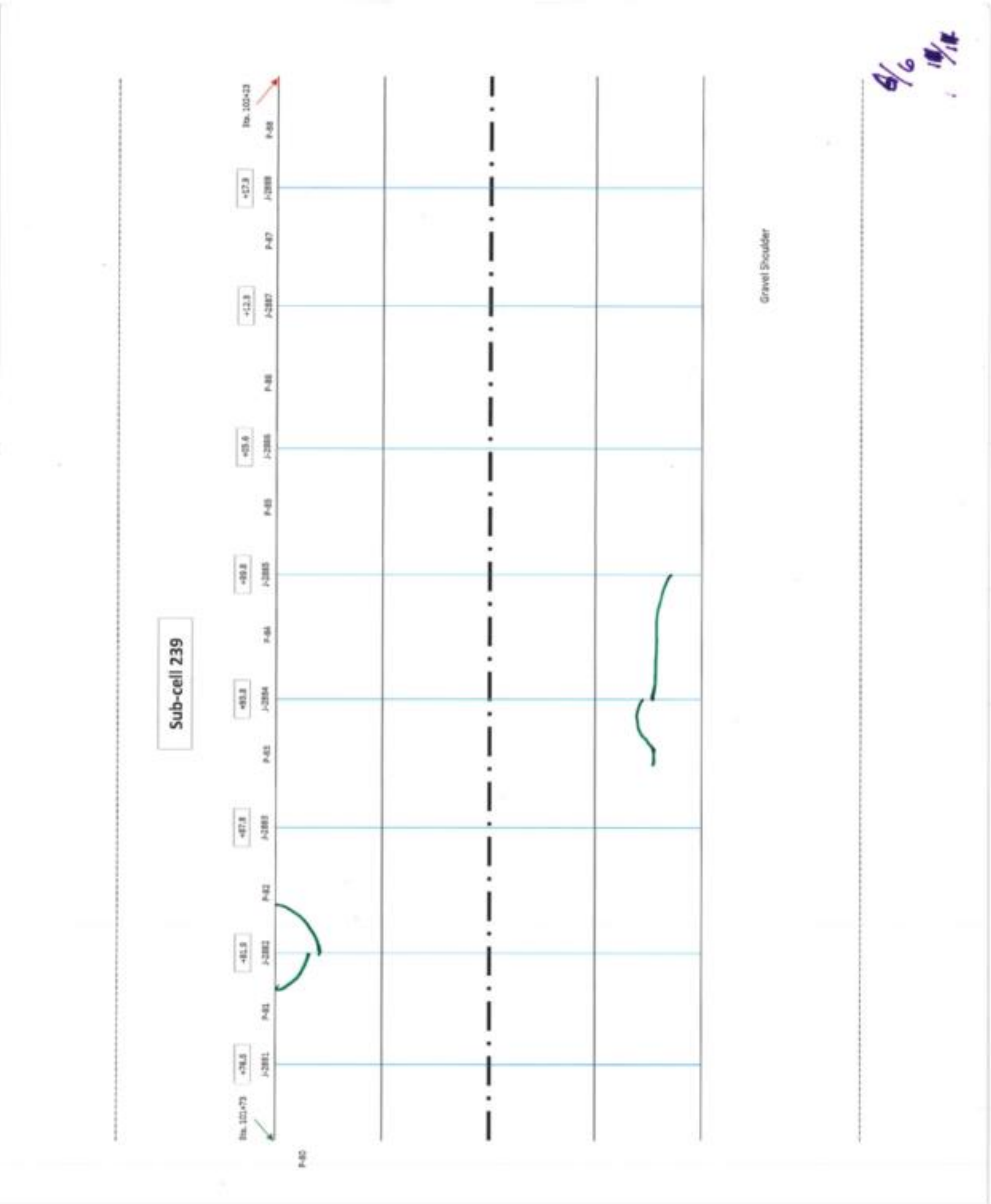

Figure A10: Distress map for Cell 239.. contd.

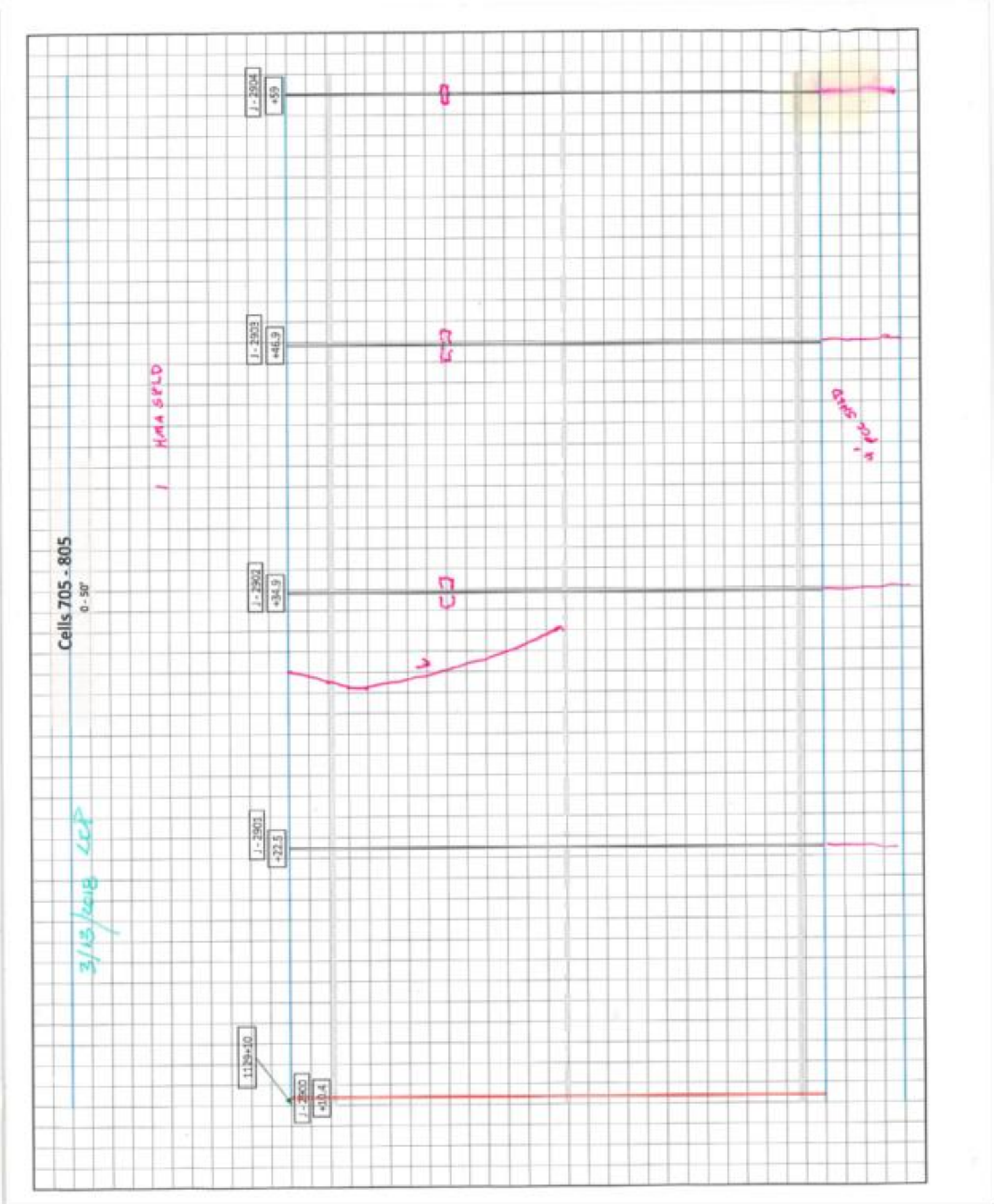

Figure A11: Distress map for Cells 705 and 805.

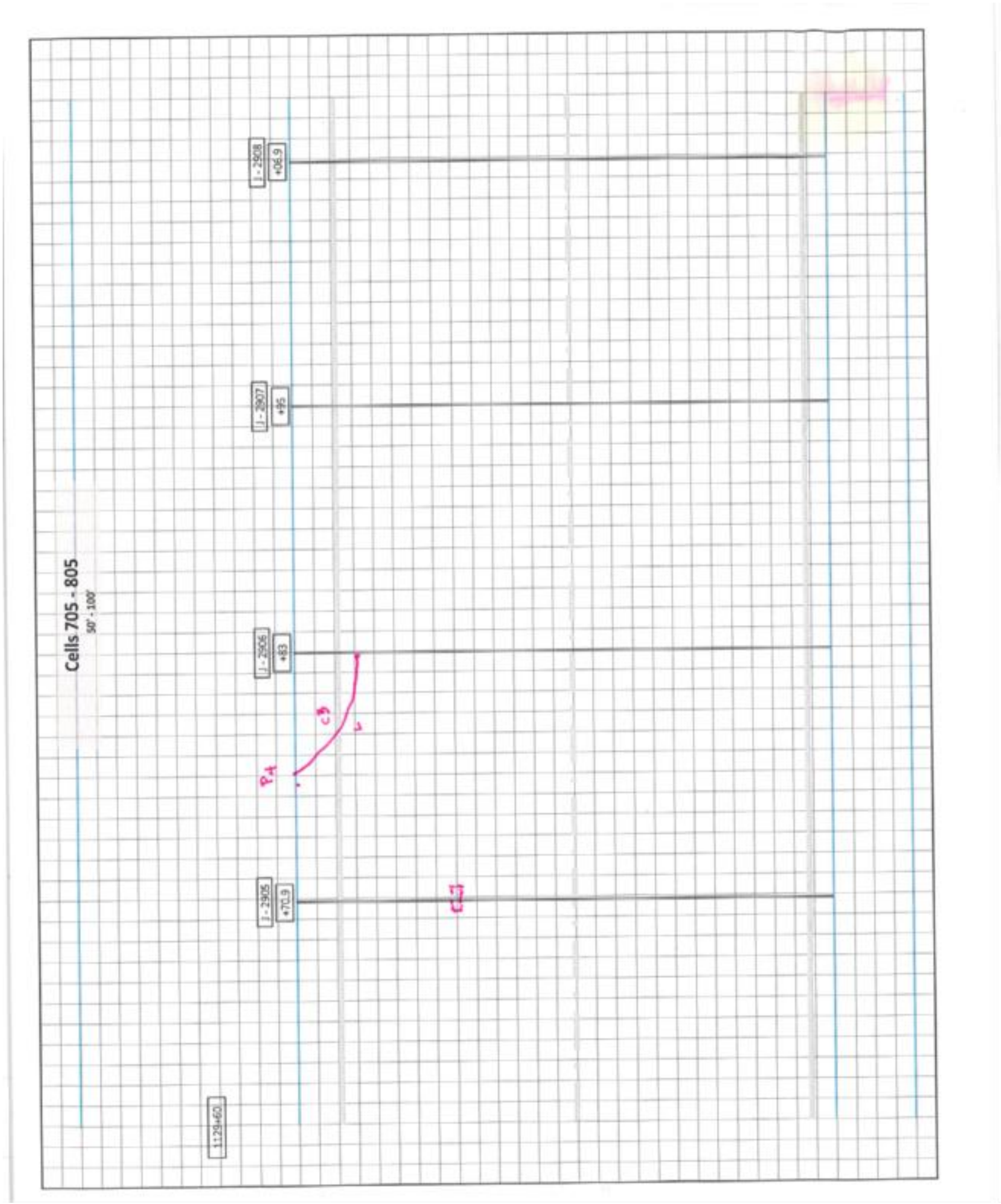

Figure A12: Distress map for Cells 705 and 805.. contd.

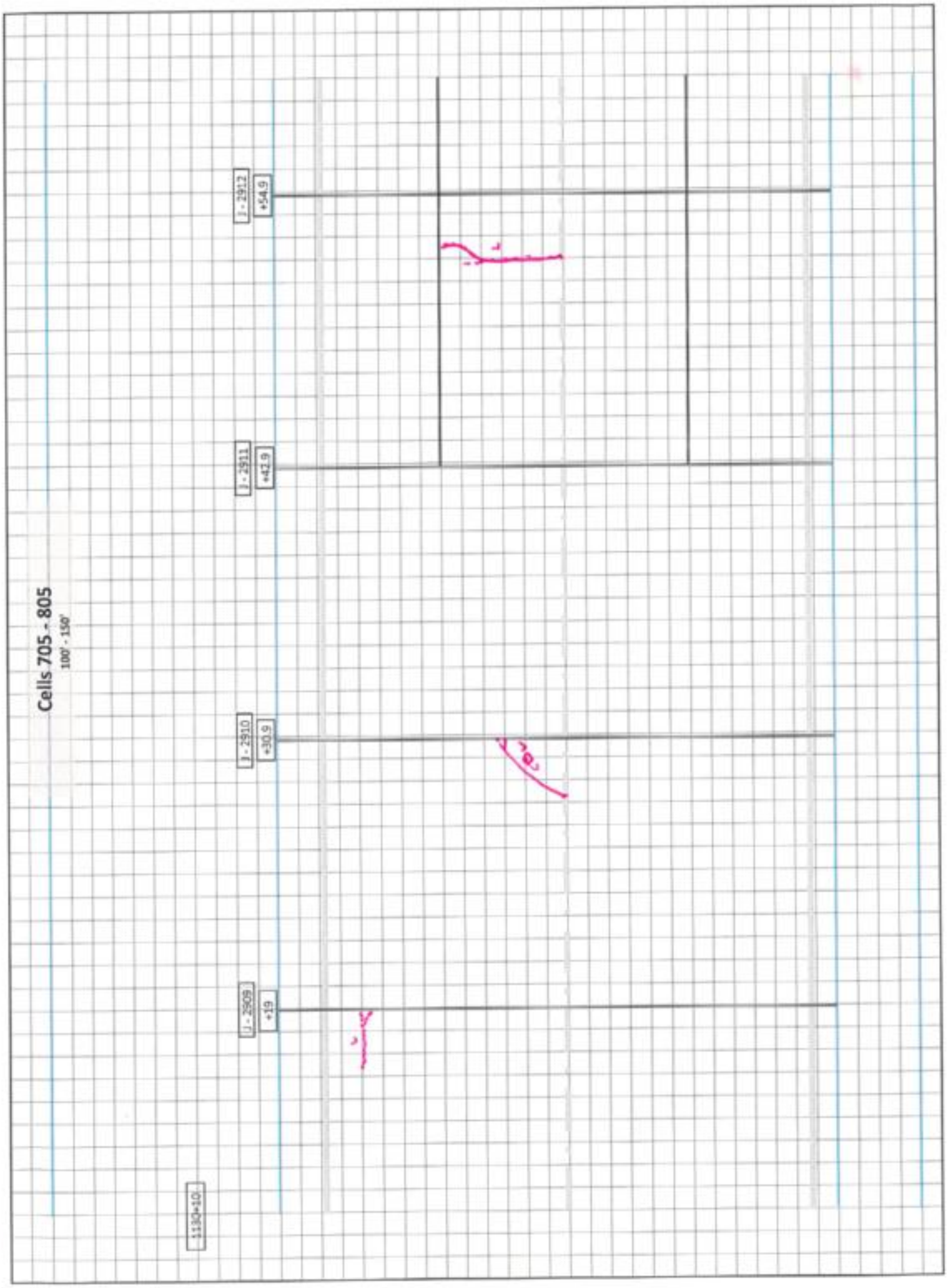

Figure A13: Distress map for Cells 705 and 805.. contd.

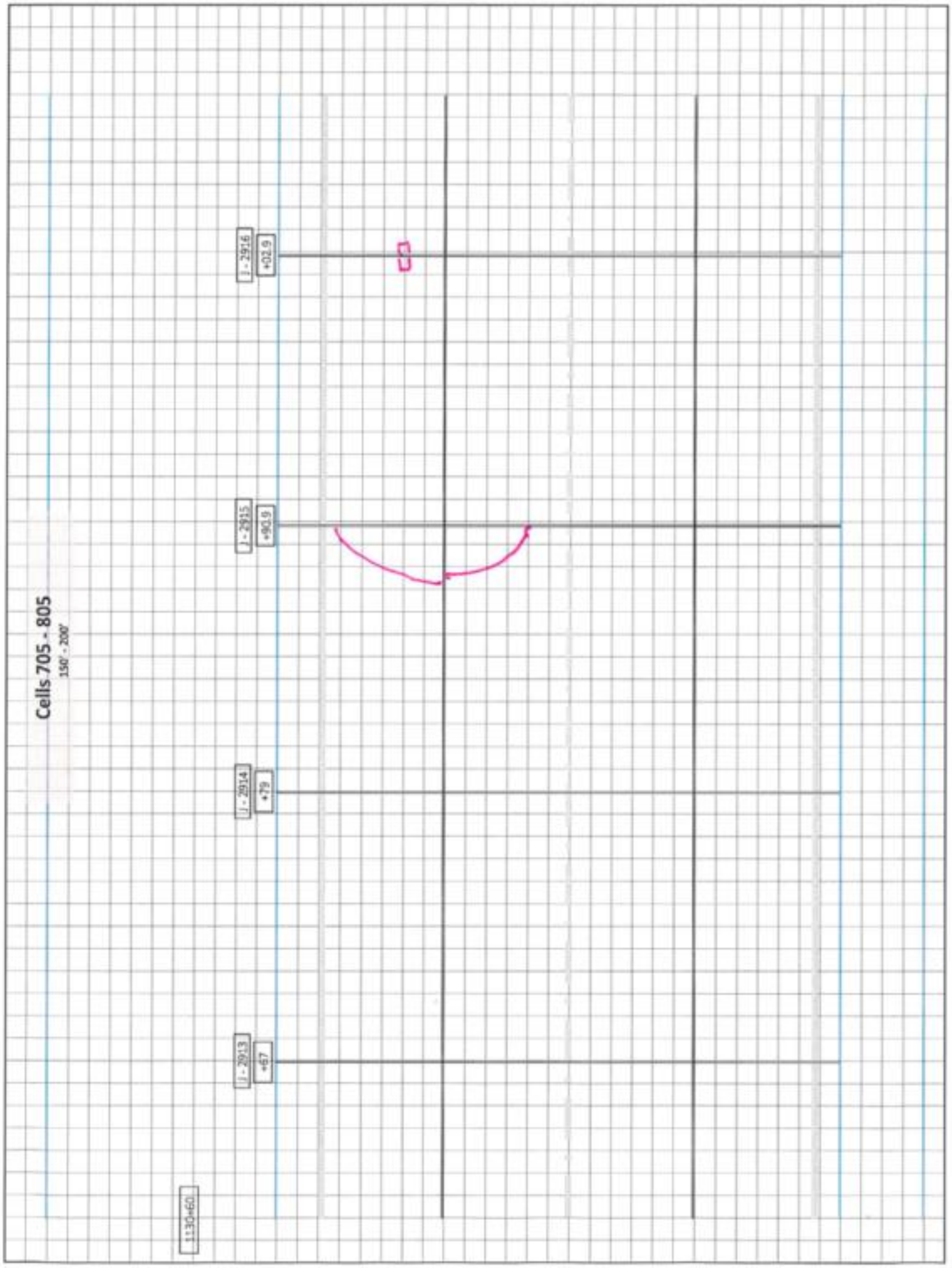

Figure A14: Distress map for Cells 705 and 805.. contd.

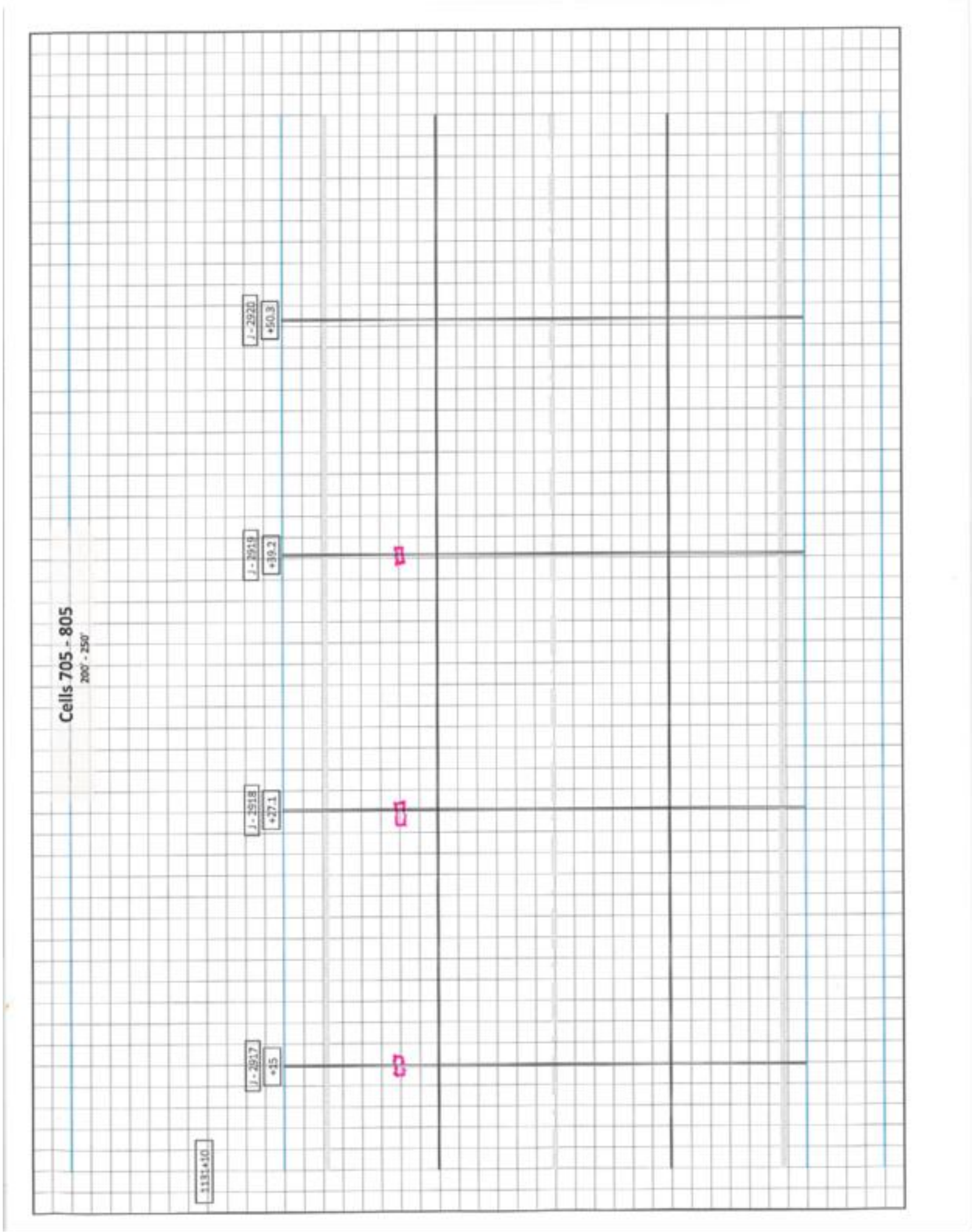

Figure A15: Distress map for Cells 705 and 805.. contd.

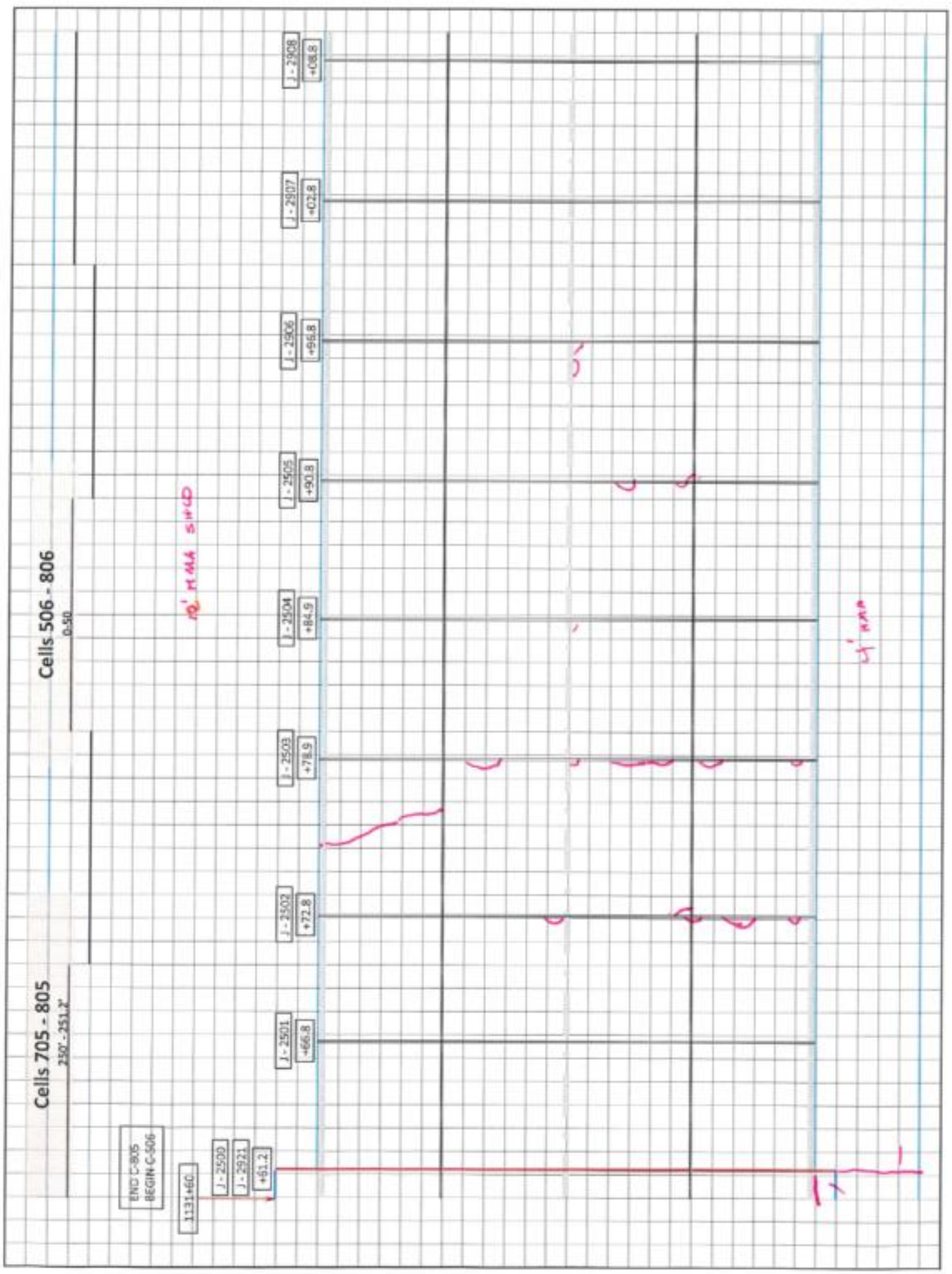

Figure A16: Distress map for Cells 705 and 805.. contd.

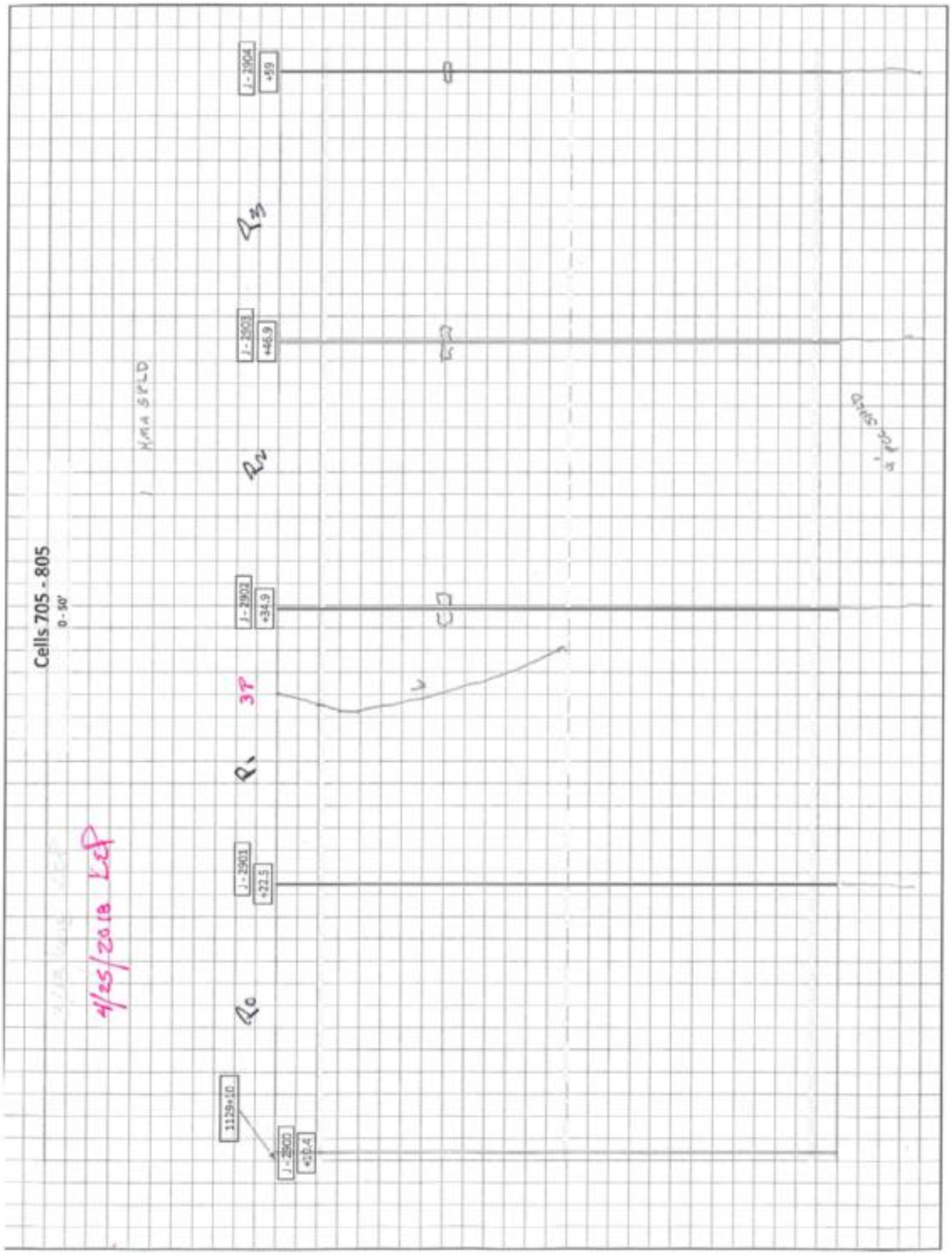

Figure A17: Distress map for Cells 705 and 805.. contd.

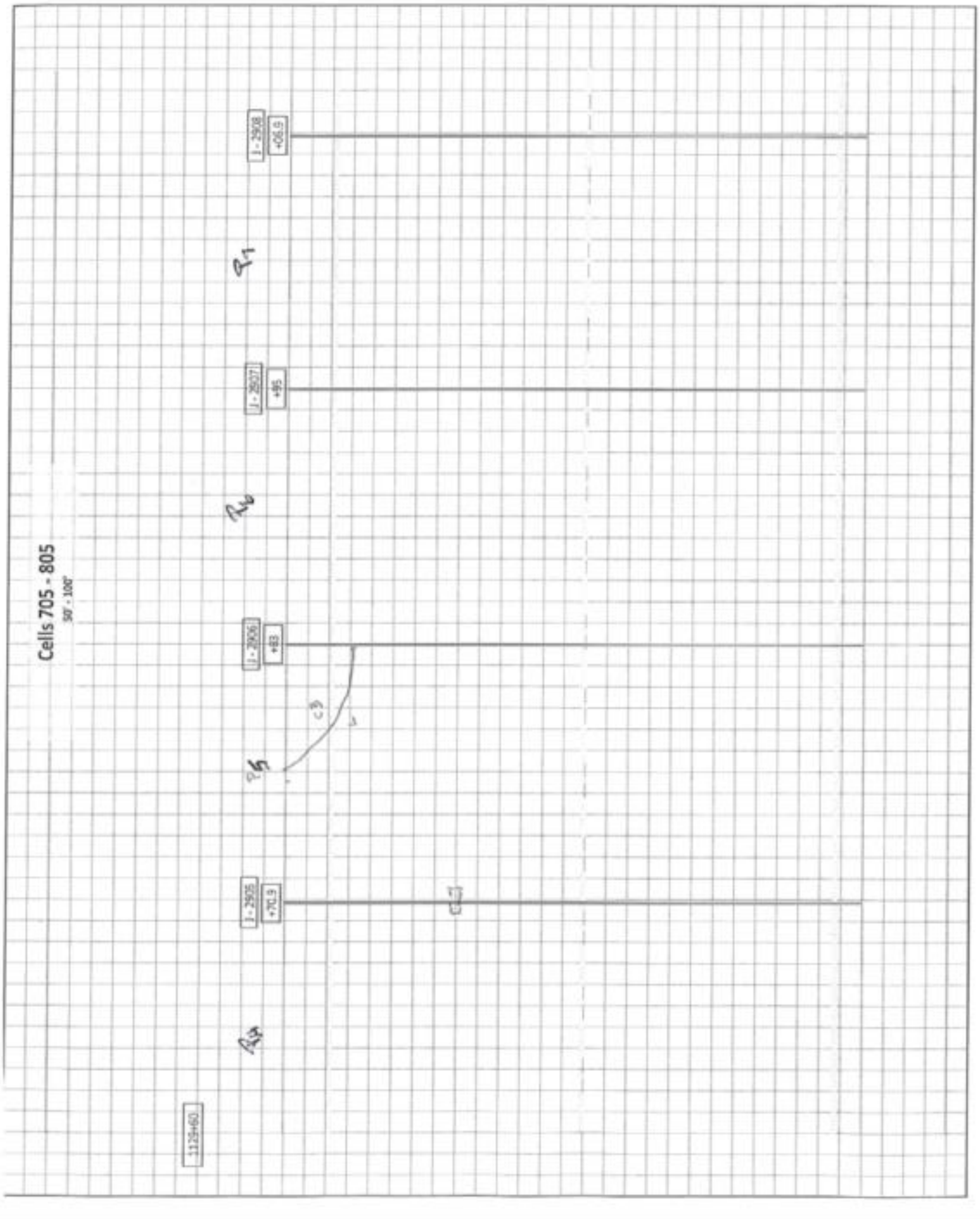

Figure A18: Distress map for Cells 705 and 805.. contd.

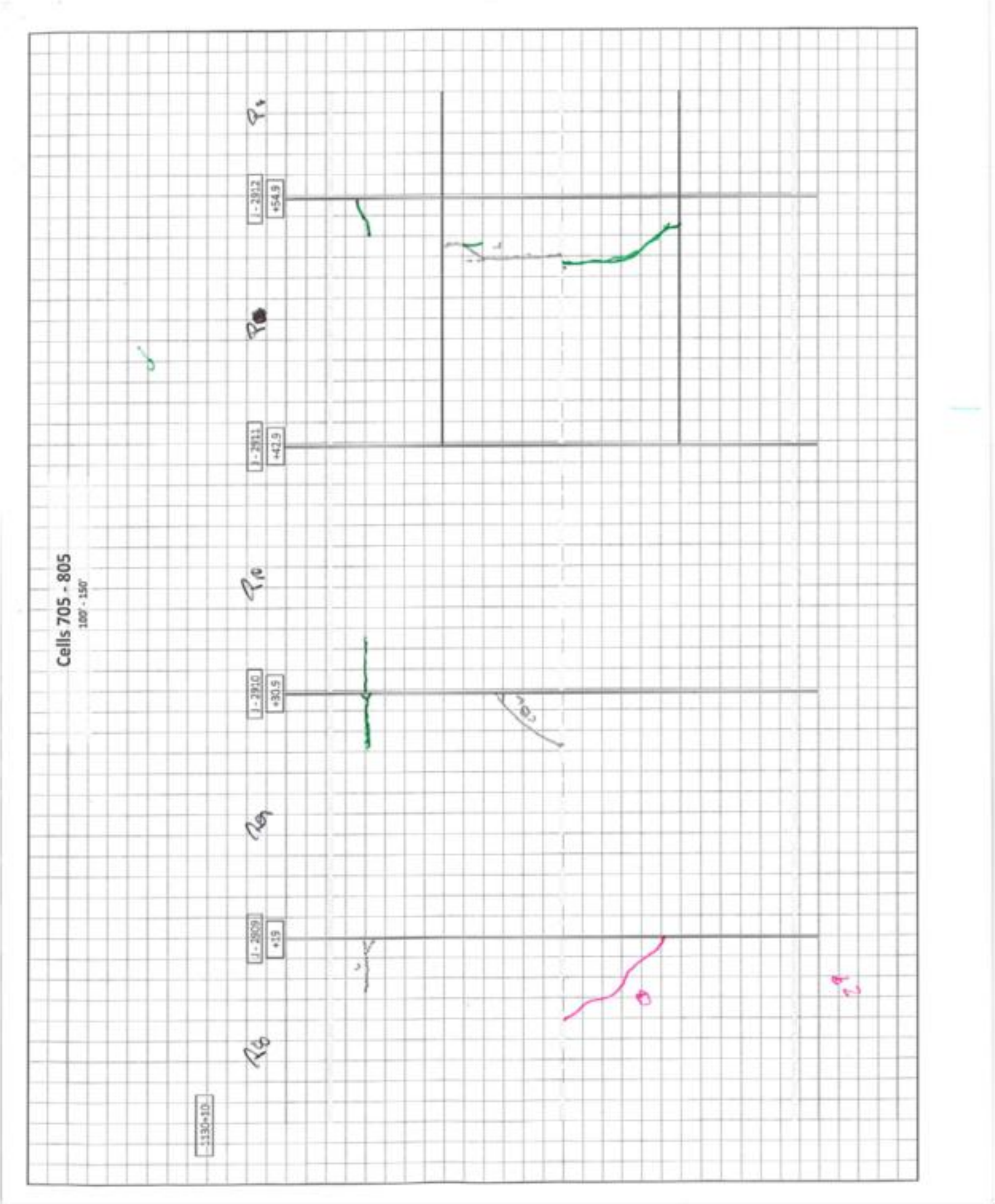

Figure A19: Distress map for Cells 705 and 805.. contd.

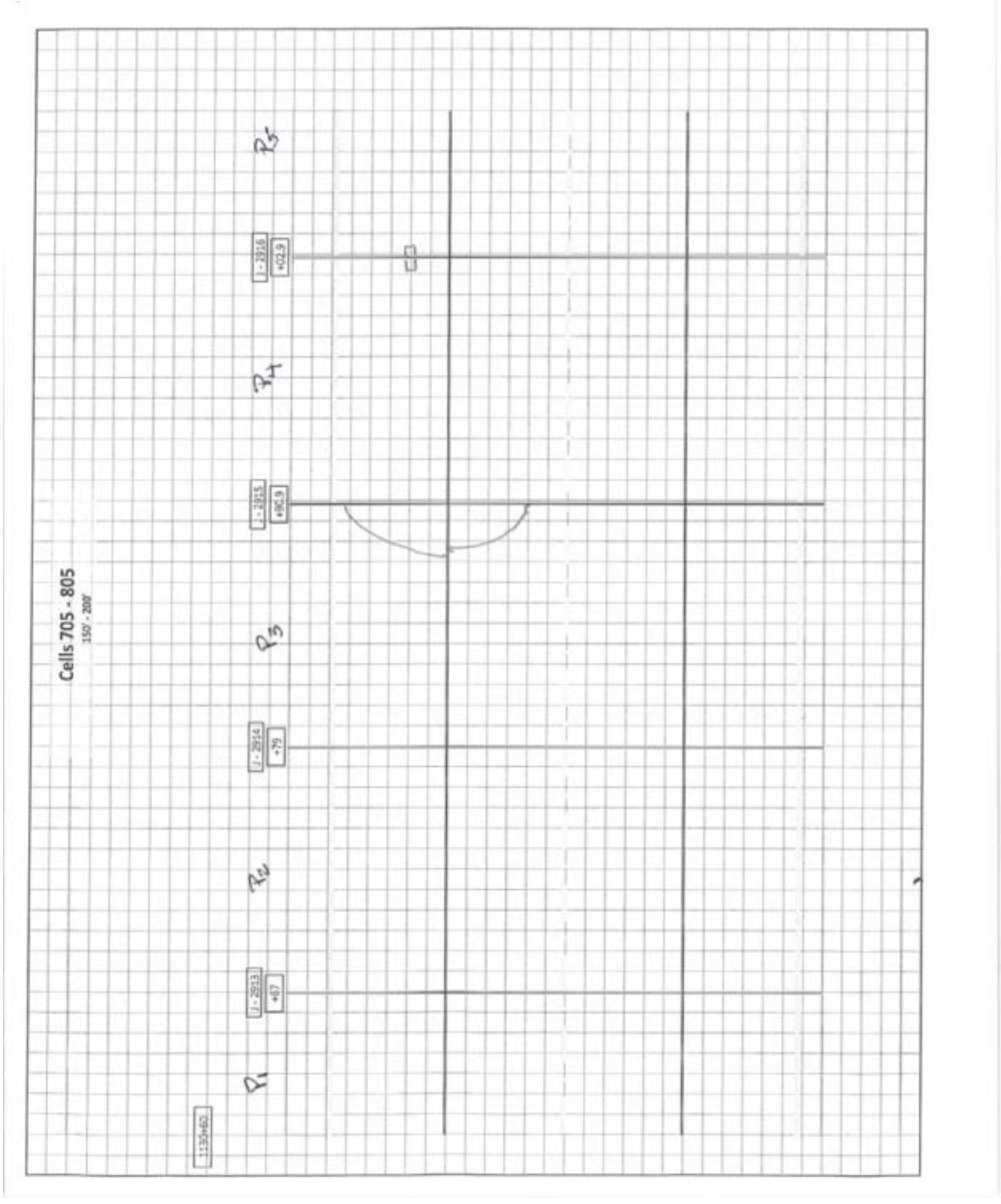

Figure A20: Distress map for Cells 705 and 805.. contd.

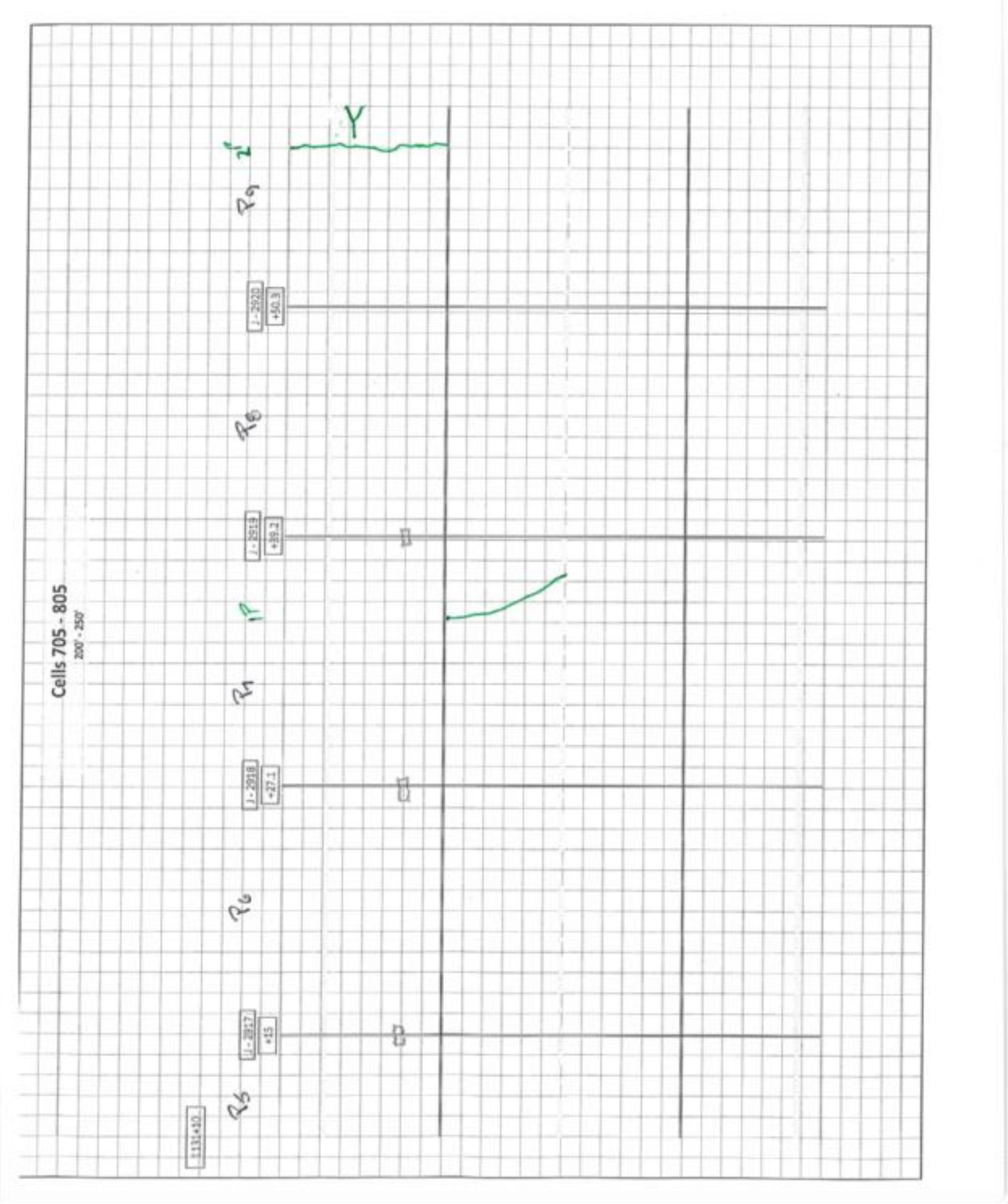

Figure A21: Distress map for Cells 705 and 805.. contd.

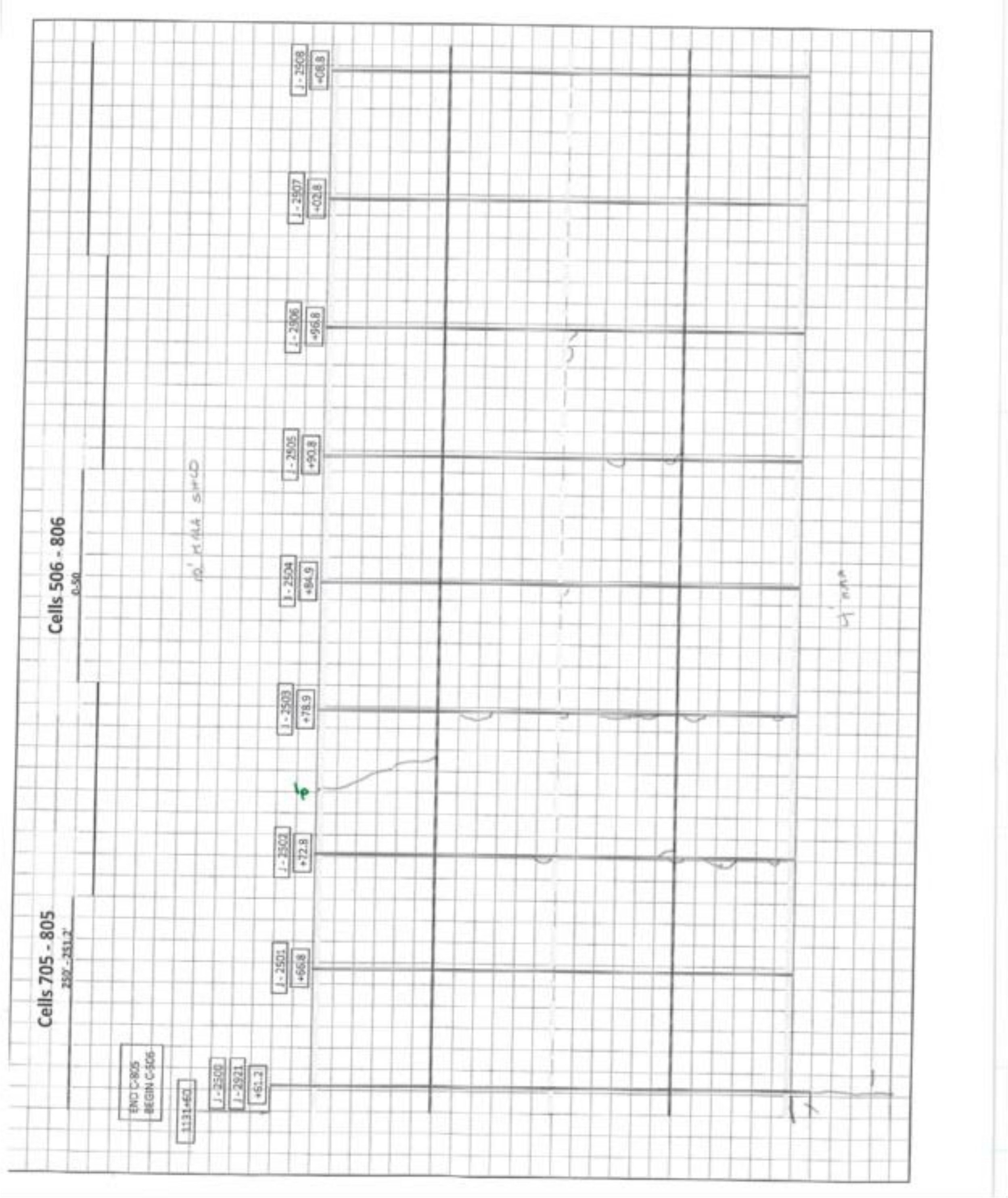

Figure A22: Distress map for Cells 705 and 805.. contd.

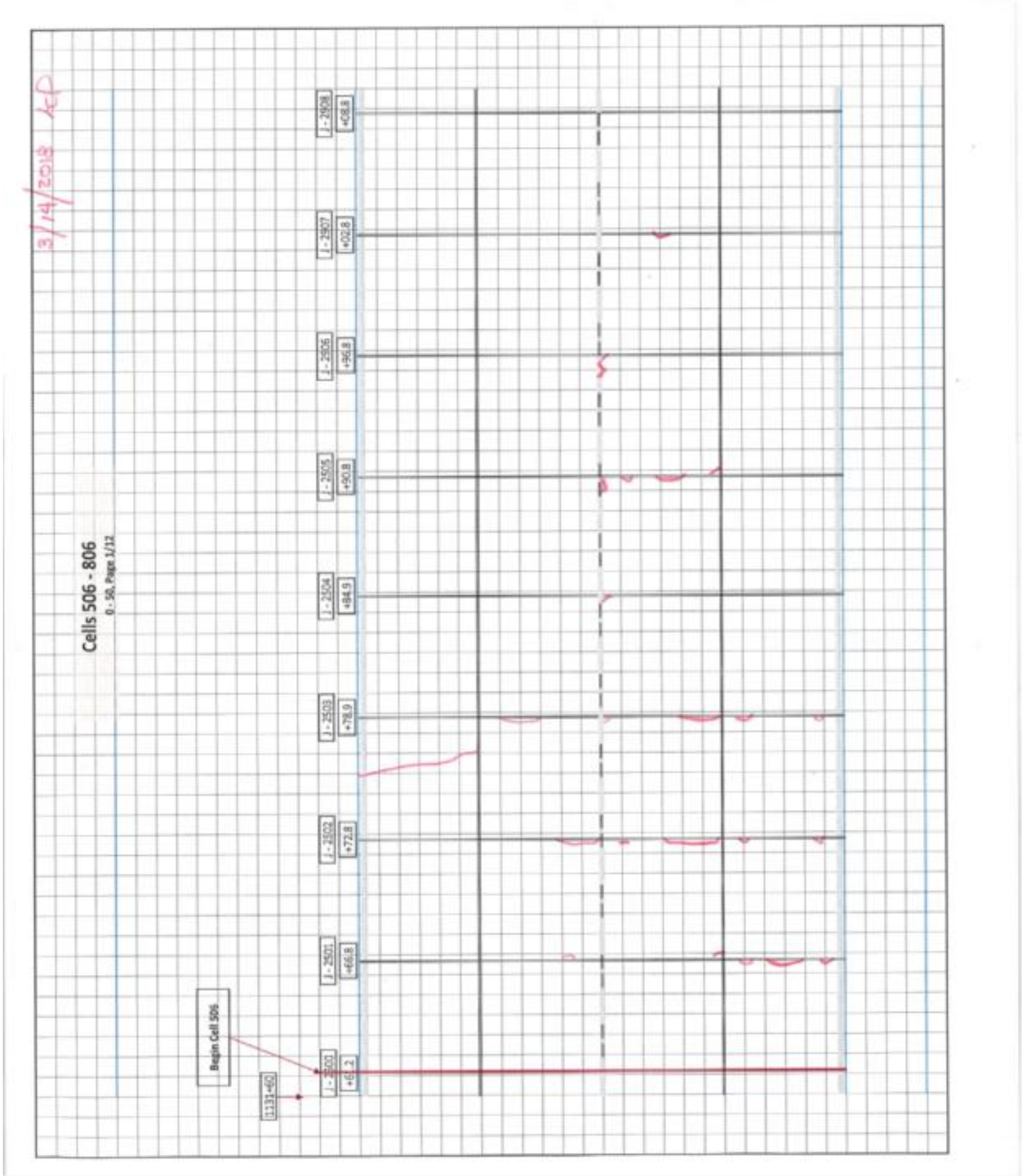

Figure A23: Distress map for Cells 506 through 806.

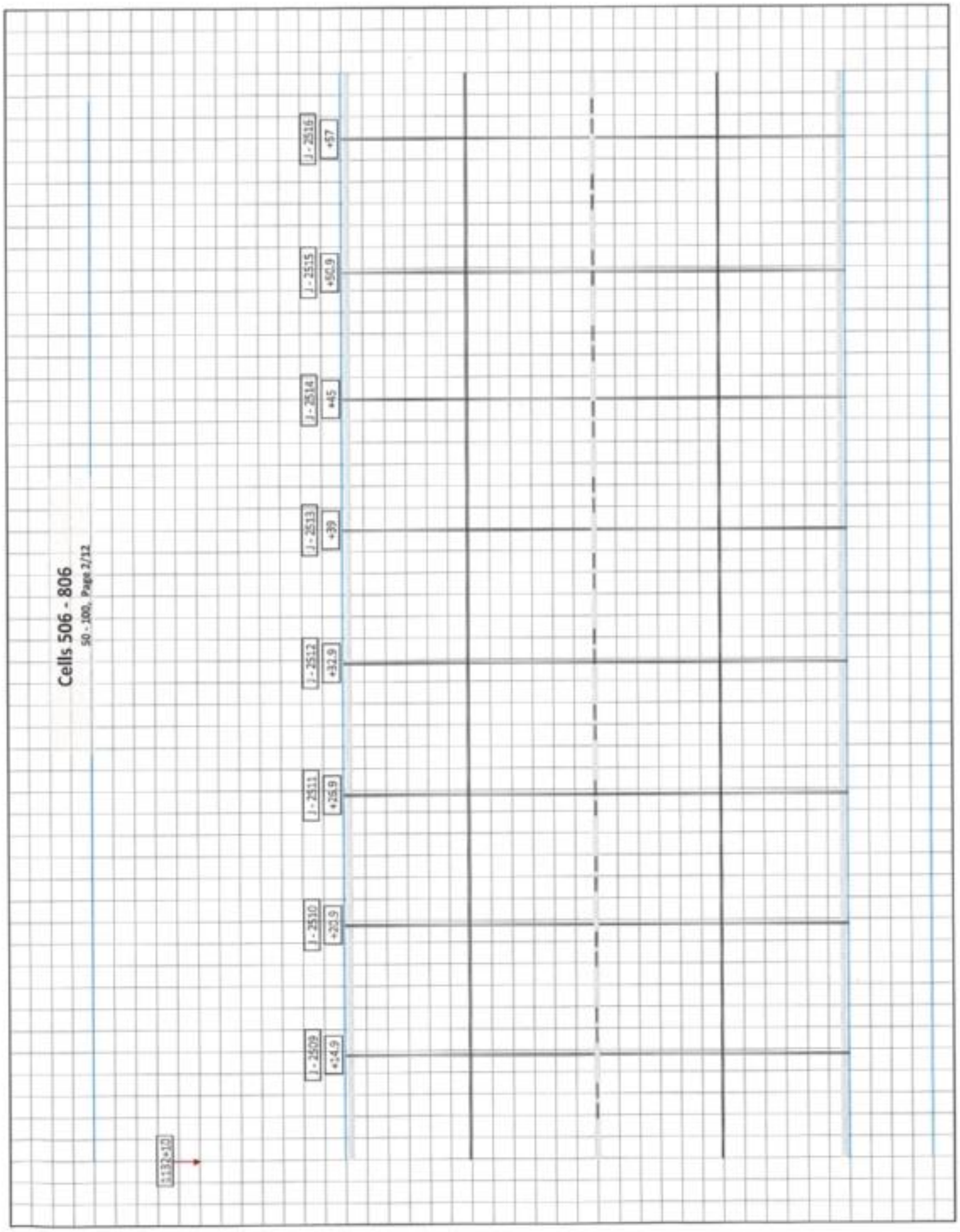

Figure A24: Distress map for Cells 506 through 806.. contd.

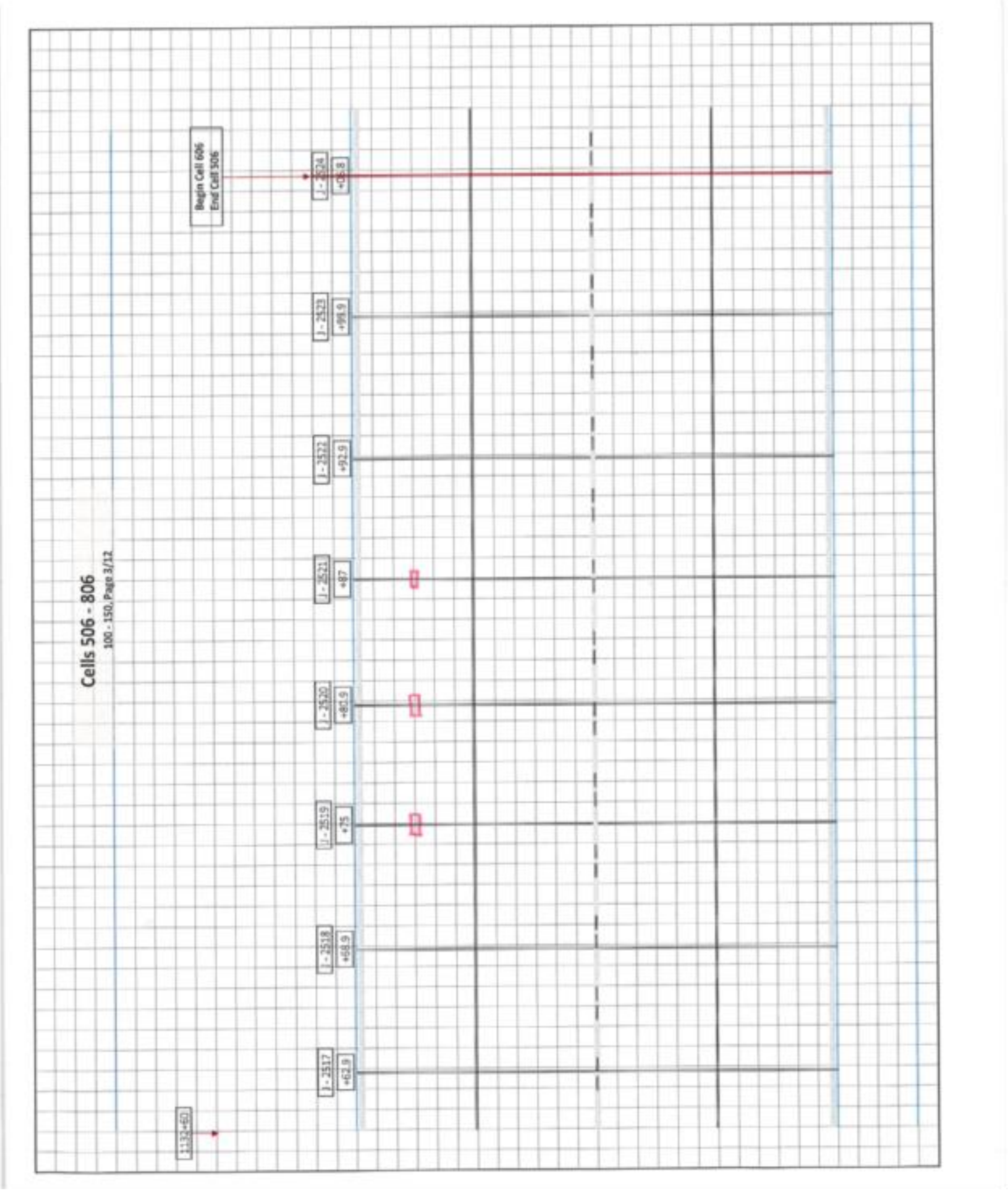

Figure A25: Distress map for Cells 506 through 806.. contd.

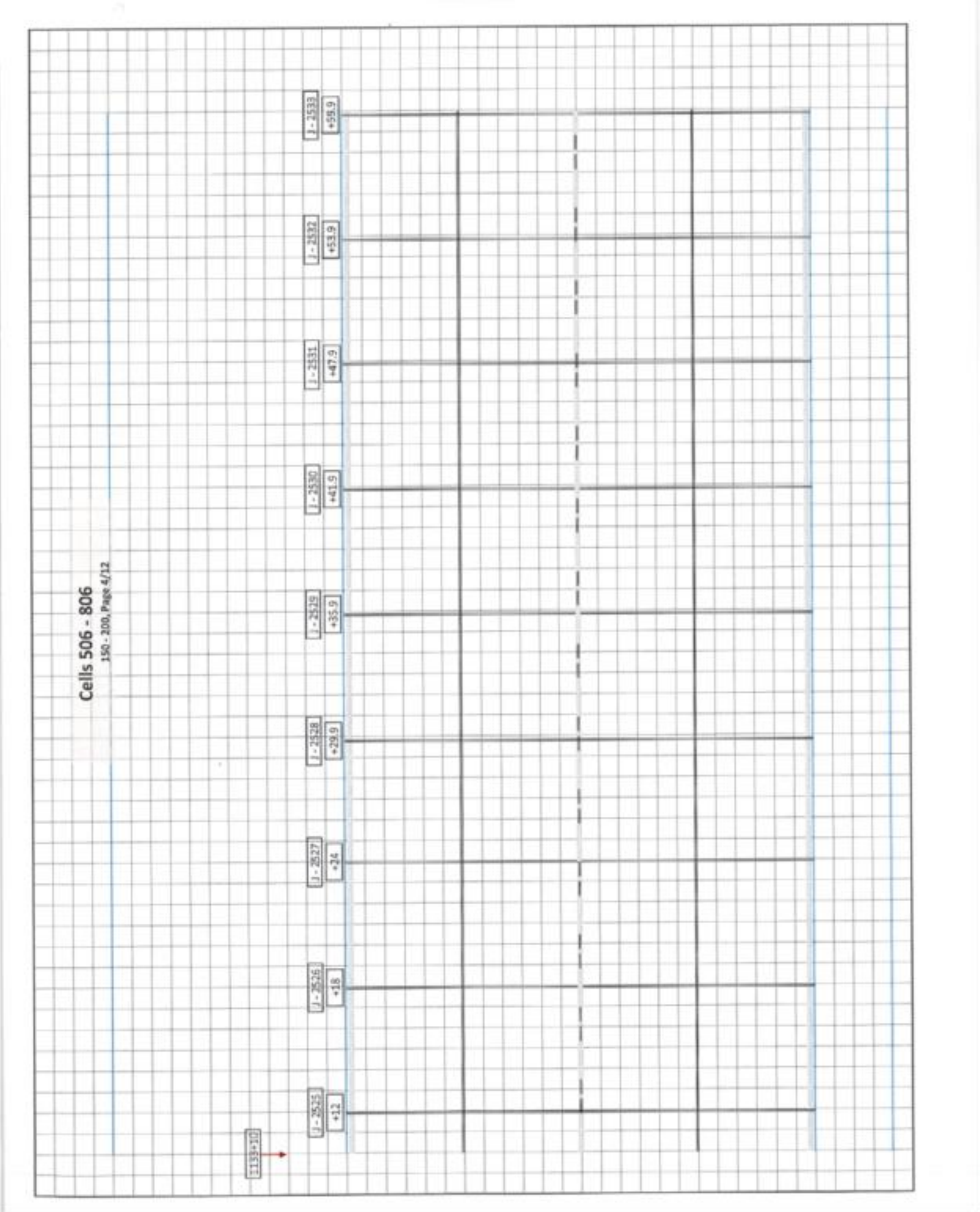

Figure A26: Distress map for Cells 506 through 806.. contd.

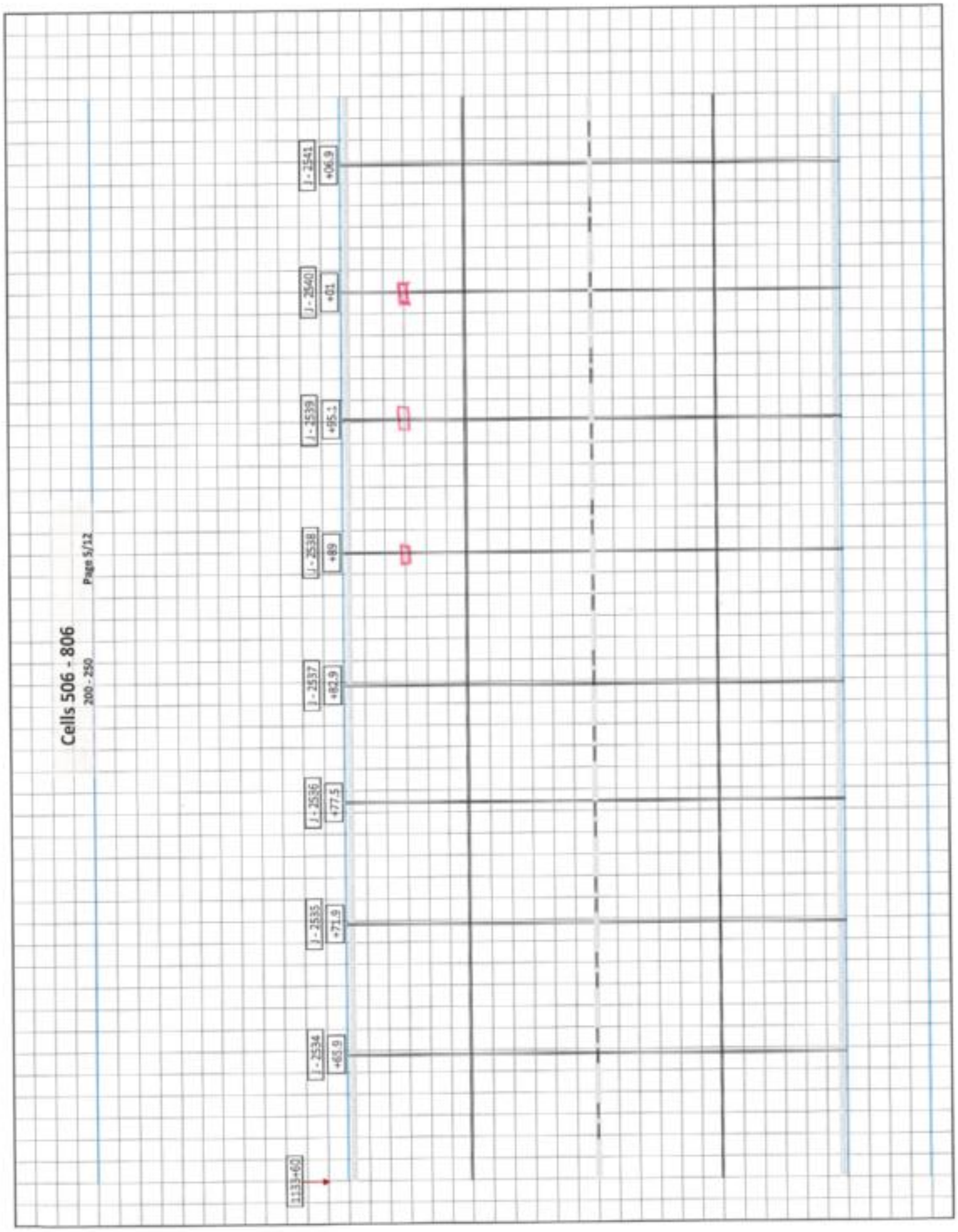

Figure A27: Distress map for Cells 506 through 806.. contd.

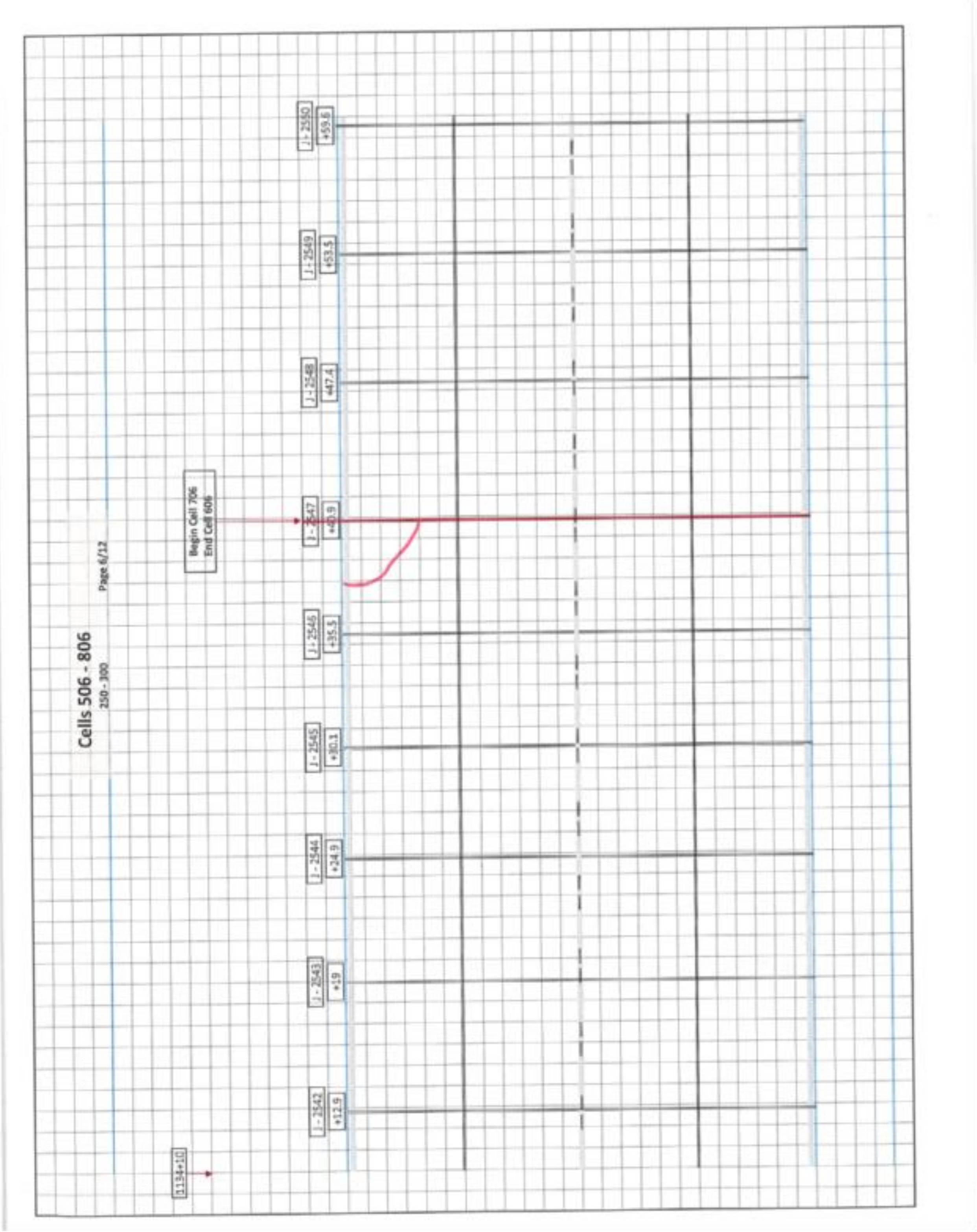

Figure A28: Distress map for Cells 506 through 806.. contd.

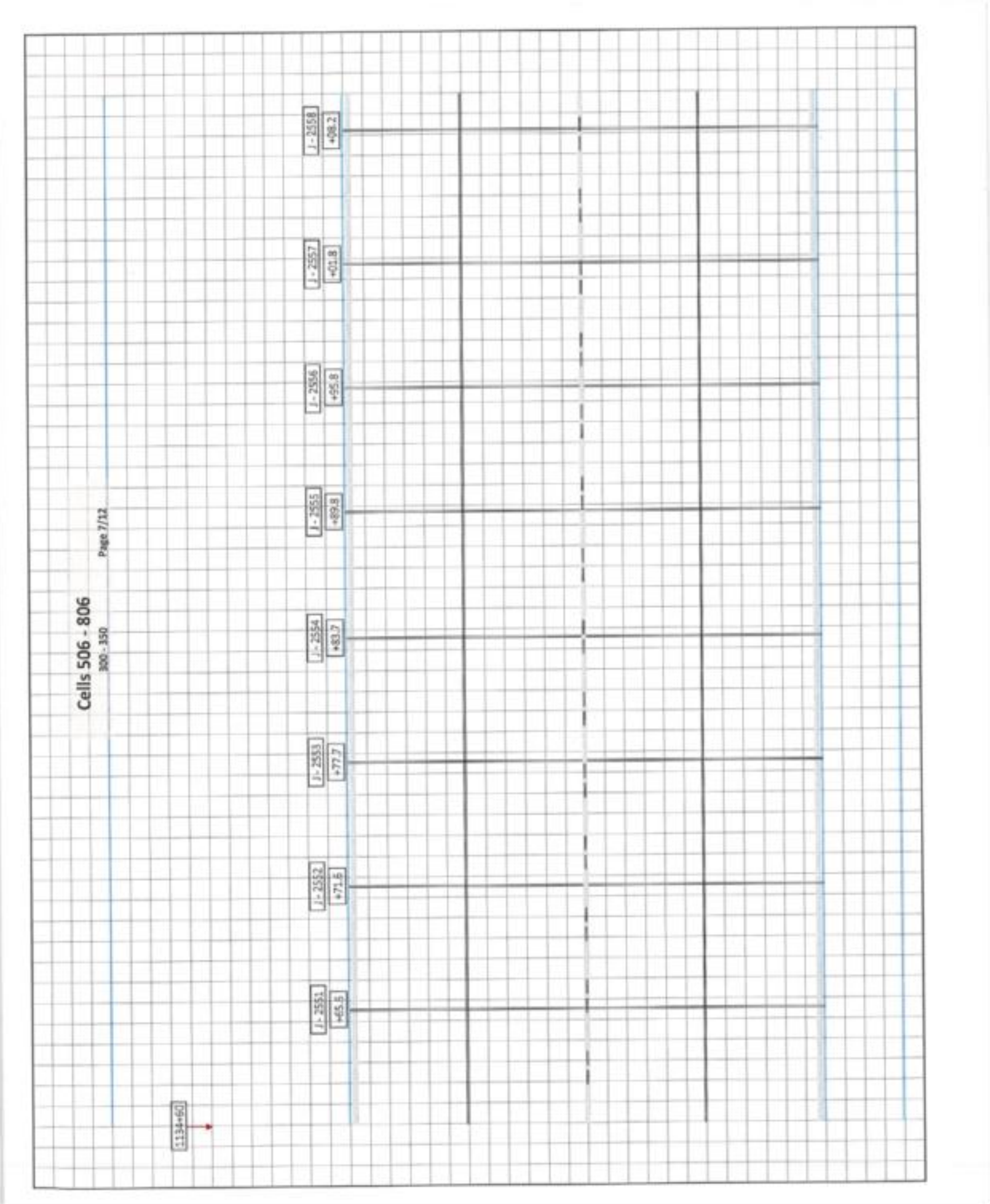

Figure A29: Distress map for Cells 506 through 806.. contd.

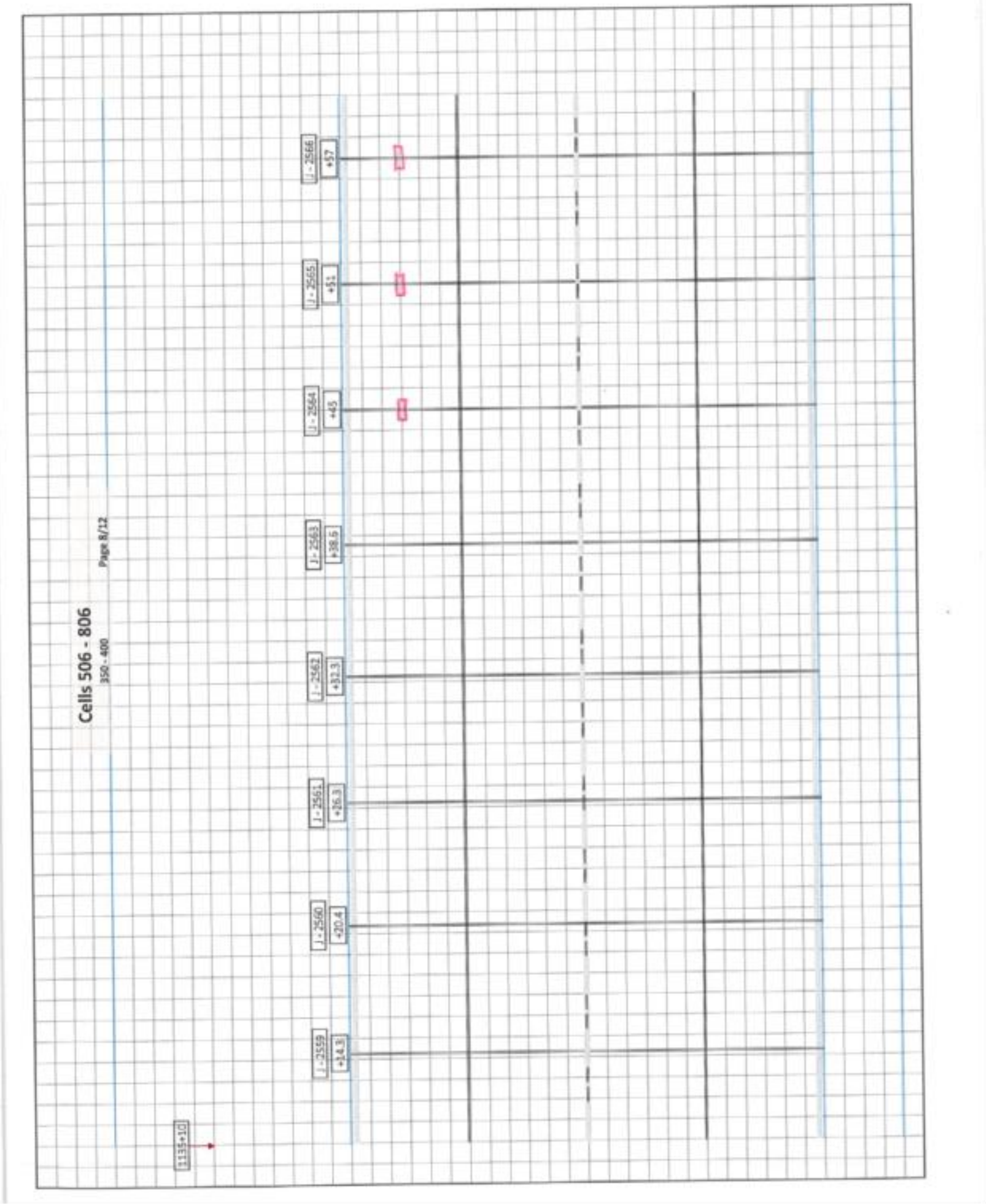

Figure A30: Distress map for Cells 506 through 806.. contd.

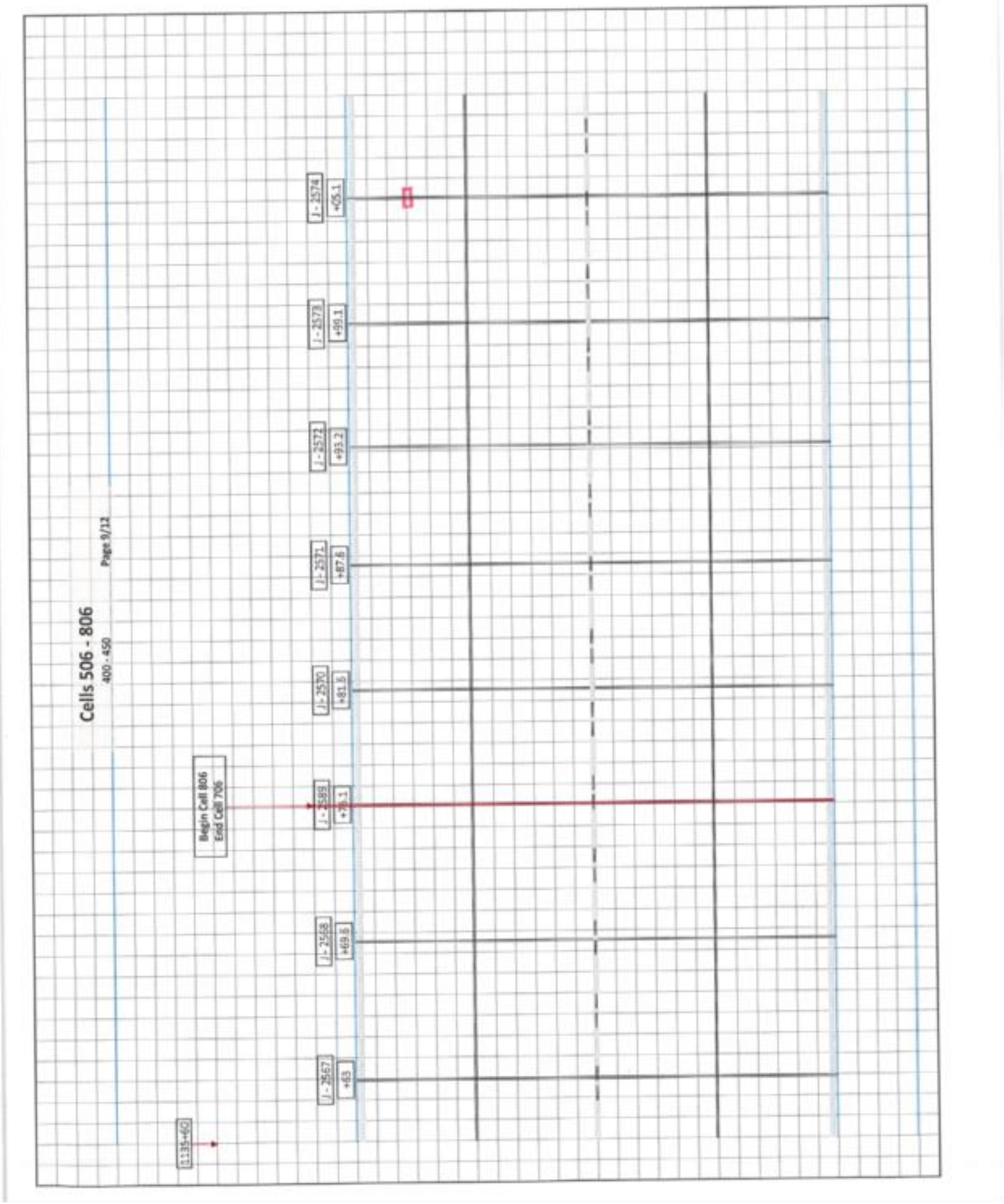

Figure A31: Distress map for Cells 506 through 806.. contd.

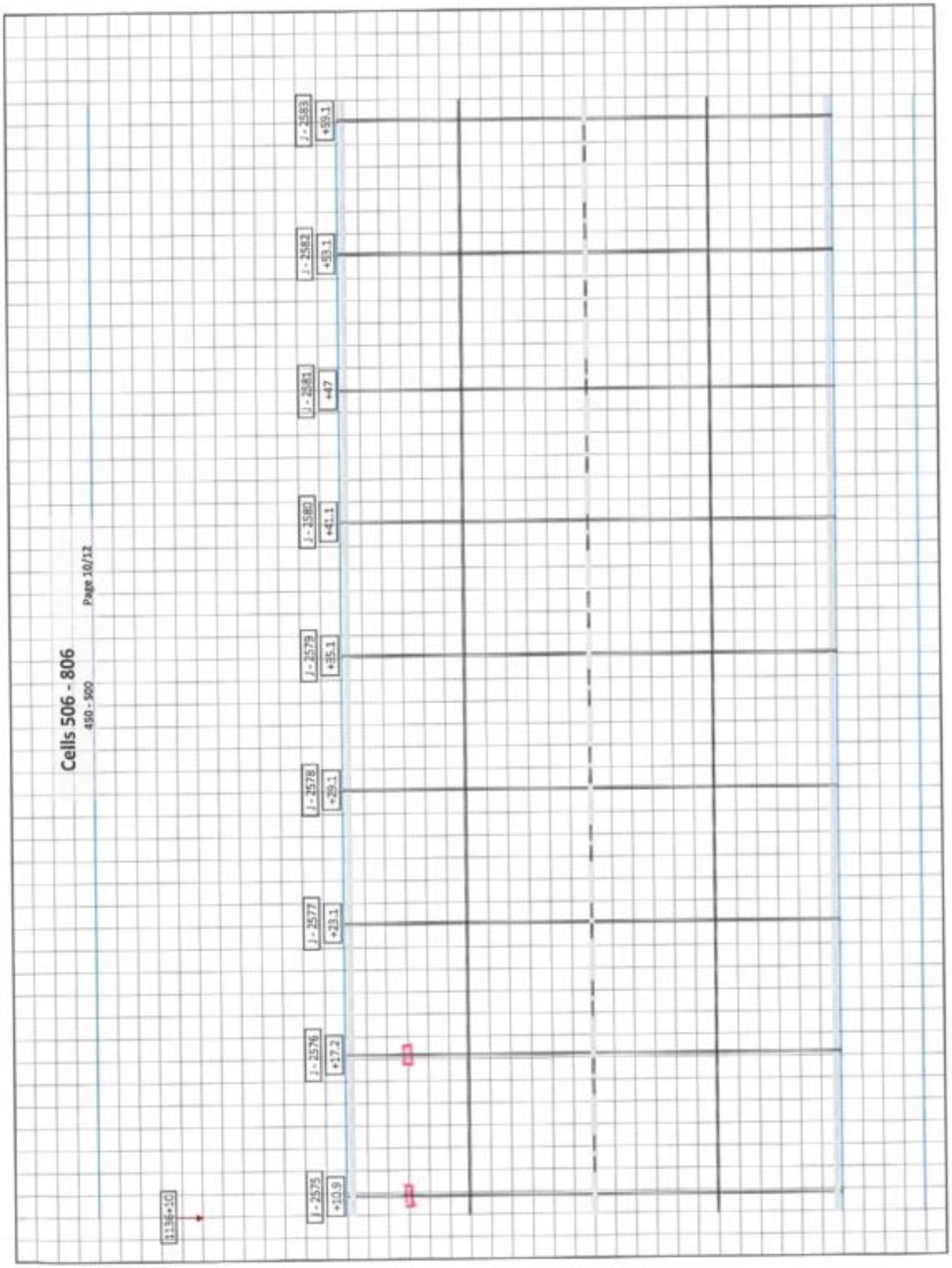

Figure A32: Distress map for Cells 506 through 806.. contd.

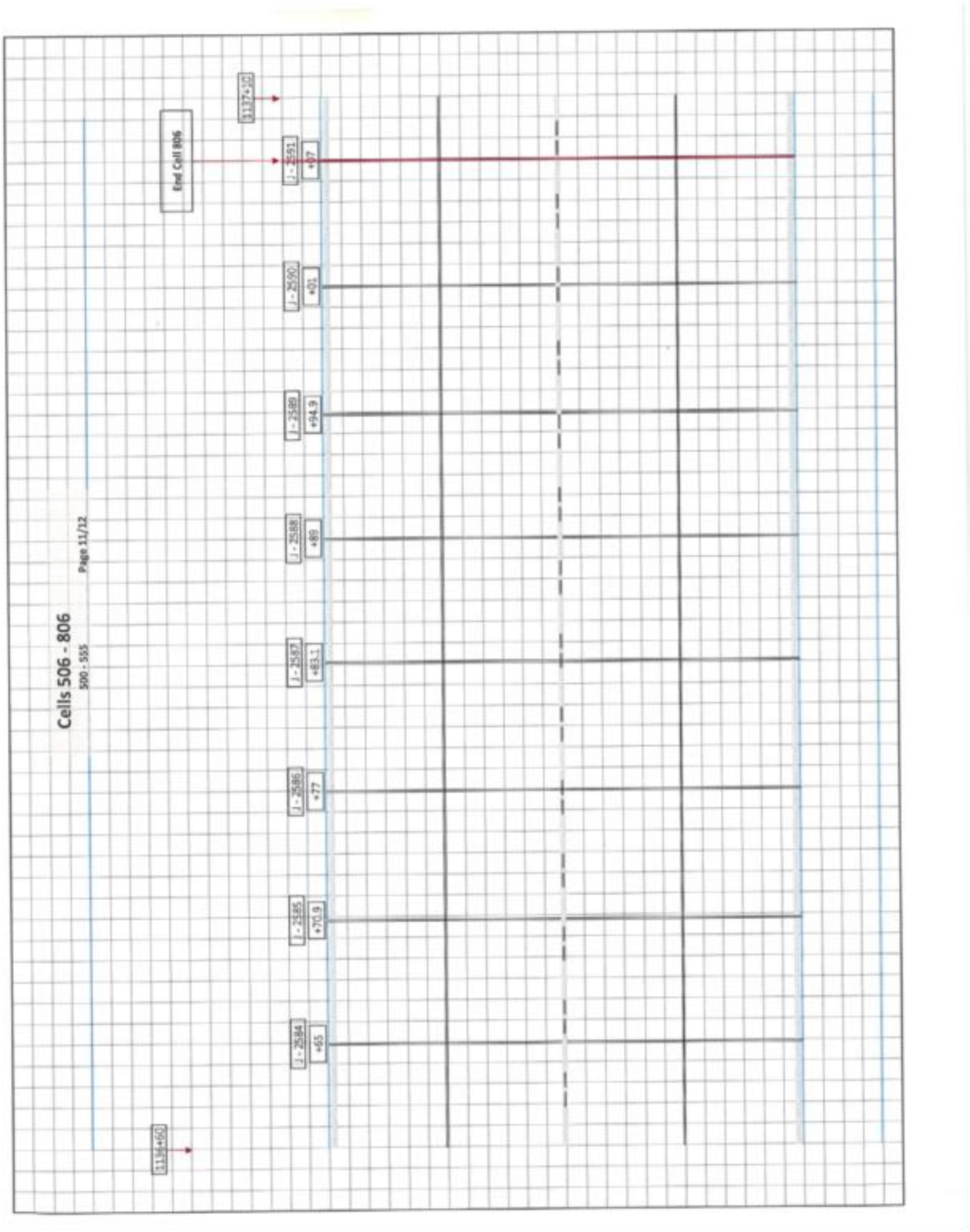

Figure A33: Distress map for Cells 506 through 806.. contd.

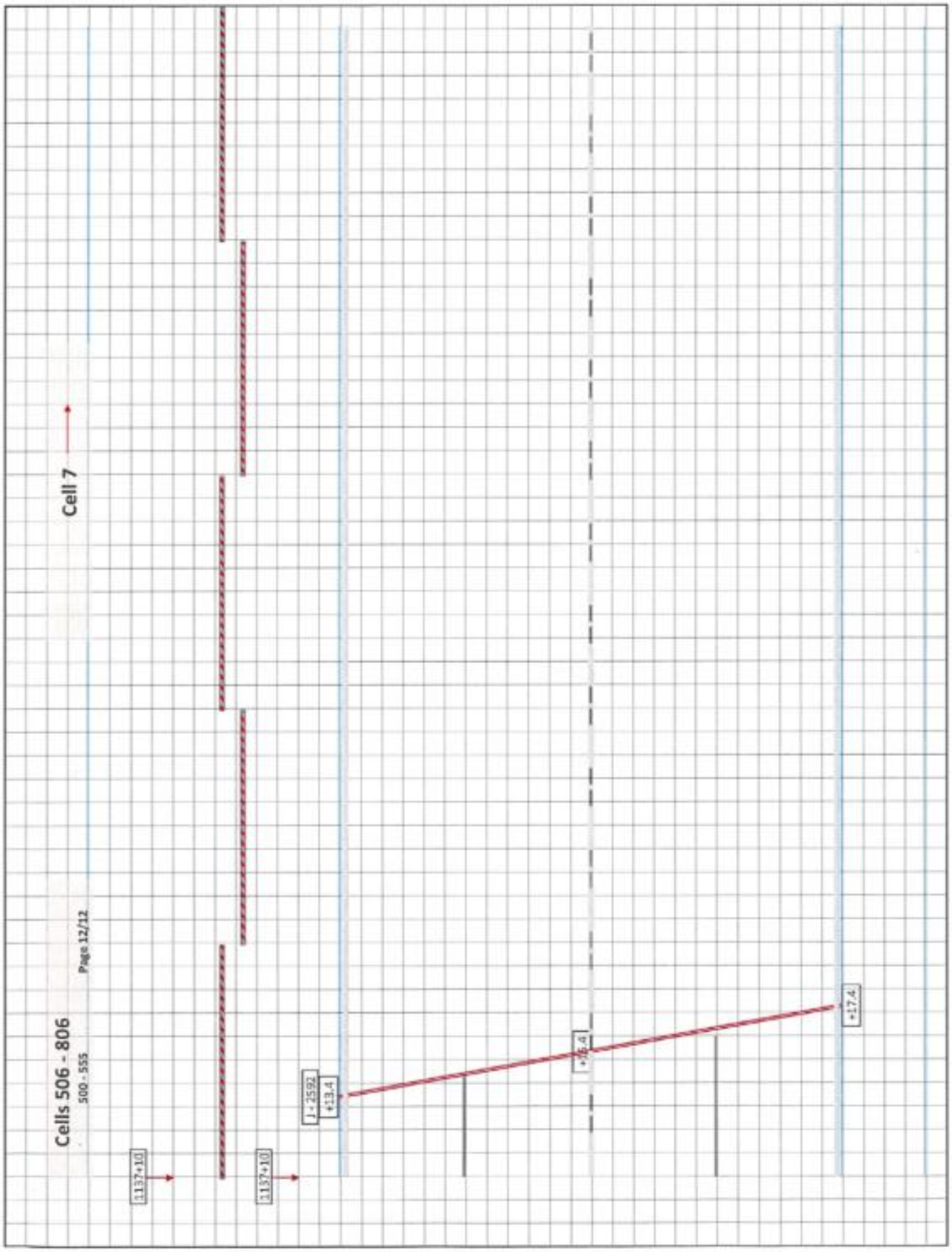

Figure A34: Distress map for Cells 506 through 806.. contd.

APPENDIX B

Joint Movement Data from Spring Loaded Potentiometer

Note: This Appendix presents the joint movement data recorded by the spring loaded potentiometers installed at different cells. Note that some of the data are appeared to be erroneous and not considered for any analysis.

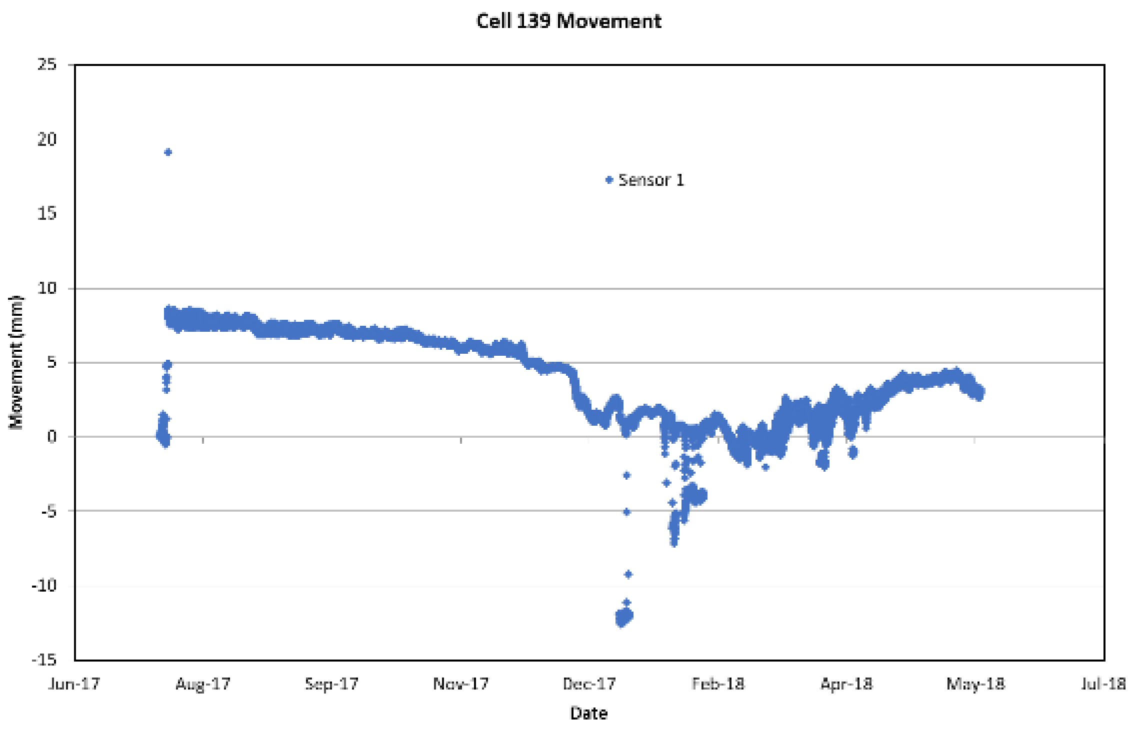

Figure B1. Joint movement data for Cell 139, Sensor 1.

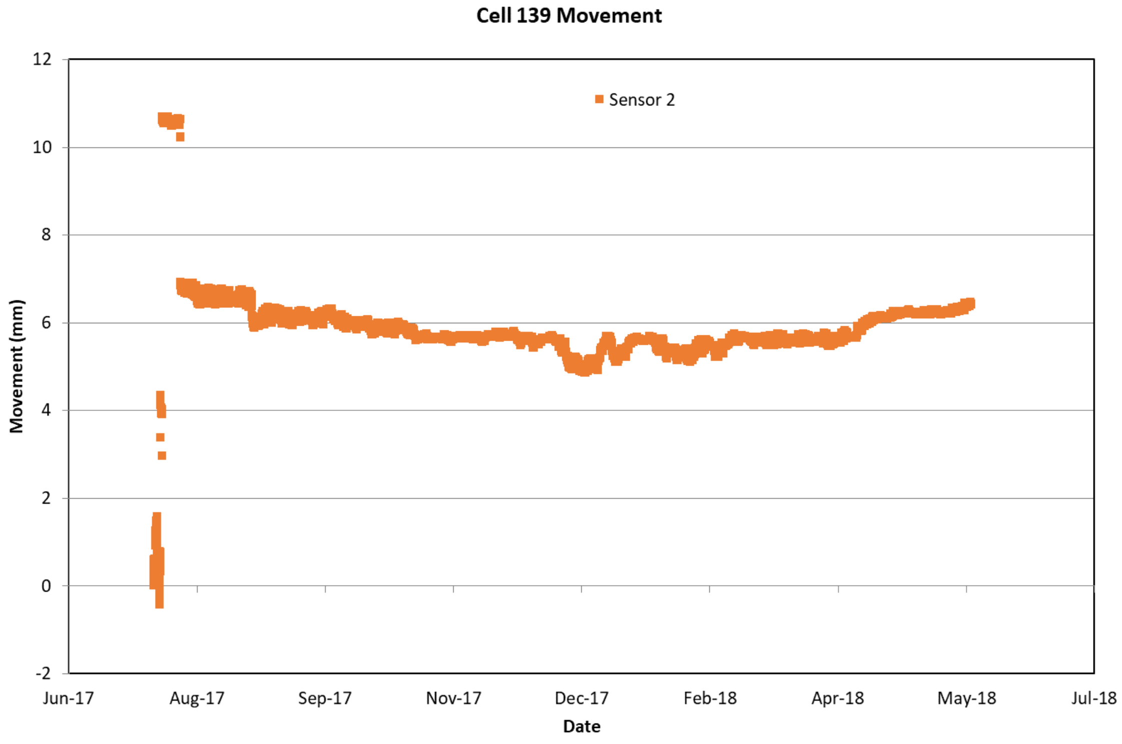

Figure B2. Joint movement data for Cell 139, Sensor 2.

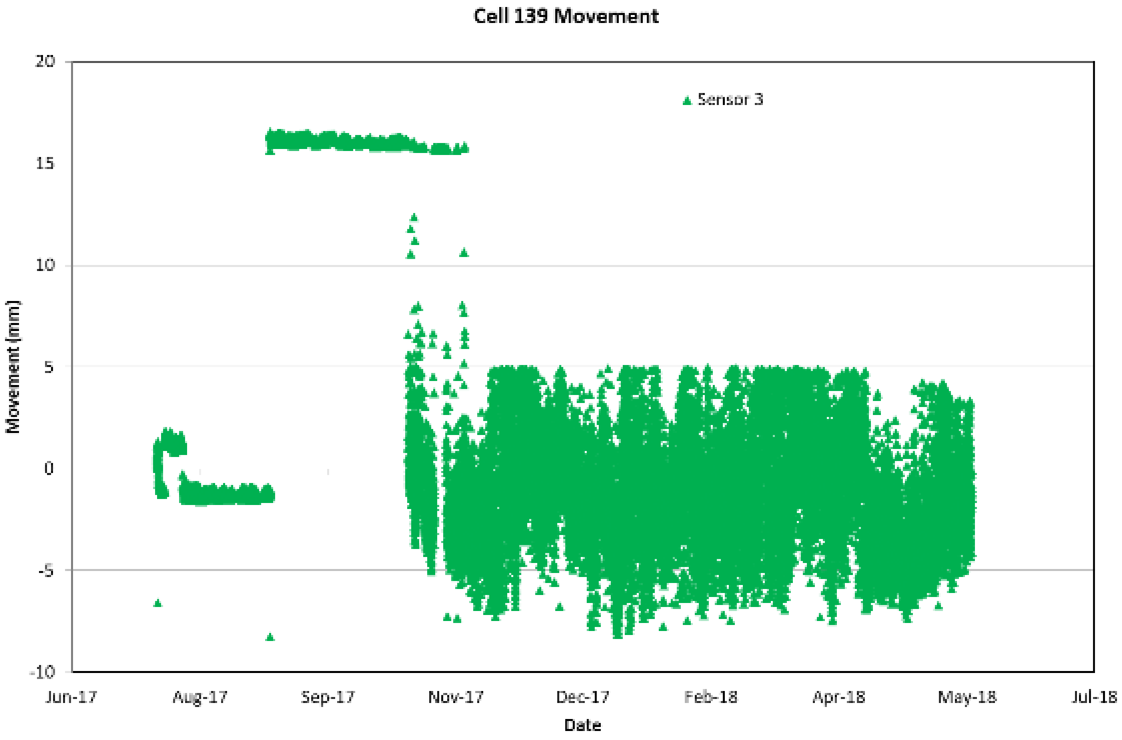

Figure B3. Joint movement data for Cell 139, Sensor 3 **(Bad sensor)**.

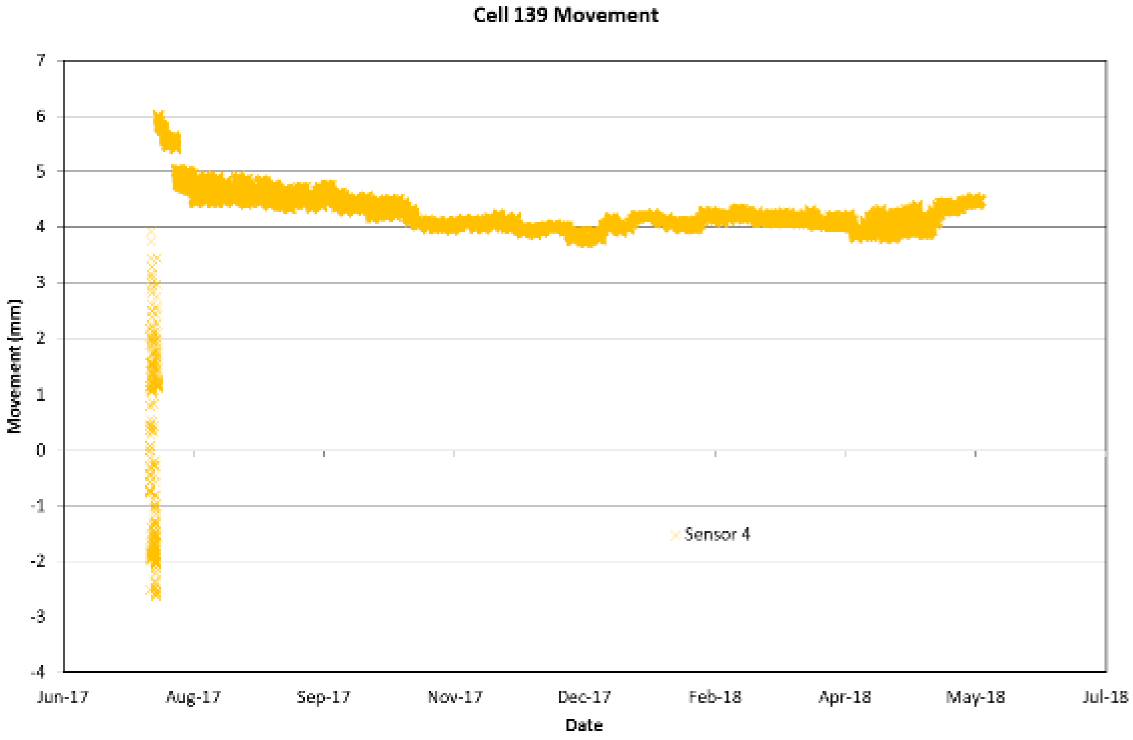

Figure B4. Joint movement data for Cell 139, Sensor 4.

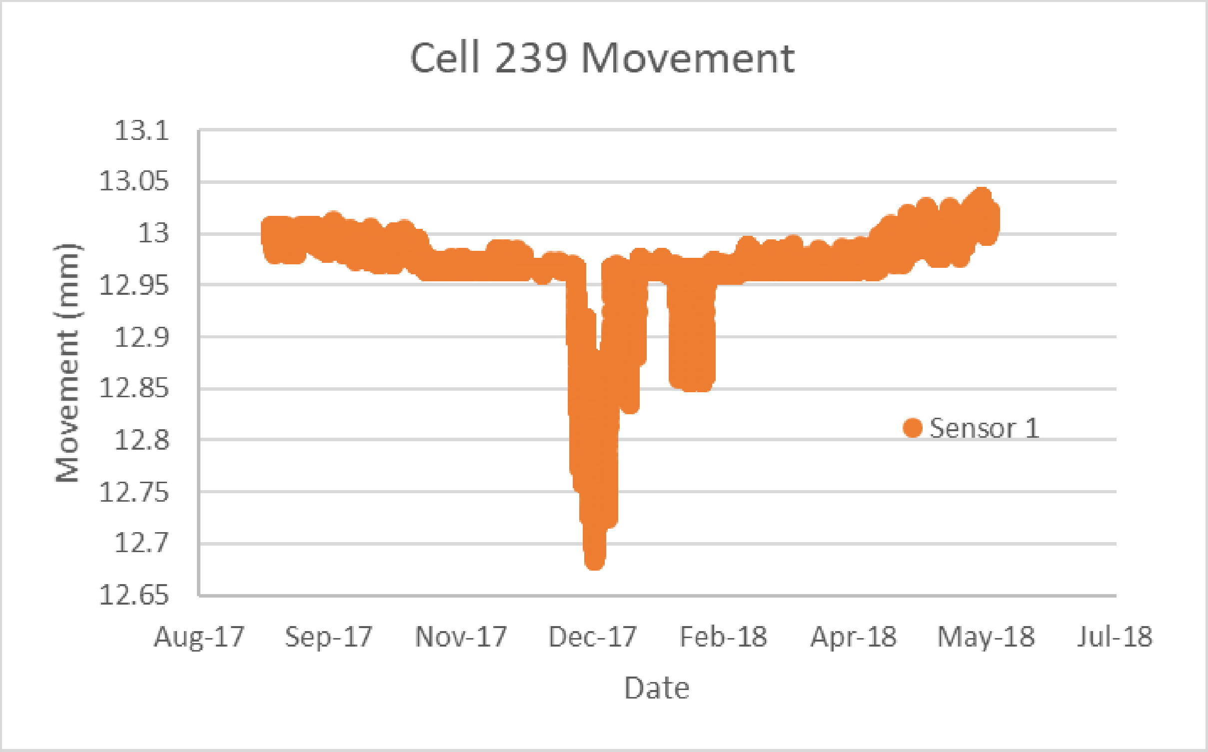

Figure B5. Joint movement data for Cell 239, Sensor 1.

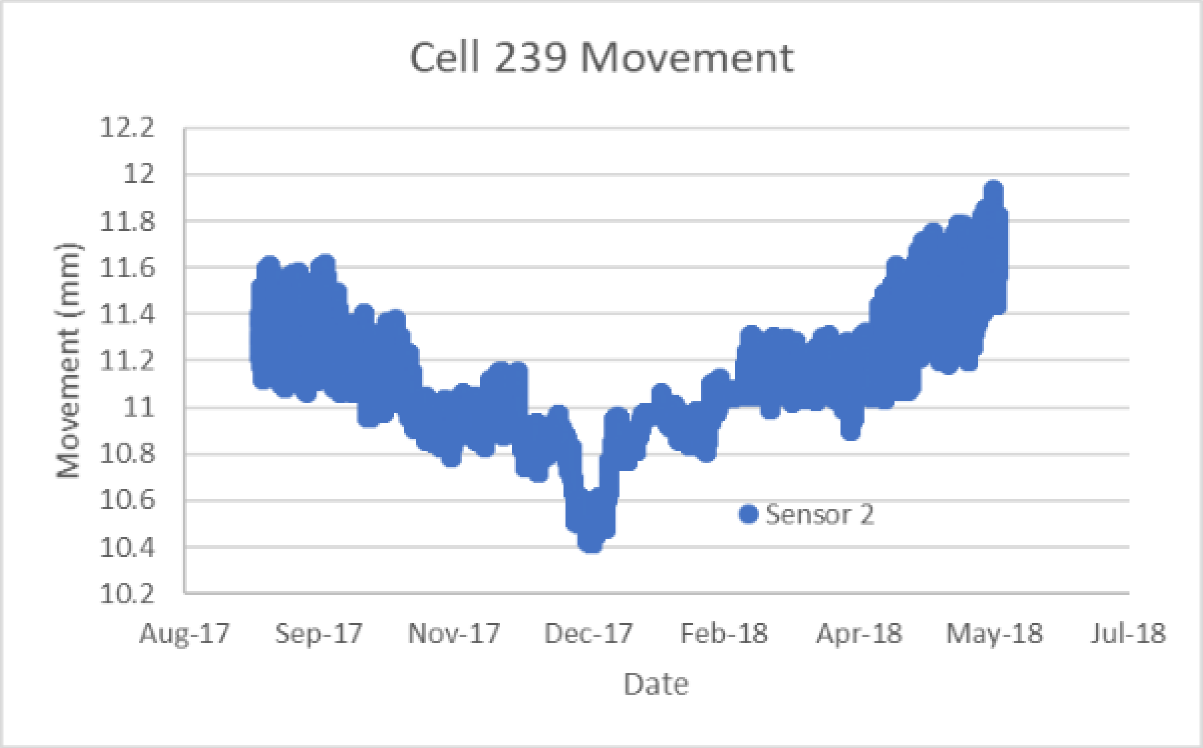

Figure B6. Joint movement data for Cell 239, Sensor 2.

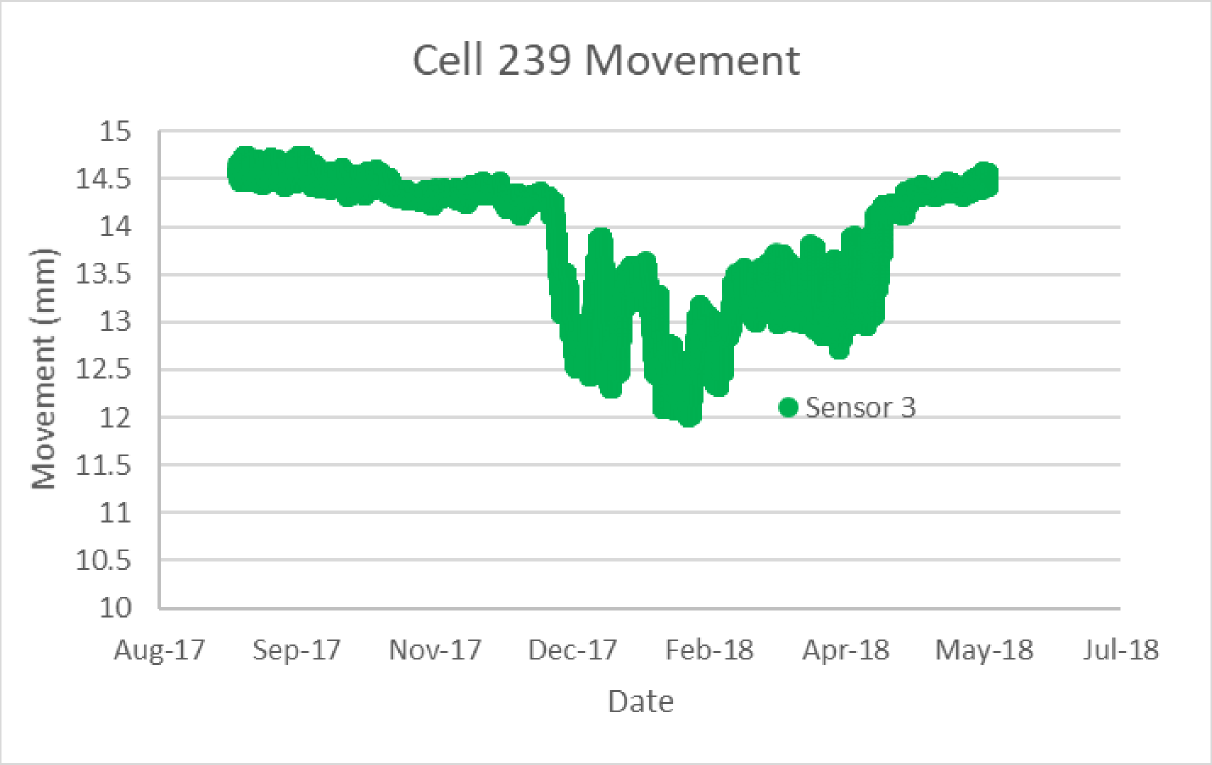

Figure B7. Joint movement data for Cell 239, Sensor 3.

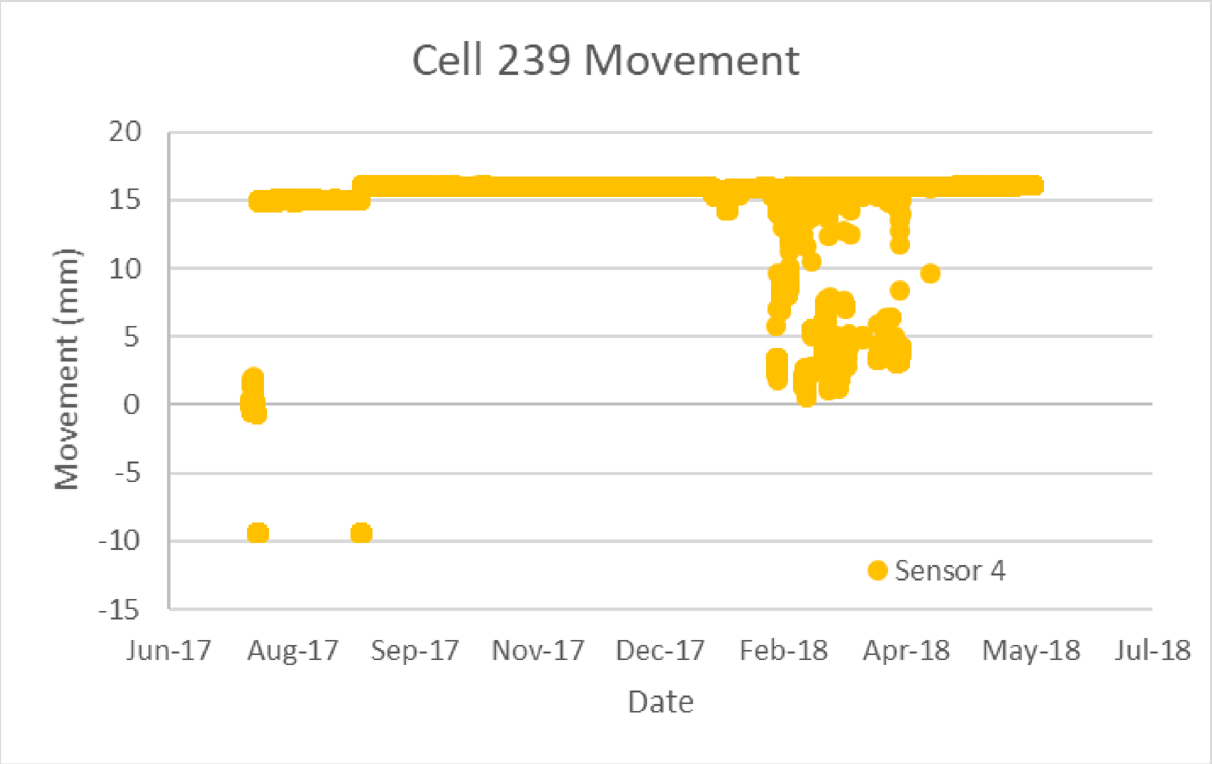

Figure B8. Joint movement data for Cell 239, Sensor 4.

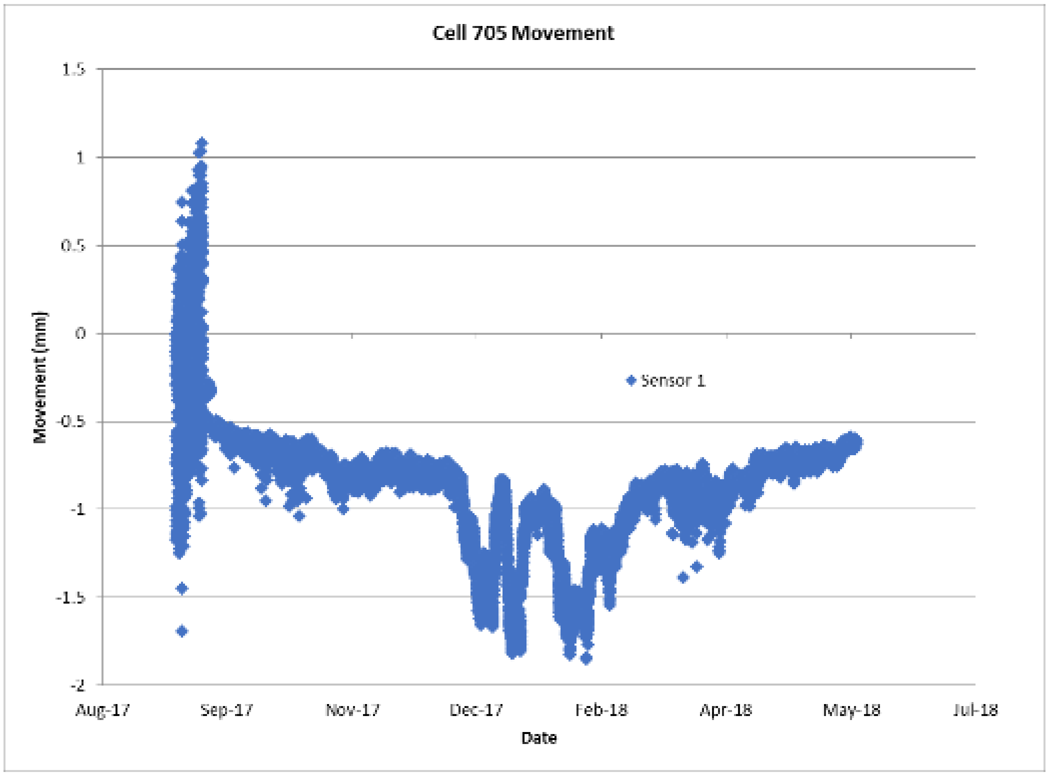

Figure B9. Joint movement data for Cell 705, Sensor 1.

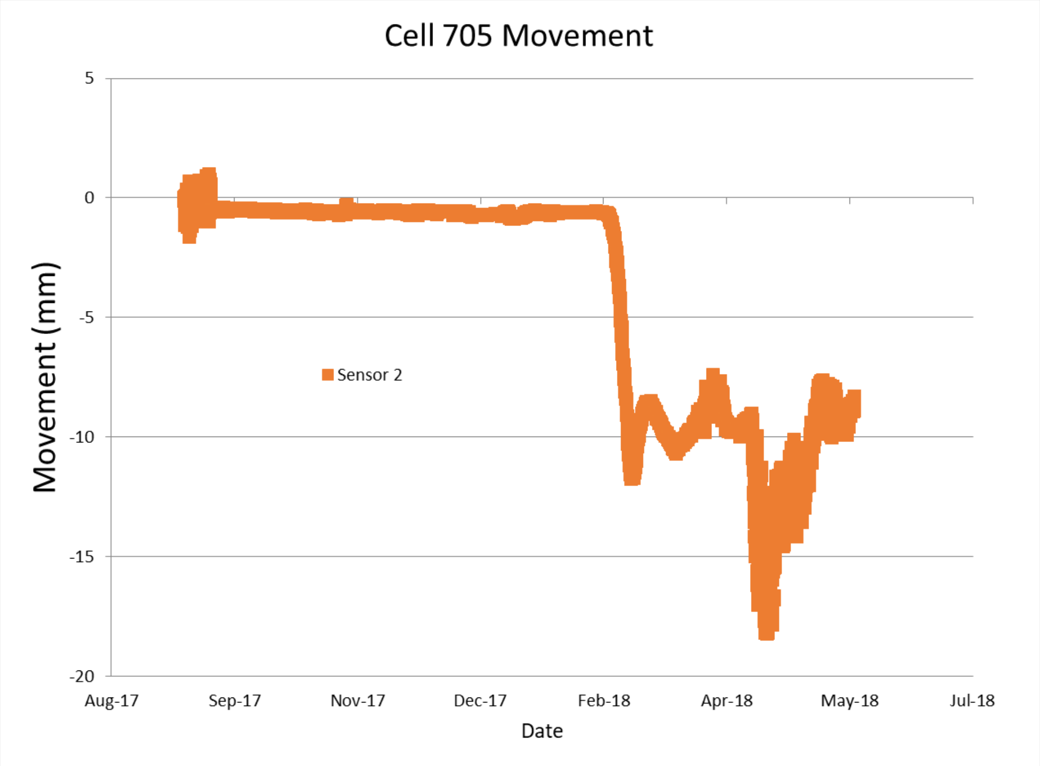

Figure B10. Joint movement data for Cell 705, Sensor 2.

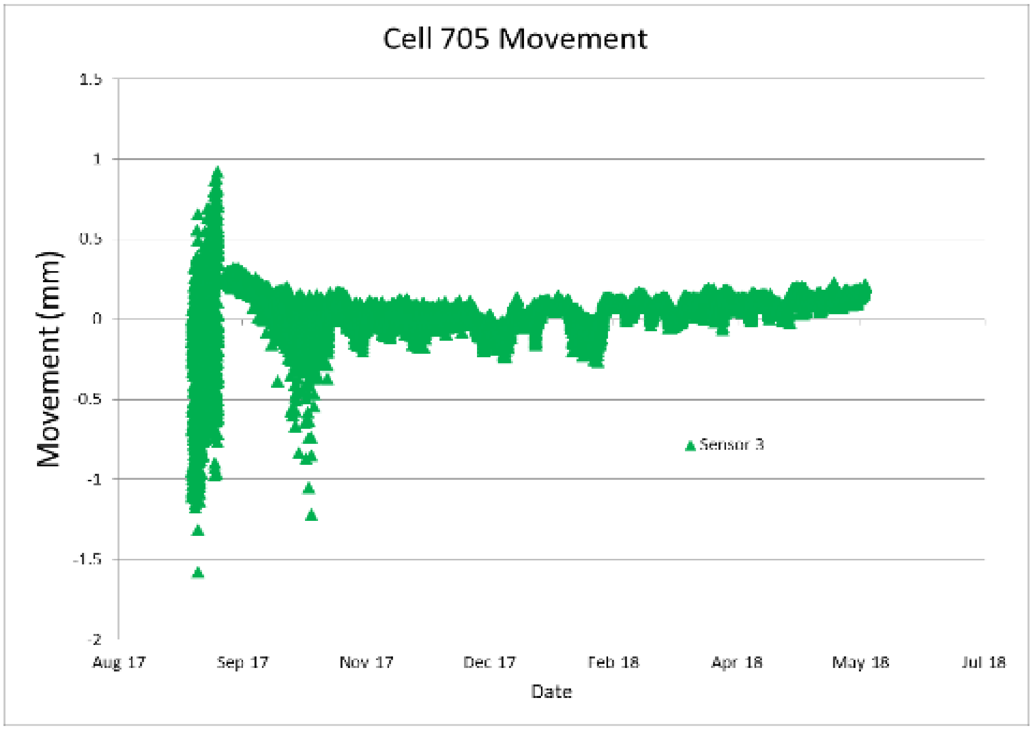

Figure B11. Joint movement data for Cell 705, Sensor 3.

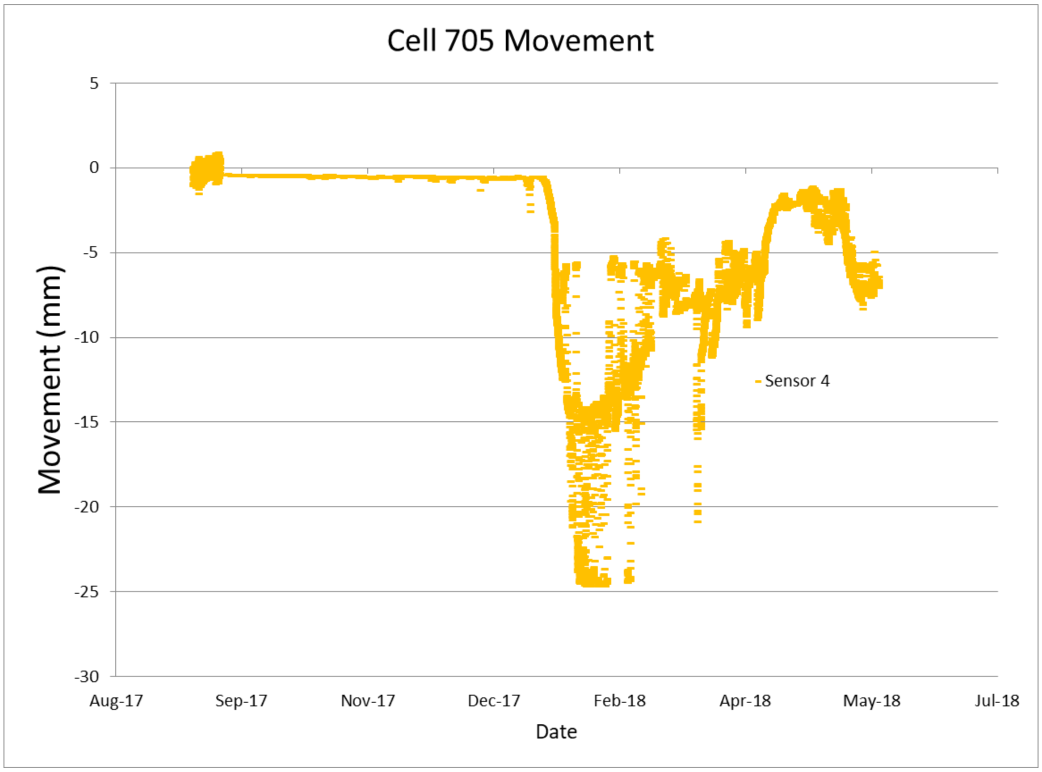

Figure B12. Joint movement data for Cell705, Sensor 4.

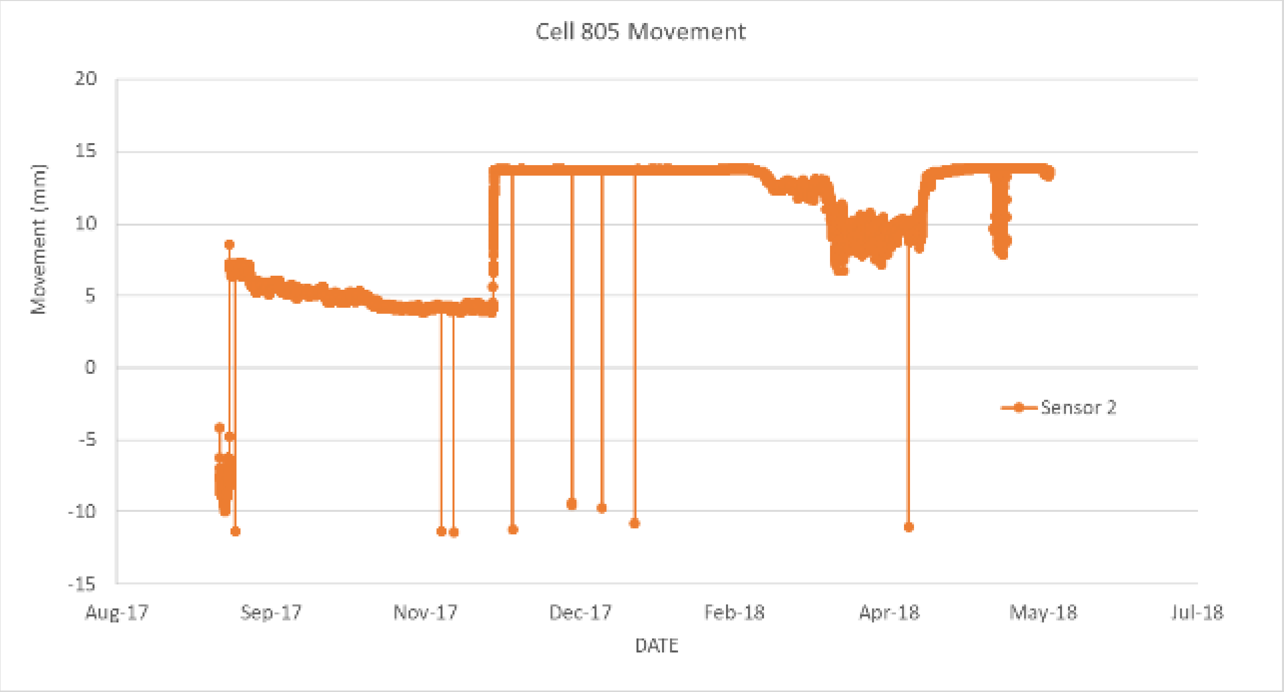

Figure B13. Joint movement data for Cell 805, Sensor 2.

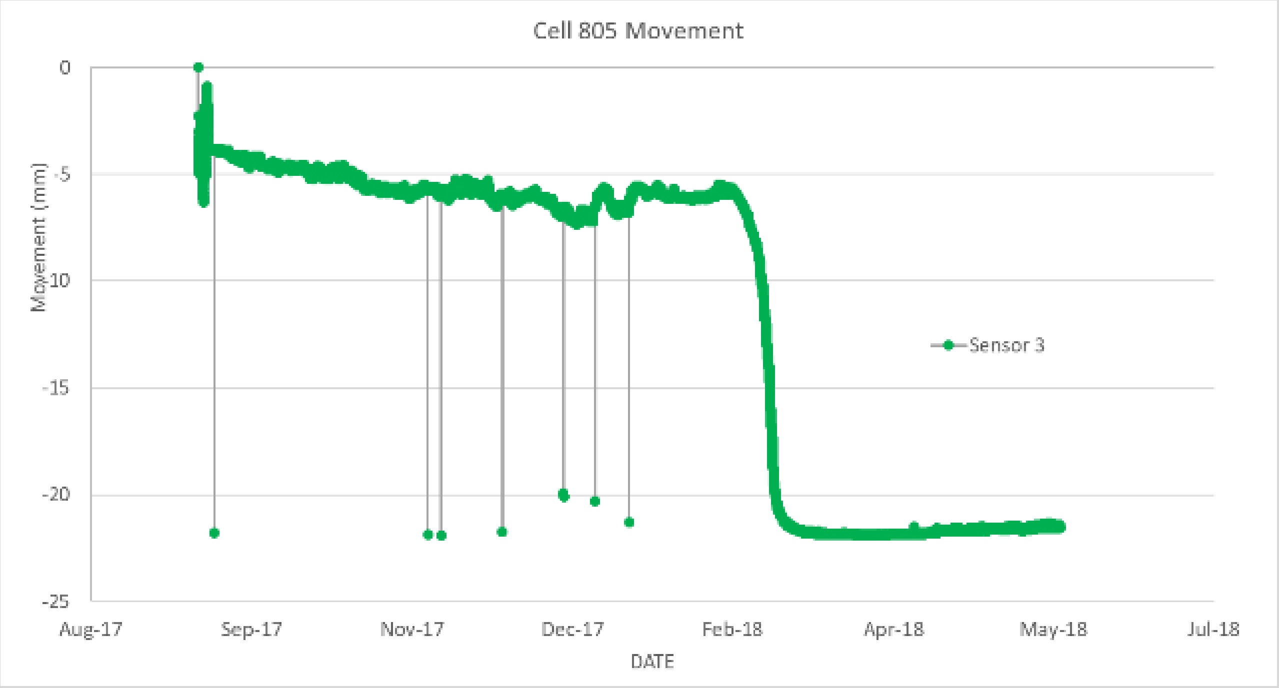

Figure B14. Joint movement data for Cell 805, Sensor 3 **(Bad sensor)**.

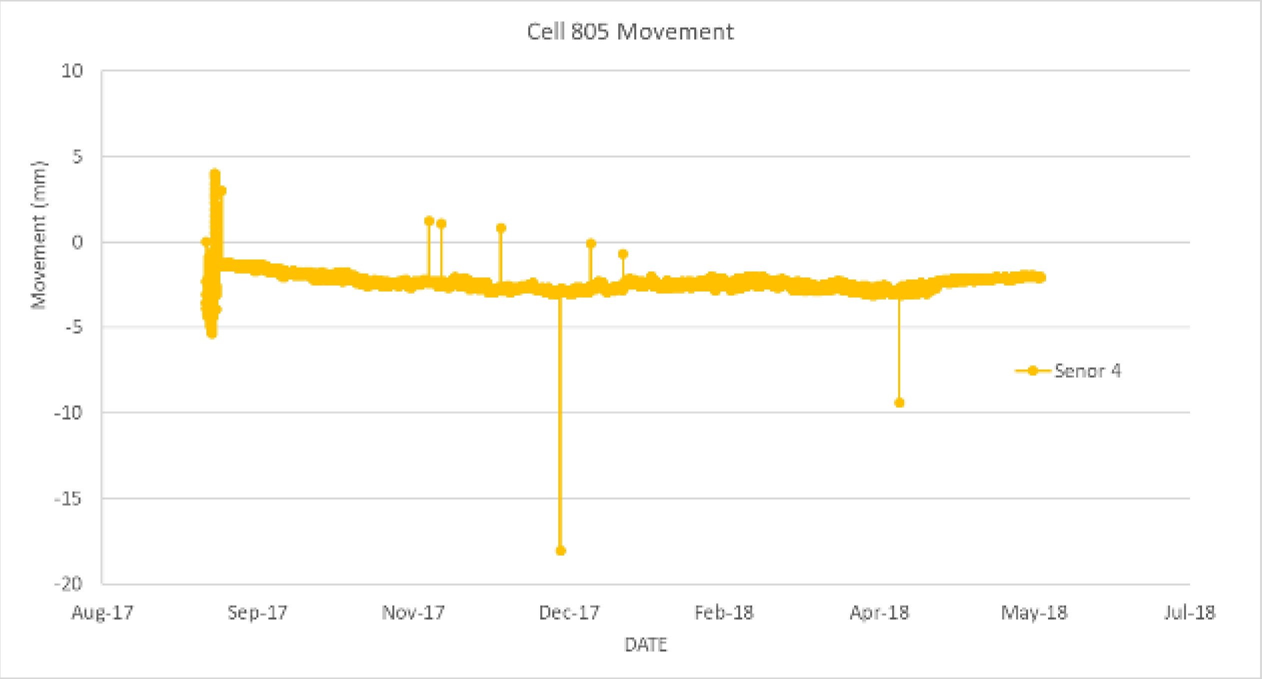

Figure B15. Joint movement data for Cell 805, Sensor 4.

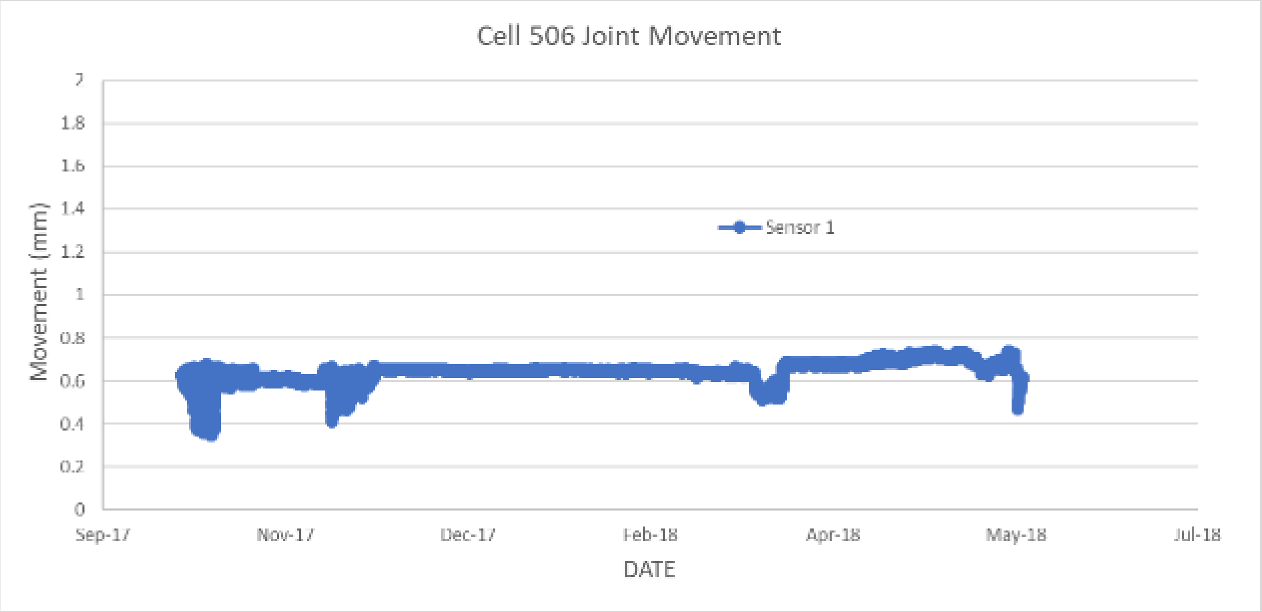

Figure B16. Joint movement data for Cell 506, Sensor 1.

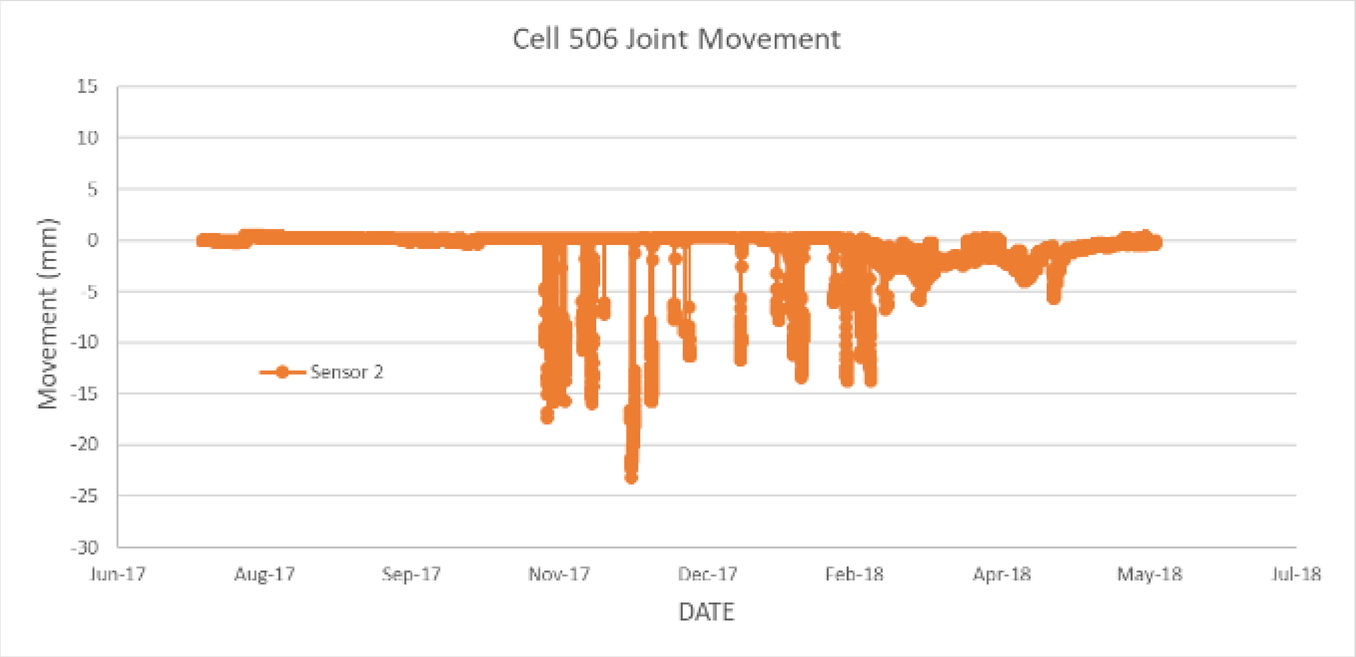

Figure B17. Joint movement data for Cell 506, Sensor 2.

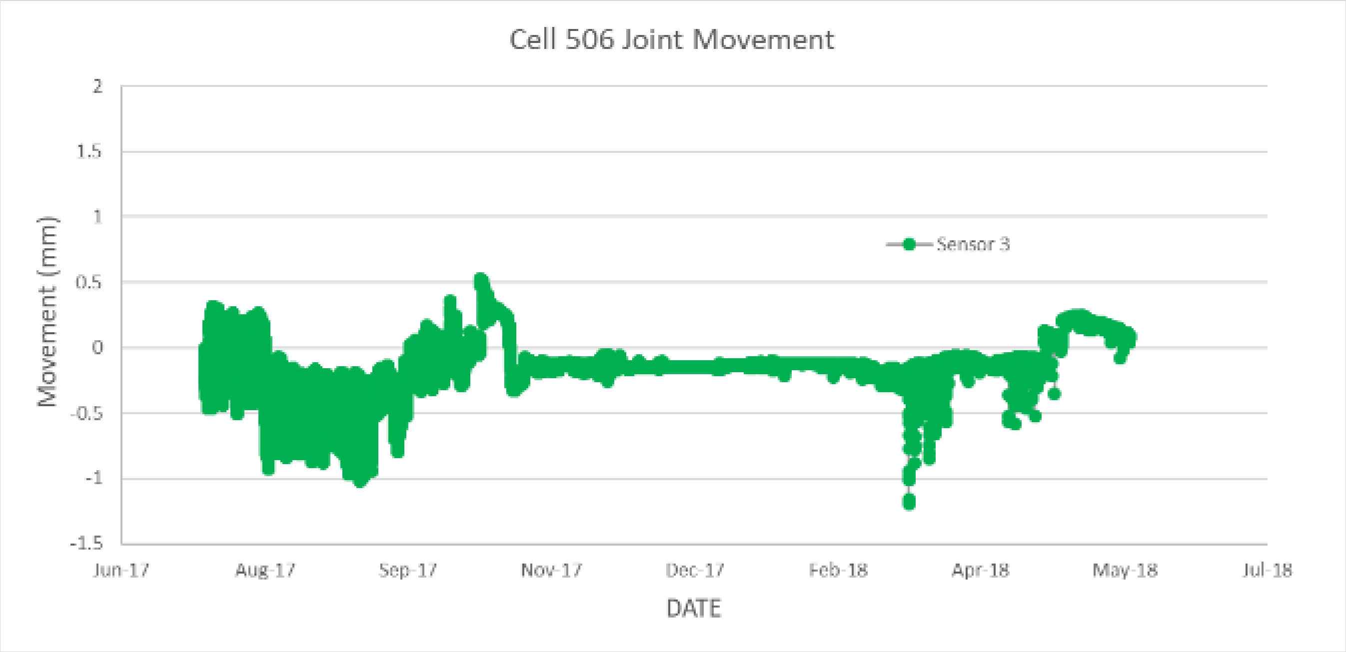

Figure B18. Joint movement data for Cell 506, Sensor 3.

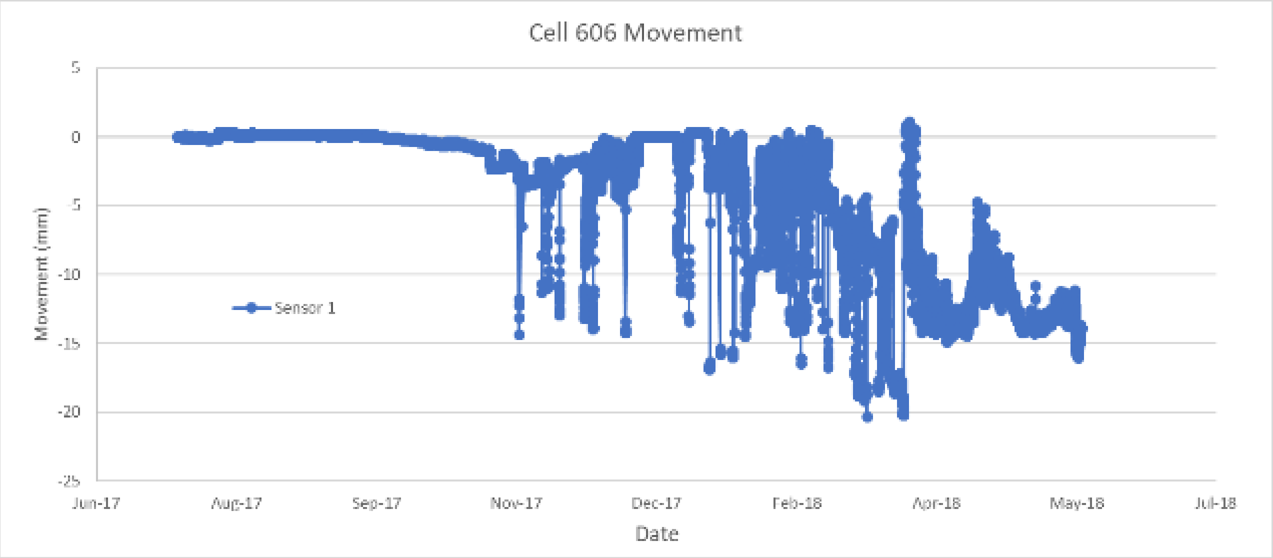

Figure B19. Joint movement data for Cell 606, Sensor 1.

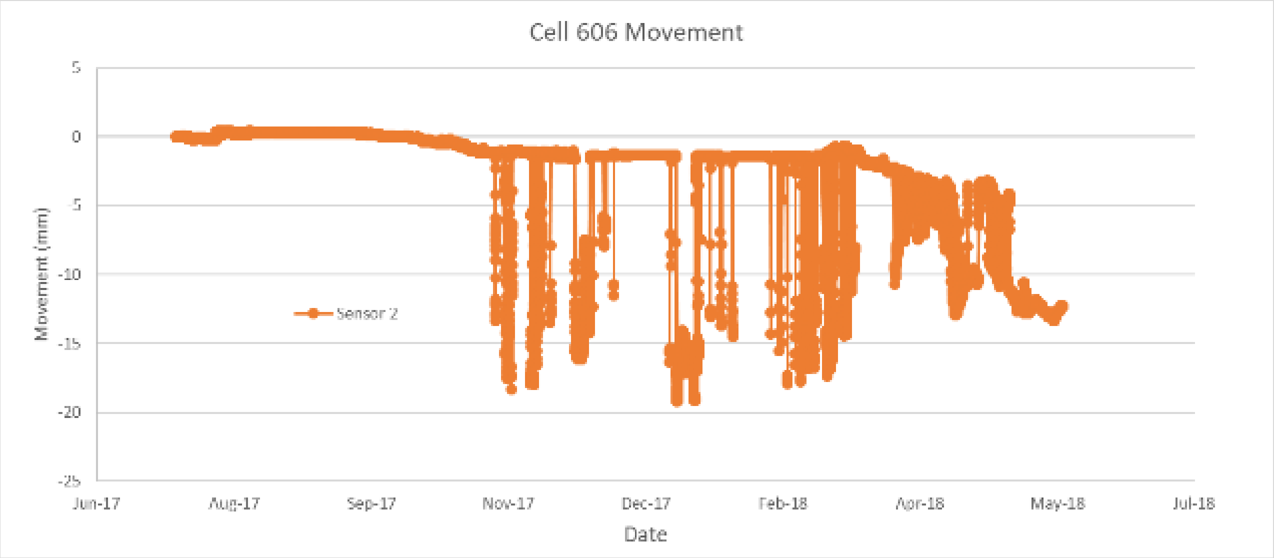

Figure B20. Joint movement data for Cell 606, Sensor 2.

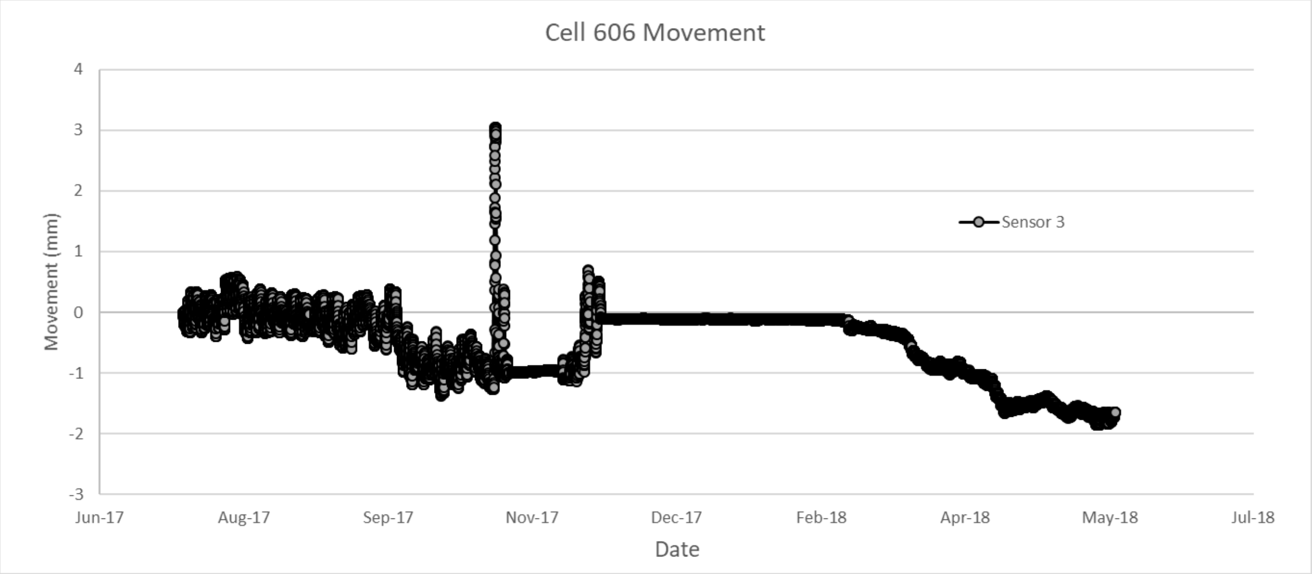

Figure B21. Joint movement data for Cell 606, Sensor 3.

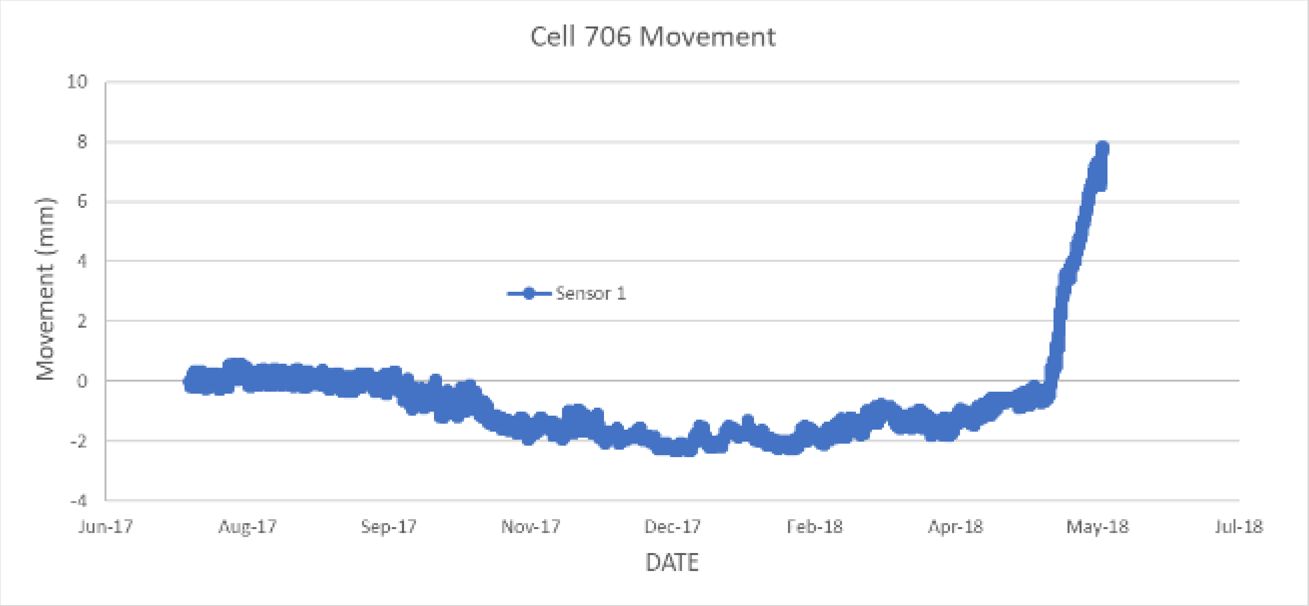

Figure B22. Joint movement data for Cell 706, Sensor 1.

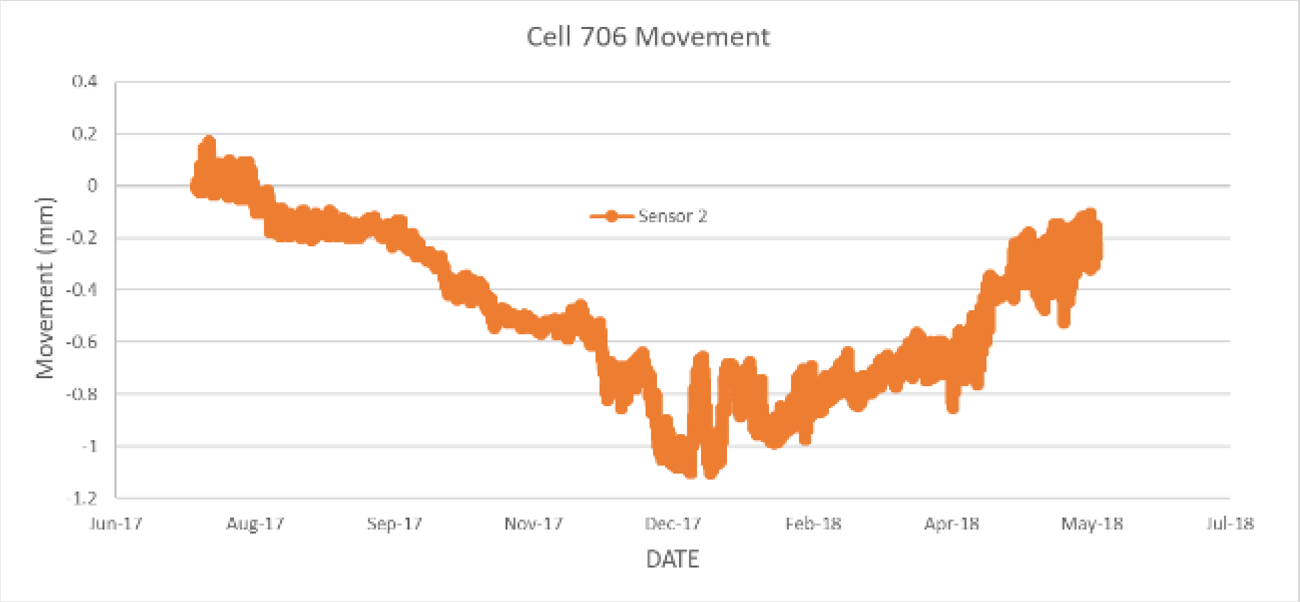

Figure B23. Joint movement data for Cell 706, Sensor 2.

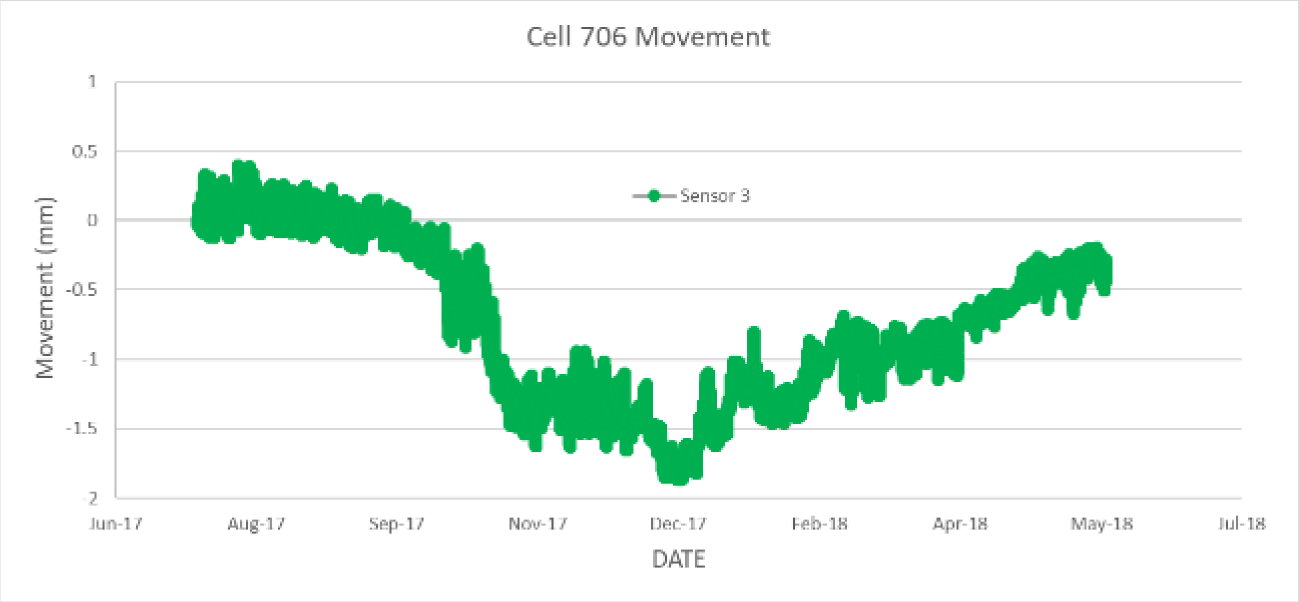

Figure B24. Joint movement data for Cell 706, Sensor 3.

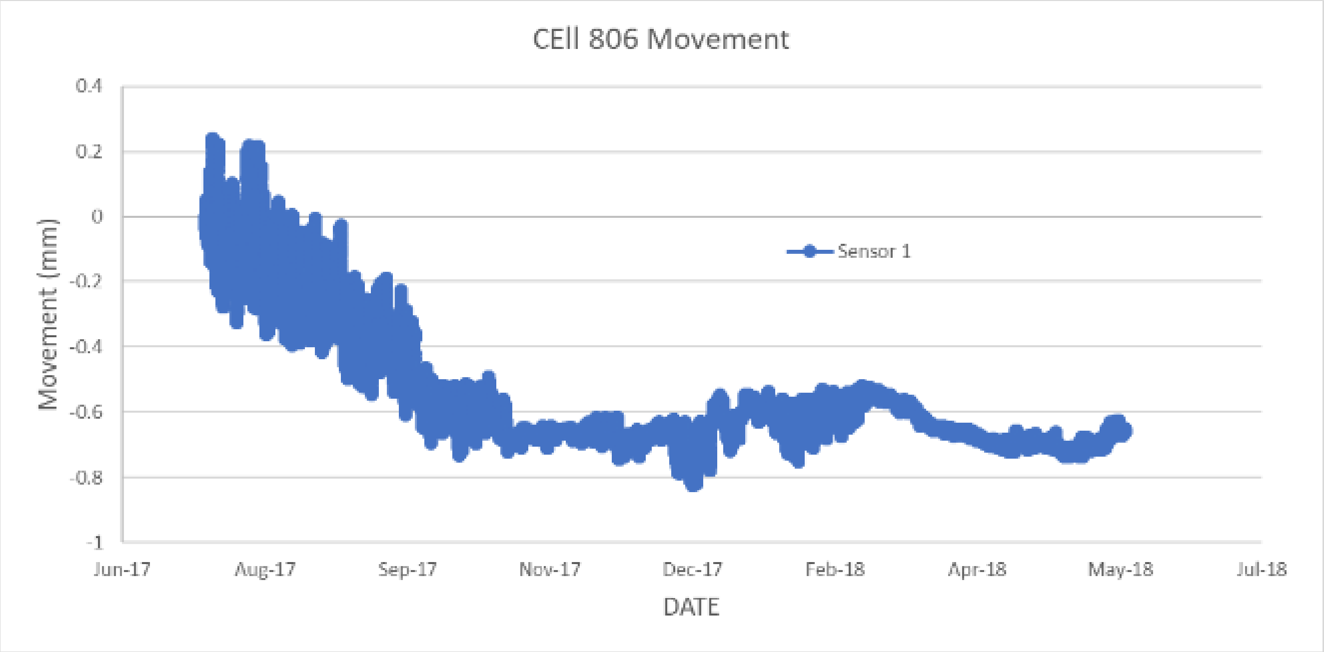

Figure B25. Joint movement data for Cell 806, Sensor 1.

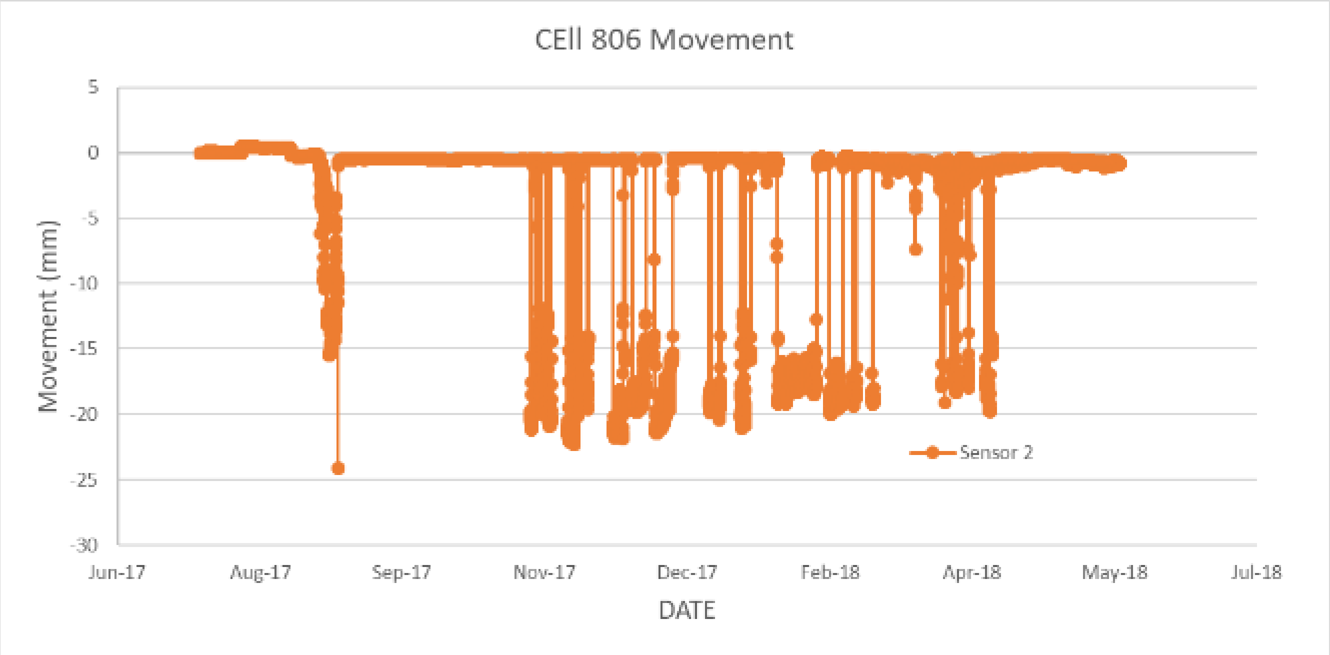

Figure B26. Joint movement data for Cell 806, Sensor 2 **(Bad sensor)**.

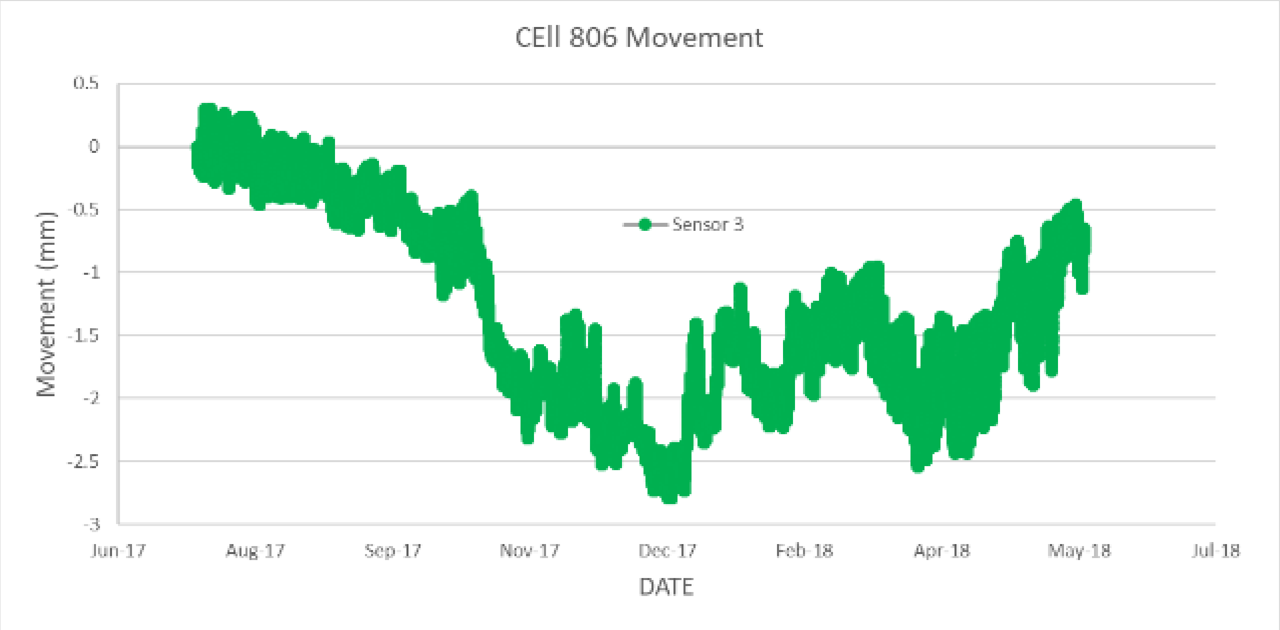

Figure B27. Joint movement data for Cell 806, Sensor 3.